UAB
Universitat Autònoma de Barcelona

X-ray studies of accreting black hole X-ray binaries

Santiago Ubach Ramírez

ADVERTIMENT. L'accés als continguts d'aquesta tesi queda condicionat a l'acceptació de les condicions d'ús establertes per la següent llicència Creative Commons:  https://creativecommons.org/licenses/?lang=ca

ADVERTENCIA. El acceso a los contenidos de esta tesis queda condicionado a la aceptación de las condiciones de uso establecidas por la siguiente licencia Creative Commons:  https://creativecommons.org/licenses/?lang=es

WARNING. The access to the contents of this doctoral thesis it is limited to the acceptance of the use conditions set by the following Creative Commons license:  https://creativecommons.org/licenses/?lang=en

Universitat Autònoma de Barcelona

Facultat de Física

X-ray studies of accreting black hole X-ray binaries

Santiago Ubach Ramírez

Supervisors:
Dr. Lluís Font Guiteras

Dr. Markus Gaug - Dr. James F. Steiner

PhD in *Physics*

February 23, 2025

Declaration

I, Santiago Ubach Ramírez, of the Unitat de Física de les Radiacions, Universitat Autònoma de Barcelona, confirm that this is my own work and figures, tables, equations, code snippets, artworks, and illustrations in this report are original and have not been taken from any other person's work, except where the works of others have been explicitly acknowledged, quoted, and referenced. I understand that if failing to do so will be considered a case of plagiarism. Plagiarism is a form of academic misconduct and will be penalised accordingly.

I give consent to a copy of my report being shared with future students as an exemplar.

Santiago Ubach Ramírez
February 23, 2025

Abstract

L'astrofísica busca entendre els mecanismes que governen els objectes celestes i les seves interaccions a través de l'univers. Els binaris de forats negres amb emissions de raigs X (BHXRBs) proporcionen un laboratori excepcional per estudiar la física d'acreció, els jets relativistes i els efectes de la gravetat extrema. Aquesta tesi se centra en l'evolució dels BHXRBs en la banda de raigs X, analitzant les seves propietats espectrals i temporals a través de diferents estats d'acreció, incloent-hi l'estat dur (HS), l'estat tou-intermedi/estat tou (SIMS/SS), i les mesures de rotació mitjançant el modelatge de l'emissió tèrmica del disc ("ajustament d'emissió del continu"). Una anàlisi auto-consistent ha revelat que la connexió entre el disc i la corona juga un paper crucial en la forma de l'emissió observada en raigs X. Utilitzant dades de múltiples observatoris de raigs X, aquest treball explora l'evolució del disc d'acreció i la geometria de la corona mitjançant tècniques avançades de modelatge espectral. Un descobriment clau és que en l'estat dur, contràriament a la creença comuna de que el disc d'acreció estaria altament truncat, el disc intern no està necessàriament truncat i podria ser no truncat o lleugerament truncat, amb una fracció de reflexió dels raigs X propera a la unitat com s'esperava. Això suggereix una interacció disc-corona més complexa del que s'havia assumit prèviament. La transició a l'estat tou-intermedi i a l'estat tou (SIMS/SS) es marca per l'emergència d'un disc d'acreció autoenfosquit, on una disminució sobtada de la temperatura aparent del disc intern va acompanyada d'un augment del radi del disc inferit. Aquest efecte, derivat del modelatge espectral, depèn fortament de la inclinació del sistema, suggerint que l'enfosquiment geomètric juga un paper significatiu en el sorgiment de les propietats observades del disc. Cal destacar que aquest fenomen sembla ser una característica recurrent en els grans esclats de BHXRBs altament inclinats, indicant un mecanisme físic comú en joc durant el SIMS. A més, aquesta tesi presenta una mesura de la rotació d'un BHXRB en l'estat dur-intermedi (HIMS) mitjançant el mètode d'ajustament de l'emissió del continu. Els resultats indiquen un forat negre amb baix gir, descartant efectivament un alt gir en incorporar noves restriccions dinàmiques. La discrepància observada entre les estimacions d'inclinació mitjançant l'ajustament de l'emissió del continu i les obtingudes a través del modelatge de reflexió relativista suggereix un possible desajustament entre el disc intern d'acreció i l'òrbita binària, la qual cosa podria tenir implicacions significatives per a l'evolució del moment angular del sistema. Aquests resultats proporcionen noves perspectives sobre la física d'acreció dels BHXRBs, desafiant les suposicions tradicionals sobre la truncació del disc, la geometria de la corona i les restriccions de gir. Els resultats tenen implicacions àmplies per entendre els processos d'acreció en entorns de gravetat extrema, amb aplicacions potencials a altres objectes compactes com els estels de neutrons i els nuclis actius de galàxies (AGN).

Astrophysics seeks to understand the mechanisms governing celestial objects and their interactions across the universe. Black hole X-ray binaries (BHXRBs) provide an exceptional laboratory for studying accretion physics, relativistic jets, and strong gravity effects. This thesis focuses on the evolution of BHXRBs in the X-ray band, analyzing their spectral and timing properties across different accretion states, including the hard state (HS), the soft-intermediate/soft state (SIMS/SS), and spin measurements via modeling the thermal emission of the disk ("continuum

fitting"). A self-consistent analysis revealed that the disk-corona connection plays a crucial role in shaping the observed X-ray emission. Using data from multiple X-ray observatories, this work explores the evolution of the accretion disk and the corona geometry through advanced spectral modeling techniques. A key finding is that in the HS, contrary to the commonly held belief that the accretion disk is highly truncated, the inner disk is not necessarily truncated and could be non-truncated or slightly truncated, and the reflection fraction is close to unity as expected. This suggests a more complex corona-disk interaction than previously assumed. The transition to the soft-intermediate and soft states (SIMS/SS) is marked by the emergence of a self-obscured accretion disk, where a sudden decrease in the apparent inner disk temperature is accompanied by an increase in the inferred disk radius. This effect, derived from spectral modeling, is strongly dependent on the system's inclination, suggesting that geometric obscuration plays a significant role in shaping the observed disk properties. Notably, this phenomenon appears to be a recurrent feature in major outbursts of highly inclined BHXRBs, indicating a common physical mechanism at play during the SIMS. Furthermore, this thesis presents a spin measurement of a BHXRB in the hard-intermediate state (HIMS) using the continuum-fitting method. The results indicate a low-spin black hole, effectively ruling out high spin when incorporating new dynamical constraints. The observed discrepancy between inclination estimates from continuum fitting and those obtained via relativistic reflection modeling suggests a potential misalignment between the inner accretion disk and the binary orbit, which may have significant implications for the angular momentum evolution of the system. These findings provide new insights into the accretion physics of BHXRBs, challenging traditional assumptions about disk truncation, corona geometry, and spin constraints. The results have broad implications for understanding accretion processes in strong gravity environments, with potential applications to other compact objects such as neutron stars and active galactic nuclei (AGN).

Acknowledgements

I would like to thank Center for Astrophysics | Harvard & Smithsonian and Universitat Autònoma de Barcelona for providing the necessary resources and support for this PhD in physics. I gratefully acknowledge the financial support from NASA for the *NICER* general observer grant 80NSSC21K1886, Chandra General Observer grants GO8-19038A and GO9-20041X and the Chandra X-ray Observatory predoc fellowship. I want to thank my three supervisors during this PhD, Dr. Lluís Font Guiteras, Dr. Markus Gaug and Dr. James F. Steiner for their support and help to learn how to become a good researcher in the field of black hole X-ray binaries in different wavelengths and for their support to prepare proposals for the MAGIC collaboration and optical telescopes such as the Magellan telescopes. Without them, this thesis couldn't happen.

I also extend my gratitude to co-authors for their valuable insights and discussions that greatly enhanced the quality of my work.

Finally, I want to thank my wife, Valeria, for her support and help over my PhD and my family for their support to pursue my dream to study the universe.

Contents

List of Figures

List of Tables

List of Abbreviations

BH	Black Hole
HS	Hard State
HIMS	Hard-Intermediate State
SIMS	Soft-Intermediate State
SS	Soft State
NICER	Neutron star interior composition explorer
NuSTAR	Nuclear Spectroscopic Telescope Array
MAGIC	Major Atmospheric Gamma Imaging Cherenkov Telescopes
HESS	High Energy Stereoscopic System
VERITAS	Very Energetic Radiation Imaging Telescope Array System
BHXRB	Black Hole X-ray Binary
XRB	X-ray Binary

Chapter 1

Introduction

1.1 This Thesis

This thesis is presented in accordance with the guidelines of the Universitat Autònoma de Barcelona. Each chapter corresponds to a research paper that has been published, submitted, or is currently under review in a peer-reviewed astrophysical journal. This structure ensures a focused presentation, where only completed and peer-evaluated results are included. An introductory chapter provides the overarching argument and necessary scientific context.

The content of this thesis is based on three interrelated papers on the physics of black hole X-ray binaries, written in collaboration with my supervisors and colleagues. It has been formally declared that none of the co-authors are using the same material to obtain another academic degree.

The three chapters forming the core of this thesis are based on the following papers:

- Self-consistent Disk-reflection Analysis of the Black Hole Candidate X-Ray Binary MAXI J1813-095 with NICER, Swift, Chandra, and NuSTAR. Ubach et al. (2024a)

  Santiago Ubach, James F. Steiner, Jiachen Jiang, Javier García, Riley M. T. Connors, Guglielmo Mastroserio, Ye Feng, and John A. Tomsick

  The Astrophysical Journal, Volume 976, Number 1 (2024)

- Detection of Self-Obscuration and Evolving Winds from MAXI J1803-298 during its 2021 Outburst

  Santiago Ubach, James F. Steiner, Oluwashina K. Adegoke, Joseph Nielsen, Jeroen Homan, Dominic Chang, Kinjal Roy , Yuexin Zhang, Ole König, Yujia Song, Josephine Wong, and Razieh Emami

  Submitted to Astrophysical Journal

- Spin measurement through continuum fitting of GRS 1716-249 with new dynamical data

  Santiago Ubach, James F. Steiner, and Manuel A. P. Torres

  To be submitted

Correspondingly, all three studies are presented in Chapters 2,3 and 4 of this thesis. They are also available on the preprint server *ArXiv* (astro-ph).

Moreover each chapter presents an introduction and conclusions on their own. The second chapter refers to the case of a black hole X-ray binary system (BHXRBs) MAXI J1813-095 in its hard state (HS) where non-thermal emission coming from the corona is strong and accompanied by weak thermal emission from the inner disk. In this first Chapter, my colleagues and I presented the results of the analysis of seven observations with subsets of the X-ray telescopes *NICER*,

Swift, *NuSTAR* and *Chandra*. The key of this analysis is the multi-instrumental observation and self-consistent reflection analysis throughout the "stalled" outburst in 2018. The self-consistent reflection analysis showed that accurately fitting the Fe Kα line at $\sim$ 6.5 keV requires two reflection components: one to model the reflection fraction and another to account for the continuum. By matching these components, we ensure that the reflection is neither overestimated nor underestimated, achieving a reflection fraction close to unity. The analysis shows that the reflection fraction approaches unity as the corona moves farther from the black hole (BH), consistent with expectations. Since a more distant corona scatters fewer photons into the disk, the observed reflection fraction should not exceed 1, contrary to cases where unphysical values (e.g., greater than 10) might arise from model limitations or incorrect assumptions (see, Figure 3 of Dauser et al. 2016). Using multi-instrument observations, we found that the high-state (HS) does not always show a truncated inner radius (R_{in}). For instance, in Observation 5, where *NICER*, *Swift*, and *NuSTAR* were used simultaneously (see Table 2.3), we observed a slightly truncated or even non-truncated R_{in}. I was in charge of reducing and analyzing the observed data in the context of a self-consistent model (described in Chapter 2). I was also in charge of the comparison with other sources in their HS to find one showing similar non-truncated disks, as well as leading the writing of the paper. The general picture of the HS should contain a highly-truncated disk but our self-consistent modeling revealed mild-to-no truncation in this HS.

In the third Chapter, my colleagues and I presented the results of the analysis of the soft-intermediate (SIMS) and soft state (SS) using *NICER* observations. This chapter, which I consider my major work, presents the detection of a self-obscured inner disk in the SIMS of the BHXRB MAXI J1803-298 during its major outburst in 2021 and the presence of disk winds during its SS using *NICER* observations. This source underwent a full outburst. It began in the HS, transitioned to the SIMS, then entered the SS where it lasted several months and then transitioned back to the HS before going quiescent. In highly inclined sources, such as MAXI J1803-298 (>70°), self-obscuration describes a phenomenon in which an outer, typically cooler part of an accretion disk blocks emission from an inner, typically hotter region (see Narayan & Yi 1994; Li et al. 2010; Ponti et al. 2012; Wang et al. 2014). Under certain conditions, the outer disk can puff up, obscuring the X-ray-emitting inner regions for high inclination systems. This may occur due to warping, from radiation pressure instability, or increased thickness due to high accretion rates. At the same time, disk winds are present in the SS that can be studied from Fe XXV and Fe XXVI absorption lines at 6.69 keV and 6.97 keV respectively.

Due to the presence of disk winds, we grouped individual SIMS and SS spectra (more than 90) into 28 merged spectra in order to enhance the detectability of disk winds. During the fitting process we observed a drop in disk temperature by a factor of $\sim$ 2 in the SIMS and an increase in disk normalization (which can be scaled proportionally to R_{in}^2). This behaviour is indicative of a possible disk obscuration. To track the disk winds, we modeled the continuum emission from 2-10 keV and added the so-called `zxipcf` model accounting for the winds, showing a clear wind evolution in the SS fitting result. The evolution has been tracked by looking how the equivalent widths of Fe_{XXV} and Fe_{XXVI} changed over the SS. *NICER* is able to detect line shifts, including below the spectral resolution of 100 eV. The systematic uncertainty in the gain calibration is approximately 30 eV, which makes the results unreliable, even if they are nominally statistically significant. Moreover, the observed line shifts are typically smaller than 30 eV. We presented the equivalent widths to show their evolution (see Figure 3.3.1 in Chapter 3). For the case of self-obscuration, we tracked the disk temperature versus disk normalization (see Section 3.4.1) and compared it with another source (GX 339-4 BHXRB) which makes the transition from the HS to the SS without showing such behavior. On the other hand, we also explored a third source (H1743-322) during three of its outbursts to see if self-obscuration in highly inclined systems is

common for all kinds of outbursts or whether it appears only in major outbursts. Other scenarios have been considered, but the obscuration due to the ejecta of a companion star and disk wind obscuration don't fit in this case as in both scenarios we observe a decrease in disk temperature but not an increase in disk normalization. The timescale for an ejection should be very fast, whereas the timescale of the obscuration is long. SIMS shows there is no absorption line, which implies that there is no wind detection in this transition state. For this second paper, contained in Chapter 2, I reported, as a key point, the detection of a self-obscured inner disk as a consequence of the radiation pressure that caused the disk "to puff up". Further investigation of different highly inclined sources in different outbursts is already underway to follow up on this result. My role in this work was the complete data reduction process, analysis, and writing of the paper.

Finally, in the fourth chapter, contained in Chapter 4, I constrained the spin ($a_\star$) of BHXRB GRS 1716-249 via continuum fitting. Continuum fitting accounts for the thermal emission from the accretion disk which is described by a multi-temperature blackbody spectrum, with the temperature profile determined by the mass accretion rate and the gravitational potential of the BH. The observed disk spectrum can be modeled using relativistic disk models such as `kerrbb` or `kerrbb2`, which account for general relativistic effects, Doppler boosting, and gravitational redshift. I used the new dynamical data of BH mass, inclination of the system and distance obtained in optical observations to obtain the new spin measurement using the `kerrbb2` model (e.g. McClintock et al. 2014; Davis & Hubeny 2006; Li et al. 2005). We made use of one *NuSTAR* observation and three *Swift* observations which match continuum-fitting requirements. For a proper assessment of the measurement uncertainty, we first performed a series of 1000 Monte Carlo (MC) samplings of the dynamical data, which includes the mass, inclination and distance to the BH, and then fit the data with those output values of the MC sampling. The most probable inclination, mass and distance are: $\sim 68°$, $\sim 6.4\ M_\odot$ and ~ 6.9 kpc, respectively, as derived from the near-infrared data. The 1000 fits to *Swift* and *NuSTAR* data using `kerrbb2` showed an upper limit of $a_\star < 0.6$. I was responsible for the data reduction, spectral analysis and uncertainty assessment via MC sampling, and I also led the writeup.

In the remainder of this chapter, I introduce the basic concepts of BHXRBs at different wavelengths, focusing on X-ray wavelengths and a description of the emission processes that dominate in each phase of an outburst. All of these concepts will be revisited and reintroduced in Chapters 2, 3, and 4.

1.2 Black Hole X-ray Binaries

Neutron stars (NSs) and BHs are the most exotic objects in the universe. Particularly, BHs can be defined by the no-hair theorem, i.e., they are completely characterized by their mass, angular momentum and charge. BHs exist across a wide range of masses, from stellar-mass BHs ($\sim 3 - 100 M_\odot$) to supermassive BHs ($\sim 10^6 - 10^{10} M_\odot$). Regardless of their mass, all of their gravitational energy is confined within a region whose radius is at most the Schwarzschild radius, given by $R_S = 2GM/c^2$. This means that the entire mass of the BH is contained within a volume smaller than a sphere of radius R_S, beyond which nothing, not even light, can escape due to the extreme curvature of spacetime. Depending on their mass, BHs can be classified as: stellar-mass (3-100 $M_\odot$), intermediate mass (100-10^5 $M_\odot$) and supermassive BHs ($> 10^5$ $M_\odot$). Supermassive BHs (SMBHs) are found at the center of galaxies, intermediate-mass black holes (IMBHs), with masses in the range of $\sim 10^2 - 10^5 M_\odot$, are thought to form primarily through two main processes: the hierarchical merging of smaller BH (Miller & Colbert 2004; Giersz 2015) and the prolonged accretion of gas and stellar matter (Greene 2020; Mezcua 2017). In

dense stellar environments, such as globular clusters or nuclear star clusters, repeated mergers of stellar-mass BHs can lead to the formation of an IMBH (Portegies Zwart 2004; Fragione 2018). Additionally, runaway collisions of massive stars followed by direct collapse can contribute to their growth (Freitag 2006; Mapelli 2021). The presence and formation mechanisms of IMBHs remain an active area of research in astrophysics. Stellar-mass BHs are found within the galaxies, usually only detected in the form of a binary system although most are thought to be undetected, many likely in the form of an isolated BH with no companion. X-ray binaries (XRBs) are binary systems consisting of an ordinary star and a compact object, which can be a stellar-mass BH or a NS. Those containing a BH are referred to as black hole binaries (BHBs). The compact object is formed by the collapse of the core of a massive star at the end of its (relatively quick) evolution. The gas from the companion star is stripped away and forms an accretion disc around the compact object, where the gas is heated up through viscosity to millions of degrees, causing the gas to emit X-rays. The presence of an accretion disk, coupled with the deep gravitational potential well around the compact object, gives rise to different kinds of outflows, streams of matter launched from different regions of the accretion flow. Outflows are able to carry away from the system a significant fraction of the matter and energy, which could have potentially fallen onto the compact object, so that XRBs act to heat their environment rather than behaving only as sinks. Outflows can take the form of relativistic, transient or persistent collimated jets, but also warm or cold, poorly collimated winds (and essentially anything in between), and are observed in different portions of the electromagnetic spectrum, from the radio wavelengths up to the X-rays (Motta et al. 2021). These systems are usually known as high-mass or low-mass X-ray binary systems (HMXBs or LMXBs). HMXBs were among the very first bright X-ray sources detected and optically identified with a massive companion star. They comprise a compact object orbiting an O or B class star. On the other hand, LMXBs contain a low-mass companion star ($M \leq 1\ M_{\odot}$) and a compact object.

A few dozens of BHXRBs are known at present, and this quantity is expected to increase in the future. Estimates predict between $10^8 - 10^9$ stellar-mass BHs are believed to exist in the Galaxy (e.g., Timmes et al. 1996; Brown & Bethe 1994). Stellar-mass BHs are important for understanding astrophysical processes. They are one endpoint of stellar evolution for massive stars, and the collapse of their progenitor stars enriches the universe with heavy elements (Woosley et al. 2002). Also, the X-rays emitted by these BHs are produced by a disk of accreting gas supplied by the outer layers of its companion star, either from Roche-lobe overflow (Xing et al. 2024) or through stellar wind capture. These are correspondingly perfect candidates for the study of accretion physics and for understanding BH physics. BHXRBs spend most of their time in the quiescent state, making it nearly impossible to detect them until they undergo an outburst, during which we can observe them in all wavelengths. Interpretation of outburst observations allow us to explain different parts and processes in accretion disks (see Figure 1.1). Mass, distance to the BH and inclination, which relates the disk vs the orbit vs the spin, are important parameters to know their luminosity. These parameters can be estimated in different ways, but the most reliable method is through optical observations during the quiescent state, where the accretion rate is low, where the accretion's role is minimized and not observable in any wavelength. The ellipsoidal light curve, exhibiting two maxima and two minima per orbital period is used to obtain the inclination of the system. The radial velocity (RV) and mass function measurements allow us to derive the mass of the BH with the inclination derived from the ellipsoidal light curve . These parameters are crucial to one of the key observational techniques of determining spin (continuum fitting).

Outbursts are commonly described by delineating two main spectral states and two transitional states. At the beginning of the outburst the system enters a hard state (HS), which lasts a couple of weeks increasing its luminosity until it approaches the Eddington luminosity limit. After this short period of time (days-to-weeks), the system rapidly transitions to the soft state (SS), where it typically remains for several months. The transition from HS to SS takes days-to-week thorugh

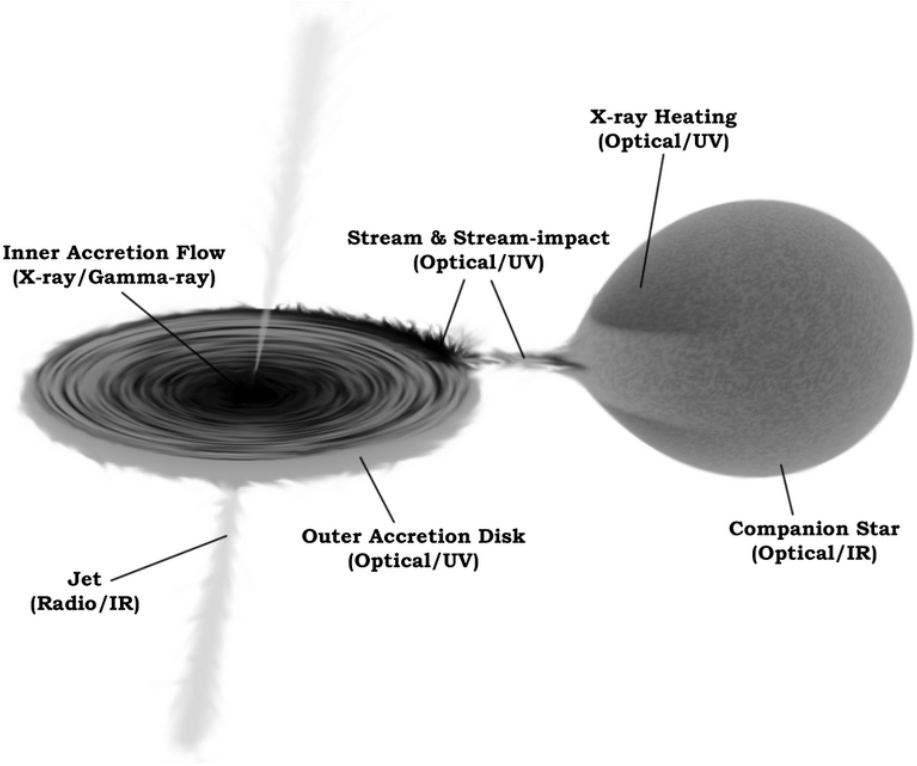

Figure 1.1: Illustration of the different wavelength emission of a BHXRB system (Hynes 2010).

the hard-intermediate state (HIMS) and then to soft-intermediate state (SIMS). Across the SS the accretion disk luminosity decreases until the system transitions back to the HS through SIMS and HIMS. The spectral states of an XRB can be visualized in the hardness intensity diagram (HID) (see Figure 1.2). The HID is a key tool for mapping BHXRBs as HID is very similar for the vast majority of the BHXRBs and it tracks the spectral hardness against the luminosity. The evolution of the HID illustrates the different spectral states and relates to the physical processes involved in each state, such as the accretion mechanism, geometry of the system, and the role of the disk and corona in the emission spectrum.

1.2.1 The Hard State

The HS in BHXRBs is characterized by its unique spectral and physical properties. The primary contribution to the total emission in the HS originates from a thick corona and accelerated particles in presence of a persistent jet. The jet emission is energetically much weaker than the photon luminosity. This emission is mainly non-thermal and spans a broad wavelength range, through radio, infrared (IR), UV-optical, X-ray, and γ-ray bands. The spectral shape is well described by a power law (PL) in X-rays, expressed as:

$$F(E) = KE^{-\Gamma}, \tag{1.1}$$

where $F(E)$ is the photon flux at energy E, K is the normalization constant, and Γ is the photon index. For the HS, Γ is typically ~ 1.7 (Remillard & McClintock 2006), indicating a hard spectral slope.

The HS is observed at the beginning and the end of outbursts in BHXRBs. In the HS of

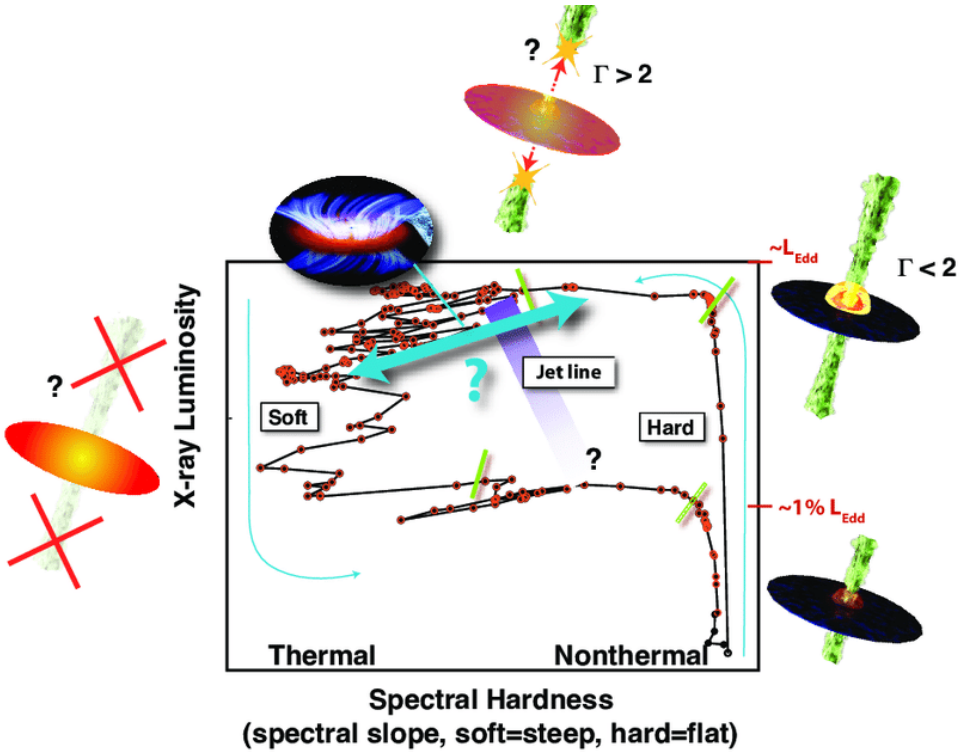

Figure 1.2: Hardness-intensity diagram (HID) illustrating the spectral states of a BHXRB during an outburst. The right side, with a high hardness ratio, corresponds to the HS, dominated by Comptonized emission. The left side, with a low hardness ratio, corresponds to the SS, dominated by thermal disk emission. The transitions between these states occur through the HIMS and SIMS.

BHXRBs, the thermal emission from the inner accretion disk contributes only a small fraction of the total flux. The disk remains cool, with typical inner disk temperatures of $T_{\rm in} \leq 0.2$ keV, while the emission is dominated by non-thermal Comptonized radiation from a hot corona. The inner accretion disk is often thought to be truncated at large radii, around 100 $R_{\rm g}$, rather than extending close to the innermost stable circular orbit (ISCO). This "truncated disk" scenario is supported by spectral and timing studies, which suggest a cooler and less luminous disk at high hardness ratios. However, the extent of disk truncation remains a subject of debate, as some studies propose that the disk could extend closer to the black hole even in the hard state (García et al. 2015; Ubach et al. 2024b). Alternative models, including strong coronal outflows and reflection-dominated inner disk emission, challenge the classical truncation picture. This putative truncation allows the innermost emission region to be dominated by the corona, where Compton scattering of seed photons from the disk occurs, generating a non-thermal spectrum at hard X-ray energies. The corona is located in a hot, optically thin region of the inner edge of the accretion disk with temperatures between $kT_e \sim 50 - 100$ keV, with a high-energy cutoff observed in the spectrum.

The broadband spectrum in the HS also suggests a combination of synchrotron and Compton emission components. The synchrotron emission, observed in radio and IR, is associated with relativistic particles in the persistent jet, while the Comptonized emission in X-rays and γ-rays is thought to arise from interactions between seed photons from the disk and hot electrons in the corona or jet, respectively. A *persistent jet* in BHXRBs refers to a steady, collimated outflow of relativistic particles that remains active over extended periods, typically during the HS. These jets are observed primarily in the radio band and exhibit a flat or slightly inverted spectrum, characteristic of self-absorbed synchrotron emission. Unlike transient jets, which are associated with state transitions and produce bright radio flares, persistent jets maintain a continuous outflow. Their power is correlated with the X-ray luminosity, forming part of the "fundamental plane of black hole activity," which connects jet emission to accretion properties. The base of the jet, sometimes suggested as the locus of the corona, is thought to play a critical role in this process (Kalemci et al. 2005; Markoff et al. 2005).

The connection between the accretion disk and the jet in the HS remains an open question (Remillard & McClintock 2006). Further multi-wavelength observations and theoretical modeling are required to elucidate this relationship and the underlying mechanisms driving the HS in BHXRBs.

Physical Context of the Hard State

In the HS, the accretion flow geometry is significantly different from other states. This corona is often modeled (Czerny et al. 2000) as an Advection-Dominated Accretion Flow (ADAF, e.g. Narayan et al. 1998; Narayan & McClintock 2008) , where a significant fraction of the accretion energy is transported inward by advection rather than radiated locally. The interaction between the corona and the truncated disk is crucial for understanding the hard X-ray emission and the connection between the accretion disk, corona and jet.

Jets and Fundamental Plane Relation

In the HS, jets are persistent and compact, with relativistic particles emitting synchrotron radiation from electrons following the magnetic lines at relativistic velocities. It can be observed in the radio and IR bands. The connection between the jet power and the accretion flow is well established through the so-called *fundamental plane of black hole activity* (Merloni et al. 2003). This empirical relation, which depends on the accretion rate, links the radio luminosity, X-ray luminosity, and the BH mass, suggesting that both the corona and jet are dynamically coupled and regulated by the accretion rate:

$$\log L_{\rm R} = \xi_1 \log L_{\rm X} + \xi_2 \log M_{\rm BH} + \xi_0, \tag{1.2}$$

where $L_{\rm R}$ is the radio luminosity, $L_{\rm X}$ is the X-ray luminosity, $M_{\rm BH}$ is the BH mass, and ξ_i are fitting coefficients. The HS in BHXRBs is a key laboratory to test this relation and, it provides a nearly universal behavior applicable to both stellar-mass and supermassive BHs (Gallo et al. 2003).

Temporal Variability

The hard state exhibits significant temporal variability, with root-mean-square (RMS) amplitudes typically in the range of 20% – 40% (Muñoz-Darias et al. 2010). This variability is dominated by band-limited noise, indicating strong inhomogeneities and instabilities in the accretion flow. Additionally, quasi-periodic oscillations (QPOs) are often observed, with frequencies ranging from ~0.1 to 10 Hz, known as low frequency QPOs (Motta et al. 2015). QPOs and high frequency QPOs are usually detected in the HS or during the intermediate states (HIMS and SIMS), but sometimes can be detected in the SS. There are three types of LFQPOs: type-C, which is the most common QPO detected between 0.1 to 10 Hz with stronger detection from higher-inclination systems. Type-B are often observed in the transition states (close to the jet line in the HID) with frequencies around 6Hz . Type-A QPOs are the least common of these low-frequency QPOs. Type-A QPOs are weak and broad, with frequencies ~6 Hz and are detected in the SS or in the transitional states. These QPOs are commonly thought to arise from precession or oscillations in the corona or the innermost regions of the accretion flow and jet (Ingram & Motta 2019). Type-B QPOs may be related with the jet given their strength in low-inclination (face-on) systems (Kylafis, Nikolaos D. et al. 2020).

1.2.2 The Hard Intermediate State

TheHIMS is a transitional spectral state in BHXRBs observed during the evolution from the HS to the SIMS and, during the reverse transition as the system evolves back to quiescence. The HIMS represents a critical stage in the evolution of the accretion flow, where the properties of the system display a mix of features from the hard and soft states, reflecting changes in the accretion geometry, disk-corona interaction, and jet activity.

Spectral Characteristics

The X-ray spectrum in the HIMS is characterized by the coexistence of a thermal disk component and a hard PL tail. The thermal component, attributed to the accretion disk, becomes more prominent than in the HS, with disk temperatures increasing slightly to $\sim (0.3 - 0.7)$ keV (Homan & Belloni 2005; Skipper & McHardy 2016). The inner edge of the disk is commonly thought to move closer to the innermost stable circular orbit (ISCO), typically at $R_{\rm in} \sim (10 - 20) R_g$, marking the beginning of the transition toward a radiatively efficient flow (Coriat et al. 2011).

The PL component, originating from Comptonization of thermal disk emission in the corona, remains dominant in the total flux. However, the photon index (Γ) softens compared to the HS, with typical values of $\Gamma \sim 1.9 - 2.1$ (Jana et al. 2023). This spectral evolution reflects a reduction in the coronal optical depth or electron temperature as the accretion flow transitions toward the SS. The overall energy spectrum in the HIMS can be modeled using a combination of thermal and non-thermal components, such as `diskbb` that accounts for the multi-temperature blackbody (Mitsuda et al. 1984; Makishima et al. 1986), `simpl` (Steiner et al. 2016 2017), or `nthcomp` that describes the Comptonization of the disk photons (Życki et al. 1999), coupled with relativistic reflection models like `relxill` (Dauser et al. 2013; García & Kallman 2010) for describing reprocessing of coronal emission which illuminates the disk. The relativistic reflection modeling

accounts for disk photons scattered by the corona which go back to the disk and are reprocessed into fluorescent, thermal, and continuum emission. Due the strong gravitational field, the photons are concentrated toward the inner disk.

Timing Properties

The timing characteristics of the HIMS provide critical insights into the dynamical processes in the accretion flow. The root-mean-square (rms) variability in the HIMS decreases compared to the HS, with values typically in the range of 5–15% (Muñoz-Darias et al. 2010). This reduction in variability indicates an increase in the stability of the accretion disk as the system transitions toward the SS.

A hallmark feature of the HIMS is the presence of low-frequency QPOs in the power density spectrum (PDS). Type-C QPOs (Remillard & McClintock 2006), with frequencies ranging from ~0.1 Hz to ~10 Hz, are commonly observed during this state. These QPOs are possibly associated with oscillations in the inner accretion flow, with a popular model relating this to Lense-Thirring precession (Motta et al. 2017) of the hot flow or variations in the disk-corona geometry. The frequency of the QPOs increases empirically as the disk luminosity grows, tracing the gradual evolution of the accretion geometry.

Jet Activity

Jet activity in the HIMS remains significant but shows signs of weakening compared to the HS. Radio observations (Fender et al. 2009) indicate that the compact, steady jets present in the HS begin to decline in strength during the HIMS. The jet spectral energy distribution (SED) transitions from being flat or slightly inverted in the HS to showing signs of steepening, indicating a reduction in particle acceleration efficiency. Transient ejecta, associated with discrete jet-launching events, have rarely been observed (Homan et al. 2020) in few sources during this state, often coinciding with changes in the QPO properties or major spectral transitions.

The connection between the jet, disk, and corona in the HIMS remains an active area of research. Multi-wavelength campaigns combining X-ray and radio observations have revealed correlations between the radio and X-ray flux, providing constraints on the coupling between accretion and jet formation.

Relativistic Reflection and Disk Winds

The HIMS provides a unique opportunity to study relativistic reflected photons from the disk and disk winds in BHXRBs (see Figure 1.3). The Fe Kα emission line, a signature of reflection from the inner accretion disk, becomes increasingly prominent in the HIMS as the disk luminosity grows and the thermal emission strengthens. Detailed modeling of the Fe Kα line profile using relativistic reflection models like `relxill` can constrain the disk inclination, ionization state, and black hole spin.

Disk winds, can be detected as absorption features in the X-ray spectrum, also play a significant role in the HIMS (Homan et al. 2016). These winds, driven by radiation pressure or magnetic fields, provide a mechanism for mass and angular momentum loss from the system. High-resolution spectra from instruments like *Chandra*, *XMM-Newton* and *XRISM* (Sako et al. 2003) have revealed winds with velocities of several thousand kilometers per second, offering insights into the feedback processes in BHXRBs.

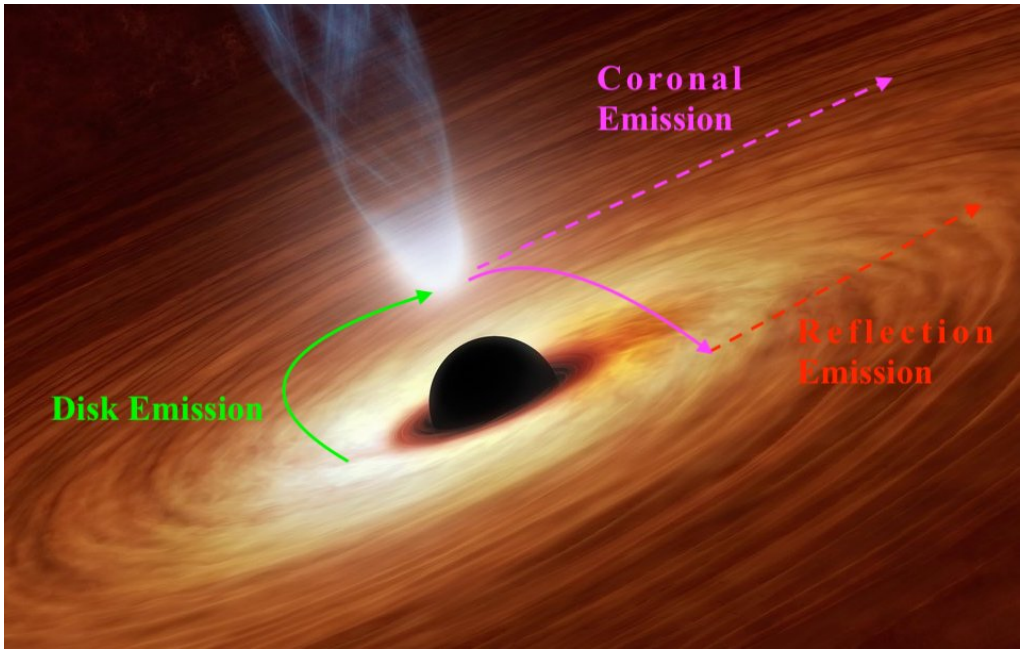

Figure 1.3: Illustration of a black hole accretion disk with its different emission components, including reflection (Courtesy of JPL/NASA).

Comparison with Other States

The duration of the HIMS can be froma few days to a week compared to HS and SS which last a couple of weeks and several months respectively. The HIMS occupies an intermediate position in the evolution of BHXRBs, bridging the HS and the SIMS. Compared to the HS, the HIMS shows a softer spectrum, reduced variability, and weakened jet activity. In contrast, the HIMS differs from the SIMS by its harder spectrum, higher variability, and the continued presence of steady jets. These distinctions highlight the importance of the HIMS as a transition phase in the spectral and timing evolution of BHXRBs.

Theoretical Implications

The HIMS provides a critical testbed for theories of accretion and ejection of accretion disks in BHXRBs. The spectral and timing evolution observed in this state reflects changes in the physical properties of the accretion flow, such as the inner disk radius, the coronal optical depth, and the jet-launching mechanism. The HIMS also offers insights into the interplay between accretion and relativistic jets, as well as the role of disk winds in regulating accretion although unusually seen.

Theoretical models, such as the truncated disk paradigm and magnetohydrodynamic (MHD) simulations, have been developed to explain the observational properties of the HIMS (Marino, A. et al. 2021). These models propose that the accretion flow in the HIMS consists of a geometrically thin, optically thick disk coupled with a hot, geometrically thick inner flow that supports the jet and corona. The gradual transition from a truncated disk in the HS to a full disk in the SS is thought to drive the observed changes in the spectral and timing properties.

1.2.3 The Soft Intermediate State

The SIMS represents a transitional phase in the spectral and timing evolution of BHXRBs. It is observed between the HIMS and the SS during the rise or decay of an outburst. The SIMS

is characterized by rapid changes in the accretion flow geometry, disk-corona interaction, and jet activity (Fan et al. 2024). Its unique spectral and temporal properties provide a crucial window into the physical processes governing these systems during transitions.

Spectral Properties

The X-ray spectrum in the SIMS shows a mix (Remillard & McClintock 2006) of thermal and non-thermal components, with the thermal emission from the accretion disk becoming dominant as the disk gets hotter. The disk component is commonly modeled by `diskbb` or `kerrbb` that accounts for a multi-temperature blackbody of a thin disk around a Kerr black hole (Li et al. 2005), exhibiting temperatures in the typical range of $0.5 - 1$ keV (McClintock & Remillard 2004). This is indicative of a disk extending down to or very close to the ISCO. The inner radius of the disk stabilizes at approximately $R_{\rm in} \sim 6R_{\rm g}$, for a Schwarzschild BH or closer for a Kerr BH if it is in prograde.

The non-thermal component, modeled as a PL or Comptonization (`nthcomp`, `simpl`), contributes a smaller fraction (Dunn et al. 2010) of the total flux compared to the HIMS. The photon index (Γ) steepens further to values between 2.4 and 2.8, reflecting the reduced dominance of the corona as the disk emission increases. The fractional contribution of the PL component to the total flux, in X-rays, typically drops below 30%, evidencing that the corona becomes weaker and the disk soft photons become dominant.

Relativistic reflection features, such as the Fe Kα line and the Compton hump (Kara et al. 2015), are prominent in the SIMS. These features are modeled using relativistic reflection models like `relxill` (Dauser et al. 2016) or `relconv*reflionx` (Dauser et al. 2013; Ross & Fabian 2005), where `relconv` () is a relativistic convolution kernel that incorporates relativistic distortion to the reflection from a hot rotating accretion disk (Dauser et al. 2013). `reflionx` and `relxill` both include computation of the reflection spectrum for an ionized disk, including the Fe-kα (Ross & Fabian 2005). Both models enable measurements of black hole spin, disk inclination, and the ionization state of the accretion disk.

Timing Properties

The timing properties of the SIMS undergo dramatic changes compared to the HIMS. The total rms variability decreases to values of ~ 0.1 (Remillard & McClintock 2006), signaling a further stabilization of the accretion flow. The reduction in variability correlates with the increased dominance of the thermal disk emission, which is inherently less variable.

A defining feature of the SIMS is the transition in the nature of QPOs. Type-C QPOs, observed in the HIMS, disappear, and Type-B QPOs emerge with frequencies typically $\sim 4-6$ Hz (Wijnands & van der Klis 1999; Casella et al. 2005). These Type-B QPOs appear during the short lived SIMS (Motta et al. 2011), and are narrower in frequency. The presence of Type-B QPOs is often associated with the rapid evolution of the inner accretion flow and changes in the coupling between the disk and corona. Their origin is still debated (Liu et al. 2022) but is sometimes linked to instabilities at the interface between the disk and corona or the transition layer of the accretion flow.

The PDS in the SIMS shows weaker noise components compared to the HIMS, with a steep power-law slope of ~ -2 and reduced band-limited noise (Mao & Yu 2021). The overall temporal behavior in the SIMS reflects the transitional nature of the accretion flow as the system approaches the soft state.

Jet Evolution

The SIMS is a critical phase for studying the evolution of jets in BHXRBs. During this state, the compact, steady jets present in the HS and HIMS are suppressed or significantly reduced in activity, and the system enters a phase of transient jet activity. These transient jets are often detected as discrete ejection events at radio and infrared wavelengths, coinciding with significant changes in the X-ray spectrum or the appearance of Type-B QPOs.

The connection between jet ejections and changes in the accretion flow geometry remains an active area of research (Sikora & Zdziarski 2023; Marcel, G. et al. 2018). It is hypothesized (Inoue 2022) that the transition from a truncated disk to a non-truncated disk, coupled with instabilities in the corona, triggers the ejection of material. The transient jets observed during SIMS are relativistic, with velocities approaching $(0.7 - 0.9)c$ (Reig, P. & Kylafis, N. D. 2015), and are thought to represent episodic energy release from the inner accretion flow.

Multi-wavelength campaigns combining X-ray, radio, and infrared observations have been instrumental in probing the coupling between accretion and ejection processes in the SIMS (Echiburú-Trujillo et al. 2024). These studies have revealed tight correlations between the timing of jet ejections and the evolution of X-ray spectral and timing properties, providing constraints on the physical mechanisms driving jet production.

Relativistic Reflection and Disk Winds

The SIMS provides an excellent opportunity to study relativistic reflection and disk winds. The Fe Kα line becomes sharper and more ionized than in the HIMS (Matt et al. 1993), due to the increasing dominance of thermal disk emission and possibly the inward migration of the disk. Reflection modeling in this state can constrain key parameters such as the ionization state of the disk, the height of the corona, and the spin of the black hole.

Disk winds, detected as absorption features in the X-ray spectrum (Ueda et al. 2009), are often prominent in the SIMS. These winds, with velocities ranging from a few hundred to several thousand kilometers per second, are indicative of outflows driven by radiation pressure or magnetic forces (e.g. Chakravorty et al. 2016; Petrucci et al. 2021). High-resolution spectra obtained with instruments like *Chandra*, *XMM-Newton*, *NICER*, *NuSTAR* and *Swift* (Degenaar et al. 2016) have revealed detailed wind properties, such as their ionization state, column density, and velocity structure, providing insights into the feedback processes in BHXRBs.

Comparison with Other States

The SIMS is a short-lived yet critical state that bridges the HIMS and the SS. Compared to the HIMS, the SIMS shows a softer spectrum, reduced variability, and a higher dominance of thermal disk emission. In contrast, the SIMS differs from the SS in its higher variability, the presence of Type-B QPOs, and the occurrence of transient jet activity. These unique characteristics highlight the transitional nature of the SIMS and its importance in the overall evolution of BHXRBs.

Theoretical Implications

Theoretical models of the SIMS emphasize the interplay between accretion, ejection, and radiation in transitional states. The gradual transition from a truncated disk to a full disk, coupled with the evolution of the corona, explains many of the observed spectral and timing properties. MHD simulations (e.g., Dihingia et al. 2023) suggest that instabilities at the inner edge of the disk or in the corona play a key role in driving Type-B QPOs and triggering jet ejections.

The SIMS also offers insights into the mechanisms of jet quenching and the role of magnetic fields in launching and accelerating outflows. Observations of disk winds during the SIMS have

provided constraints on the mass and energy carried away by these outflows, contributing to our understanding of accretion feedback (Petrucci, P.-O. et al. 2021; Parra et al. 2024).

1.2.4 The Soft State

The SS in BHXRBs is defined by a dominance of thermal emission originating from the accretion disk. This state is typically observed during the peak (Remillard & McClintock 2006) of an outburst, where the accretion rate is at its highest. The main characteristics of the SS are the strong multi-temperature blackbody spectrum with temperatures of $T_{\rm in} \sim 1$ keV, associated with the innermost regions of the accretion disk, an inner edge of the disk extended close to the innermost stable circular orbit (ISCO), $R_{\rm in} = 6R_{\rm g}$ for a non-rotating black hole, a weak or absent PL component, with photon indices (Γ) typically > 2.5, and minimal radio emission due to jet suppression.

Spectral Properties

The spectrum in the SS is primarily dominated by the thermal emission from the geometrically thin, optically thick accretion disk. The disk spectrum can be modeled using the standard `diskbb` model, characterized by the following relation for the flux:

$$F_\nu \propto \int_{R_{\rm in}}^{R_{\rm out}} \nu^3 \left[\exp\left(\frac{h\nu}{kT(R)}\right) - 1\right]^{-1} R, dR, \tag{1.3}$$

where h is Planck's constant, k is Boltzmann's constant, ν is the frequency and T(R) follows the standard temperature profile for a thin accretion disk:

$$T(R) = T_{\rm in}\left(\frac{R}{R_{\rm in}}\right)^{-3/4}. \tag{1.4}$$

This approximation is non-relativistic and has an incorrect boundary condition. A better option is `ezdiskbb` (Zimmerman et al. 2005a; Novikov & Thorne 1973a; Page & Thorne 1974) which accounts for multi-temperature blackbody model for a thin, steady-state, Newtonian accretion disk, assuming zero torque at the inner boundary for the disk at radius R_{in}.

The PL component, when present, originates from Comptonization in a weak corona. However, its contribution to the total flux in X-rays is typically less than 20%, indicating that the disk dominates the energy output in this state (Remillard & McClintock 2006).

Temporal Variability

The SS is characterized by low levels of temporal variability, with rms amplitudes less than $< 7.5\%$ (Remillard & McClintock 2006). This stability contrasts with the high variability observed in the HS due to a stable disk at ISCO. QPOs in the SS are rare but, when present, are usually of Type A or C, with frequencies in the range of 1–10 Hz (Motta et al. 2011; Motta et al. 2015; Homan et al. 2020).

Jet Quenching

One of the defining features of the SS is the suppression of jet activity. Radio observations (Russell et al. 2011) show a significant reduction or complete absence of synchrotron emission, suggesting that the physical conditions near the black hole do not support the formation of a compact jet. This quenching of jets has been linked to changes in the geometry and radiative efficiency of the accretion flow (Fender et al. 2004).

Disk Geometry and Accretion Physics

In the SS, the accretion disk is thought to extend down to the ISCO, providing a direct probe of the innermost regions of the black hole's gravitational potential. The high disk temperatures and luminosities imply a radiatively efficient accretion flow, consistent with the standard Shakura-Sunyaev disk model (Shakura & Sunyaev 1973). This model is a foundational framework for modeling accretion disks, offering insight into the disk's structure, temperature distribution, and radiation characteristics. The inner disk radius can be used to estimate the black hole spin if the inclination distance and mass are well constrained (Zhang et al. 1997).

Table 1.1 summarizes the key properties of the different spectral states in BHXRBs.

Table 1.1: Comparison of Properties Across Spectral States

Property	HS	HIMS	SIMS	SS
Spectral Index (Γ)	1.4 – 2.0	2.0 – 2.2	2.2 – 2.5	> 2.5
Variability (RMS)	20% – 40%	5% – 15%	$\sim 0.1\%$	$< 7.5\%$
Jet Presence	Persistent	Persistent	Transient	Absent
Disk Temperature ($T_{\rm in}$)	≤ 0.2 keV	~ 0.5 keV	< 1 keV	~ 1 keV

1.2.5 Black Hole Modeling

BHXRB spectra evolve with their state. The different spectral states of BHXRBs emphasize the importance of BH emission, which consists of both thermal and non-thermal components. Non-thermal emission from the corona is more prominent in the HS and thermal emission from the disk is more prominent in the SS. To model these two main aspects of a BH, both a PL model accounting for the non-thermal emission of the corona and a multicolor-blackbody radiation from the thermal disk model are necessary. Corona models include `nthcomp` and `simpl/simplcut`. Both cases account for the Comptonized continuum. `nthcomp` (Życki et al. 1999) describes the shape of the continuum produced when thermal photons undergo Compton scattering. Instead of a simple exponentially cut-off power law , `nthcomp` provides a more accurate representation of the resulting spectrum. The high-energy cutoff in this model is sharper than a standard exponential cutoff and is determined by the electron temperature (kT_e). Another important effect (especially for XRBs) is that the `nthcomp` model incorporates the low-energy rollover. This model is a physically accurate description of an electron cloud Comptonizing a seed spectrum, which can be taken as either a blackbody or a disk blackbody. It doesn't have the low-energy problem because it is physically anchored, providing a more accurate representation of the emission at these energies. The hot electrons Compton up-scatters seed photons coming from the disk so there are few photons in the scattered spectrum at energies below the typical seed photon energies, making it diverge from a power law below this energy. Typically, the physical picture is that these seed photons are (quasi)blackbody (on NS) or disk blackbody in spectral distribution. Either of these shapes can be selected in the model (input type), both being parameterized by a seed photon temperature (kT_{bb}). Between the low and high-energy rollovers, the shape of the spectrum is determined by the combination of electron scattering optical depth and electron temperature. It is not necessarily a power law, but can be parameterized by an asymptotic power law index (Γ) at low energies. The `simpl` model (Steiner et al. 2009) is an empirical Comptonization model in which a fraction of photons from an input seed spectrum is scattered into a PL component. The seed spectrum consists of soft thermal photons from the accretion disk, which are not Compton-thick and have a spectral index greater than 1. The `simplcut` model is a variant of `simpl` that additionally accounts for the fraction of these Compton-scattered photons that interact with the corona and reflect off the disk. In this model, the reflection fraction and the temperature of the corona are also included.

For the disk modeling, the most common model is `diskbb` (Makishima et al. 1986). Accretion disks emit thermal photons in the form of blackbody radiation. `Diskbb` is a multi-temperature blackbody model. With a combination of thermal and nonthermal (e.g., Comptonization and reflection) continuum models, it is possible to fit a BHXRB spectrum, but particularly in the HS and intermediate states, a Fe-Kα emission line appears in the spectrum due to reflected photons off the disk coming from the corona. For instance, `relxill` and `relxillCp` are the most common models used to characterize the reflection emission. They are standard relativistic reflection models, modeling the irradiation of the accretion disk, the intrinsic reflection, allowing a broken power law emissivity. These flavors of the relativistic models for an incident spectrum differ by either using an exponential high-energy cutoff power law or an `nthcomp` Comptonization continuum. Furthermore, the `relconv` component, which is part of the `relxill` model, accounts for the convolution of the reflection line in the spectrum. This is an essential distinction, as it provides the necessary adjustment to the reflection component. On the other hand, `reflionx` (Ross & Fabian 2005) is a separate model that calculates the reflection spectrum from an ionized disk, including the Fe Kα lines.

1.3 Radio observations

Radio observations of BHXRBs provide crucial insights into jet activity and the underlying accretion processes. These observations primarily probe synchrotron emission from relativistic particles in the jets and offer a unique perspective on the connection between the accretion disk and outflows.

1.3.1 Physical Processes

Radio emission in BHXRBs is closely coupled to their jet properties. Here we describe the jet properties including radio emission associated with the jet:

- **Synchrotron Radiation:** Electrons accelerated to relativistic speeds in the magnetic fields of the jet emit synchrotron radiation. The observed spectrum typically follows a PL form:

$$S_\nu \propto \nu^\alpha, \tag{1.5}$$

  where S_ν is the flux density, ν is the frequency, and α is the spectral index. For compact self-absorbed jets in the hard state, $\alpha \sim 0$, whereas optically thin emission in transient jets during the intermediate states has $\alpha < 0$ (Fender 2001).

- **Jet Formation:** The presence of compact steady jets in the hard state ((Miller-Jones et al. 2008; Miller-Jones et al. 2011)) is associated with the geometry of the accretion flow. The truncated disk allows for the formation of a hot magnetized corona that launches the jets via mechanisms such as Blandford-Znajek or Blandford-Payne (Blandford & Znajek 1977; Blandford & Payne 1982). These are candidate mechanisms for the extraction of energy from a rotating BH.

- **Jet Quenching:** In the soft state, the jet emission is suppressed or absent. This phenomenon is attributed to changes in the inner disk structure and the cooling of the corona, which disrupt the conditions necessary for jet formation (Fender et al. 2004).

- **Radiative Cooling:** Synchrotron cooling and adiabatic expansion of the jet contribute to the observed evolution of the radio spectrum, particularly in transient jets. The cooling timescales and spectral steepening provide information on the energy distribution of the jet particles and the magnetic field strength.

1.3.2 Radio Emission Across Spectral States

The behavior of radio emission varies significantly across the spectral states of BHXRBs. During the HS, compact jets produce flat-spectrum radio emission ($\alpha \sim 0$). The radio luminosity correlates with the X-ray luminosity following the fundamental plane of black hole activity (Eq. 1.2). In SIMS, transient jets are observed, often associated with discrete ejections during state transitions. These jets produce optically thin synchrotron radiation (Russell et al. 2013) with steep spectra ($\alpha < 0$). The suppressed radio emission is indicative of jet quenching, typical of the SS. This state highlights the strong connection between the accretion flow and jet activity.

1.3.3 Key Observations

Radio monitoring of BHXRBs has revealed several important phenomena. The evolution of radio emission tracks the spectral state transitions, showing correlation between outflow properties and the X-ray states which can be used to understand accretion-outflow coupling. Ejection events during intermediate states, in the form of bright radio flares, indicate the launch of relativistic jets, accompanied by X-ray variability. Polarimetric observations of radio jets reveal the magnetic field structure and confirm synchrotron radiation as the dominant emission mechanism (Bolis et al. 2024).

1.4 Infrared observations

IR observations of BHXRBs offer unique insights into the processes occurring in the accretion flow, the jets, and the donor star. IR wavelengths probe a diverse range of physical phenomena, including thermal emission from the disk, synchrotron radiation from jets, and blackbody radiation from the companion star.

1.4.1 Physical Processes

The key physical mechanisms contributing to IR emission in BHXRBs are as follows:

- **Thermal Emission from the Accretion Disk:** The outer regions of the accretion disk emit predominantly in the IR when the source is active. This thermal emission follows a blackbody spectrum and depends on the temperature profile of the disk. The thermal emission flux density can be approximated by:

$$F_{\rm disk}(\nu) \propto \int_{R_{\rm in}}^{R_{\rm out}} B_\nu(T(r)) 2\pi r \, dr, \tag{1.6}$$

  where $B_\nu(T(r))$ is the Planck function, and $T(r) \propto r^{-3/4}$ is the temperature profile of the disk (Shakura & Sunyaev 1973).

- **Synchrotron Radiation from Jets:** Relativistic electrons in the magnetic fields of the compact jets emit synchrotron radiation, which contributes significantly to the IR spectrum in the HS (Corbel & Fender 2002). The spectral index of this emission depends on whether the jet is optically thick or thin:

  - Optically thick: $F_\nu \propto \nu^\alpha$, with $\alpha \sim 0$.
  - Optically thin: $F_\nu \propto \nu^\alpha$, with $\alpha < 0$.

IR observations, combined with radio and optical data, help constrain the spectral break frequency that marks the transition from optically thick to thin synchrotron emission (Russell et al. 2012).

$$F_\nu \propto \begin{cases} \nu^{\alpha_{\text{thick}}}, & \nu < \nu_{\text{break}} \\ \nu^{\alpha_{\text{thin}}}, & \nu > \nu_{\text{break}} \end{cases} \tag{1.7}$$

where F_ν is the flux density at frequency ν, $\alpha_{\text{thick}} \approx +2$ (spectral index for optically thick synchrotron emission), $\alpha_{\text{thin}} \approx -0.6$ to -0.8 (spectral index for optically thin synchrotron emission), ν_{break} is the spectral break frequency (-0.6 to -0.8).

- **Blackbody Emission from the Companion Star:** In some BHXRBs, the donor star's thermal emission contributes to the IR spectrum. This emission is particularly significant in systems with a low-mass donor, where the star dominates the near-IR flux in quiescence state.

1.4.2 Infrared Emission Across Spectral States

The IR properties of BHXRBs vary significantly depending on their spectral state. In HS, compact jets dominate IR emission via synchrotron radiation (Gandhi et al. 2011). The IR flux correlates with the radio flux and provides insight into jet power and particle acceleration. During intermediate states, transient jets can contribute to IR flares, with optically thin synchrotron emission producing steep spectra. These flares often coincide with state transitions and are linked to discrete ejection events. In the SS the IR emission is dominated by the outer accretion disk. Jets are quenched in this state, leading to a significant reduction in non-thermal IR flux.

1.4.3 Observational Signatures

Infrared observations provide several key signatures of the physical processes in BHXRBs:

- **Spectral Breaks:** The transition between optically thick and thin synchrotron emission is observed as a spectral break typically in the IR. This break frequency provides constraints on the jet geometry and magnetic field strength (Migliari et al. 2006; Gandhi et al. 2011; Pal et al. 2016a).
- **Polarization:** Synchrotron radiation is linearly polarized. IR polarimetry can probe the magnetic field orientation and strength in the jet (Russell & Fender 2008; Shahbaz et al. 2008; Russell 2018).
- **Time Lags:** Variability studies across IR, optical, and X-ray bands reveal time lags that trace the propagation of energy through the accretion flow and jet (Casella et al. 2010; Casella et al. 2010; Malzac et al. 2018).
- **Correlations with X-rays:** In the hard state, the IR and X-ray fluxes are correlated, reflecting the coupling between the accretion disk and the jet (Coriat et al. 2009).

1.4.4 Key Observations

IR studies have significantly advanced our understanding of BHXRBs. Notable findings include that the jet power in the IR correlates with the X-ray luminosity (John et al. 2024), allowing indirect estimates of jet power and efficiency. The disk-jet connection in spectral and timing studies

(Lucchini et al. 2020) have revealed how the accretion flow transitions affect jet production. Near-IR observations, dominated by the donor star in quiescence, have been used to estimate orbital parameters and the system's distance (see Orosz et al. 2002).

1.5 UV-optical observations

Ultraviolet (UV) and optical observations of BHXRBs provide critical insights into the accretion processes, donor star characteristics, and reprocessing of high-energy radiation. These wavelengths probe the cooler regions of the accretion disk, emission from the companion star, and the reprocessed emission of X-rays in the outer disk.

1.5.1 Physical Processes

The main contributors to UV and optical emission in BHXRBs are:

- **Thermal Emission from the Accretion Disk:** The outer regions of the accretion disk emit in the optical and UV due to their lower temperatures compared to the inner disk. The temperature profile of the disk is described by:

$$T(r) \propto \left(\frac{\dot{M}}{r^3}\right)^{1/4}, \tag{1.8}$$

  where $\dot{M}$ is the mass accretion rate and r is the radial distance (Pal et al. 2016b). The UV and optical fluxes depend on the disk's effective temperature and size:

$$F_{\rm disk}(\nu) \propto \int_{R_{\rm in}}^{R_{\rm out}} B_\nu(T(r)) 2\pi r \, dr, \tag{1.9}$$

  where $B_\nu(T)$ is the Planck function.

- **Reprocessing of X-ray and UV radiation:** High-energy photons from the inner disk or corona are reprocessed by the cooler outer disk or companion star surface, producing UV and optical emission. The outer disk absorbs these emissions and re-emit them at lower energies. The reprocessed flux depends on the irradiation geometry and efficiency (Veledina et al. 2011).

- **Blackbody Emission from the Companion Star:** In some BHXRBs, the donor star contributes significantly to the optical spectrum. The stellar flux can dominate at longer wavelengths, particularly in LMXBs.

- **Non-thermal Emission:** In some systems, synchrotron radiation from jets may contribute to the optical and UV emission, particularly during state transitions or flares (Yang et al. 2022a).

1.5.2 UV and Optical Emission Across Spectral States

The UV and optical properties of BHXRBs vary significantly depending on their spectral state:

- **Hard State:** The optical and UV fluxes are often dominated by synchrotron radiation from jets and thermal emission from the outer disk. Reprocessing of X-rays in the outer disk also contributes (Yang et al. 2022a; Veledina et al. 2011).

- **Intermediate States:** The optical and UV fluxes increase during state transitions due to enhanced disk heating and transient jet activity. Flares and spectral variability are common (Liu, Z. et al. 2023a).
- **Soft State:** The optical and UV emission are dominated by thermal emission from the irradiated accretion disk (Anastasopoulou et al. 2022).
- **Quiescence State:** The donor star may also contribute to the optical spectrum, particularly in quiescent periods.

1.5.3 Observational Signatures

UV and optical observations provide key signatures of the physical processes in BHXRBs:

- **Double-peaked Line Profiles:** Optical emission lines, such as Hα and He II, often exhibit double-peaked profiles indicative of a Keplerian disk. A Keplerian disk refers to an accretion disk in which the motion of the orbiting material follows Kepler's laws of planetary motion and are typically found in compact objects.
- **Time Lags:** The delay between X-ray and UV/optical variability is linked to the reprocessing timescale in the outer disk. This lag can be used to constrain the disk size and geometry (Lewin et al. 2023).
- **Polarization:** Scattering and synchrotron processes can produce polarized emission in the optical and UV bands. Polarimetric studies help to probe the disk geometry and magnetic fields (Kravtsov et al. 2022).
- **Spectral Variability:** Changes in the UV/optical continuum and line fluxes reveal variations in the accretion rate, jet activity, and reprocessing efficiency (Liu, Z. et al. 2023b).

1.5.4 Key Insights from UV and Optical Observations

UV and optical studies have significantly advanced our understanding of BHXRBs. Notable findings include:

- **Accretion Disk Structure:** Spectral energy distributions (SEDs) in the UV and optical have been used to constrain the disk's temperature profile and outer radius (Oda et al. 2019).
- **Irradiation Effects:** UV/optical flux measurements confirm that X-ray irradiation is a key driver of emission in the outer disk (Yao & Feng 2019).
- **Jet Contributions:** Spectral and timing studies have revealed the role of jets in contributing to optical and UV emission, particularly during state transitions (Cassatella et al. 2012).
- **Binary Parameters:** Optical observations of the donor star and disk provide estimates (in quiescence state) of the orbital period, inclination, and mass function of the binary (Deloye et al. 2008; Heida et al. 2017).

UV and optical observations will remain essential tools for understanding the physics of BHXRBs, offering complementary insights to those obtained at X-ray and radio wavelengths.

1.6 X-ray observations

X-ray observations of BHXRBs provide unparalleled insights into the physics of accretion and jet formation in strong gravitational fields. The X-ray regime is dominated by emission from the innermost regions of the accretion disk, the corona, and, in some cases, from the relativistic jet. These observations probe the dynamics and energetics of matter in extreme conditions, enabling studies of the accretion flow, black hole spin, and high-energy processes. X-ray observations are the main constituent of this thesis as most of my work is focused on X-ray observations using *NICER*, *NuSTAR*, *Swift* and *Chandra*. Other telescopes have been used in other wavelengths as a secondary goal of this thesis, which is multi-wavelength studies of BHXRBs.

1.6.1 Primary X-ray Emission Mechanisms

The X-ray emission in BHXRBs arises from several key physical processes:

- **Thermal Emission from the Accretion Disk:**

$$F(E) = \int_{R_{\rm in}}^{R_{\rm out}} 2\pi r\, B(E, T(r))\, dr \tag{1.10}$$

  where B(E, T(r)) represents the Planck's function, R_{in} is the inner radius and R_{out} is the outer radius of the accretion disk.

- **Comptonization in the Corona:** The hot, optically thin corona surrounding the accretion disk IC scatters soft seed photons from the disk to higher energies. The resulting spectrum at high energies follows a PL with a high-energy cutoff, characterized as an approximation:

$$A(E) = K E^{-\Gamma} \exp\left(-\frac{E}{E_{\rm cut}}\right), \tag{1.11}$$

  where Γ is the photon index, and $E_{\rm cut}$ is the cutoff energy which is related to the electron temperature of the corona (Steiner et al. 2009). This component generally dominates in the hard state and contributes significantly in the intermediate states.

- **Relativistic Reflection:** Hard X-ray photons emitted by the corona irradiate the accretion disk, producing a reflection spectrum that includes fluorescent emission lines (e.g., Fe Kα at 6.4–7.0 keV), the Compton hump (20–30 keV), and an absorption edge. The reflection spectrum is strongly influenced by relativistic effects such as gravitational redshift, Doppler broadening in strongly curved spacetime, and light bending. These effects produce a broadened and skewed Fe Kα line, which serves as a diagnostic of the disk's inner radius and the black hole spin (Fabian et al. 1989). The reflection spectrum is modeled using components like `relxill` (García et al. 2014) or `reflionx` (Dauser et al. 2013).

- **Jets and Non-thermal X-rays:** In the HS, synchrotron and synchrotron self-Compton (SSC) processes from jets may contribute to the X-ray emission, particularly in the low-luminosity regime (Gardner & Done 2013; Russell et al. 2010). This emission is typically non-thermal and shows a flat or slightly rising spectrum.

1.6.2 Spectral Fitting Techniques

X-ray spectral fitting is crucial for disentangling the contributions of various emission components in BHXRBs. The main approaches include:

Continuum Fitting Method

The continuum fitting method uses the thermal emission from the accretion disk to estimate the spin of the BH. The disk's inner radius is assumed to coincide with the ISCO, which depends on the spin parameter (a_*). The observed disk spectrum is modeled with relativistic corrections using components like `kerrbb2` (McClintock et al. 2014), which accounts for BH spin, disk inclination, and mass accretion rate. The relativistic accretion-disk model `kerrbb2` (McClintock et al. 2006). `kerrbb2` merges two different disk models, `bhspec` and `kerrbb`. Specifically, `bhspec` is used to determine the value of the spectral hardening factor $f \equiv T_{col}/T_{eff}$ (also known as the color correction factor, Davis et al. 2005), while `kerrbb` employs ray-tracing computations to model the disk (Li et al. 2005). The luminosity and temperature profile are related by:

$$L \propto R_{\rm in}^2 T_{\rm eff}^4 , \tag{1.12}$$

where $R_{\rm in}$ is the inner disk radius and $T_{\rm eff}$ its effective temperature.

Relativistic Reflection Fitting

Relativistic reflection fitting involves modeling the broadened and skewed Fe Kα line and the reflection continuum to measure the black hole spin, disk inclination, and ionization state. Components like `relxill` combine relativistic ray-tracing calculations with atomic reflection models, providing constraints on the spin parameter a_* and the disk's ionization parameter ξ, defined as:

$$\xi = \frac{4\pi F_X}{n_e}, \tag{1.13}$$

where F_X is the incident X-ray flux, and n_e is the electron number density of the disk.

Coronal Properties from High-energy Cutoff

The cutoff energy in the power-law spectrum provides information about the electron temperature (kT_e) in the corona. Models such as `nthcomp` or `simpl` describe the Comptonization process, allowing constraints on kT_e and the optical depth (τ).

1.6.3 Temporal Analysis of X-ray Variability

Temporal studies of X-ray light curves reveal critical information about accretion dynamics:

- **Power Spectral Density (PSD):** The PSD is characterized by broad noise components and narrow features, such as quasi-periodic oscillations (QPOs). These features are commonly linked to instabilities in the disk or Lense-Thirring precession (Ingram et al. 2009).
- **Time Lags:** Time lags between soft and hard X-ray variability constrain the size and geometry of the corona and its connection to the disk (Uttley & Malzac 2023).
- **Spectro-temporal Correlations:** Simultaneous spectral and timing studies provide insights into state transitions and disk-jet coupling (Radhika & Nandi 2014).

1.6.4 Future Prospects for X-ray Observations

Next-generation X-ray observatories, such as *XRISM* (Team 2020), *Athena* (Barcons et al. 2012), and *AXIS* (Reynolds et al. 2023), will provide unprecedented capabilities for BHXRB studies:

- **High-resolution Spectroscopy:** Observations of the Fe Kα line and other reflection features will provide precise measurements of black hole spin, disk inclination, ionization state and wind components. However, an improvement comes from the secondary ability to disentangle narrow/distant reflection from broadened/close-in reflection.

- **Time-resolved Spectroscopy:** Improved time resolution will allow detailed studies of state transitions, QPOs, and disk instabilities. However, non of these new instruments has improved the resolution over present instruments. The large collecting area with *Athena* can improve reverberation studies.

- **Polarimetry:** X-ray polarimetry provides a powerful diagnostic tool for studying the geometry of the corona and its relation to the accretion disk and jet. Missions such as the *Imaging X-ray Polarimetry Explorer* (*IXPE*) offer new insights by measuring the polarization degree and angle of X-ray emission in black hole X-ray binaries.

  Polarimetry can help constrain the physical properties of the corona by determining whether the X-ray emission is predominantly scattered or originates from a specific geometry (e.g., a slab-like or spherical corona). Additionally, it allows for a direct comparison between the inferred corona orientation and the known alignment of the relativistic jet with the accretion disk. Such measurements are crucial for understanding disk-jet coupling and the role of magnetic fields in black hole accretion systems.

X-ray observations remain a cornerstone of BHXRB research, offering unique insights into the interplay of accretion, relativistic effects, and jet formation in strong gravitational fields. Most of the emission from active BHXRBs comes out in the X-ray bandpass.

1.7 γ-ray observations

γ-ray observations of BHXRBs probe the most energetic processes in these systems, including particle acceleration, jet formation, and high-energy radiative mechanisms. Emission in this energy band provides critical insights into the non-thermal processes associated with the corona, relativistic jets, and interactions of accelerated particles with the surrounding environment (Romero, G. E. et al. 2010; Barkov et al. 2012).

1.7.1 Origin of γ-ray Emission

γ-ray emission in BHXRBs can arise from a variety of mechanisms (see Bordas 2009):

- **Inverse Compton (IC Scattering:** High-energy electrons in the corona or jet up-scatter low-energy seed photons (from the accretion disk, the companion star, or synchrotron emission) to γ-ray energies. This is a dominant mechanism of γ-ray production, described by:

$$E_{\rm out} \sim \gamma^2 E_{\rm in} \,, \tag{1.14}$$

  where γ is the Lorentz factor of the electrons, only if the electrons are directed toward the observer and $E_{\rm in}$ and $E_{\rm out}$ are the energies of the seed and scattered photons, respectively.

- **Synchrotron Self-Compton:** Electrons accelerated in jets produce synchrotron emission, which is then up-scattered to γ-ray energies by the same electron population. This mechanism is prevalent in compact jets during the HS.

- **Hadronic Processes:** In high-energy jets, protons accelerated to relativistic speeds interact with ambient matter or photons, producing neutral pions that decay into γ rays:

$$\pi^0 \rightarrow \gamma + \gamma \ . \tag{1.15}$$

  These interactions also produce secondary particles such as neutrinos (Bednarek & Protheroe 1999; Sahakyan 2018), making multi-messenger observations critical for constraining hadronic contributions.

- **Pair Production and Annihilation:** At γ-ray energies above 511 keV, photon-photon interactions can lead to pair production:

$$\gamma + \gamma \rightarrow e^+ + e^- \ . \tag{1.16}$$

  Conversely, annihilation of these pairs can generate γ-ray photons at characteristic energies of 0.511 MeV.

- **Interactions with Stellar Winds:** In HMXB systems with strong winds, γ-rays can be generated through IC scattering off photons from the stellar wind or from proton-proton collisions in dense wind regions (Araudo et al. 2011; Koljonen et al. 2018a).

1.7.2 γ-ray Spectral Features

Gamma-ray spectra in BHXRBs are characterized by distinct components linked to the underlying physical processes (see review Bu & Zhang 2023):

- **High-energy Cutoff:** In the HS, the γ-ray spectrum typically displays a power-law shape with an exponential cutoff, reflecting the maximum energy of coronal electrons:

$$F(E) \propto E^{-\Gamma} \exp\left(-\frac{E}{E_{\rm cut}}\right) \ . \tag{1.17}$$

  Typical cutoff energies range from tens to hundreds of keV (Zdziarski & Gierliński 2004), providing constraints on the coronal electron temperature. In the SIMS, this PL, also display a PL shape (Grove et al. 1997; Maccarone et al. 1999).

- **Broad-band Synchrotron and SSC Emission:** γ-ray emission in jets extends as a power-law spectrum, often blending seamlessly with X-ray synchrotron and SSC components. The typical spectral index for synchrotron radiation is $\alpha \approx 0.75$ which corresponds to $\Gamma = \alpha + 1$ (Kataoka et al. 1999).

- **Pion Decay Signatures:** Hadronic γ-ray emission is characterized by a distinct spectral shape, including a bump near $\sim$ 100 MeV from neutral pion decay (Malyshev et al. 2015).

- **Annihilation Line:** γ-ray observations may reveal a narrow feature at 511 keV, indicating electron-positron annihilation in the corona or jet but not detected reliably.

1.7.3 Temporal Variability in γ-rays

γ-ray variability provides valuable clues about the size and dynamics of emitting regions:

- **State-dependent Variability:** γ-ray flux and spectrum evolve with the spectral state of the BHXRB. The HS shows strong, steady γ-ray emission likely linked to jets, while the soft state is typically quiescent in γ-rays due to jet suppression (see 1.2.4).

- **Flares and Transients:** Episodic γ-ray flares are often associated with rapid changes in jet power, magnetic reconnection, or shocks in the outflow (Gandhi et al. 2011; Liu, Z. et al. 2023a; Bolis et al. 2024).
- **Correlations Across Wavelengths:** Simultaneous multi-wavelength observations reveal correlations between γ-ray and X-ray variability (Malzac et al. 2005; Kalemci et al. 2016), shedding light on the coupling between the corona, disk, and jet. Radio and IR observations are also used for a broadband SED, jointly with X-ray and γ-ray as jet probes.

1.7.4 Observational Techniques and Instruments

γ-ray observations of BHXRBs are conducted using space-based telescopes and ground-based facilities:

- **Space-based γ-ray Observatories:** Instruments like *Fermi*-LAT[1] with an energy range of 20 MeV - 300 GeV and an angular resolution of <3.5° at 100 MeV and <0.15° above 10 GeV. *INTEGRAL*[2] with an energy range of 3 keV to 10 MeV and an angular resolution of 12' for γ-ray sources. *CGRO/COMPTEL*[3] has an energy range of 0.75 to 30 MeV and angular resolution of 1°. These instruments have been pivotal in detecting and characterizing γ-ray emission in BHXRBs. These observatories provide broad energy coverage and high sensitivity to non-thermal processes.
- **Ground-based γ-ray Observatories:** Cherenkov telescopes such as H.E.S.S. (Aharonian et al. 2006), MAGIC (Aleksić et al. 2016), and VERITAS (Park 2015) can detect very high-energy (VHE) γ-rays (> 100 GeV) from BHXRBs. These telescopes rely on the detection of Cherenkov radiation produced when γ-rays interact with the Earth's atmosphere.

1.8 Instruments

In this thesis I used telescopes operating at different wavelengths with a main focus on X-ray observatories. In radio, I used data from *ATCA*, *Fermi-LAT* for γ-rays and data taken with the *Magellan telescope* (UV-optical) of a proposal for a multi-wavelength observation purpose. In X-rays, I used the observatories *NICER*, *Swift*, *NuSTAR*, *Chandra* and *MAXI* as a major part of my thesis.

1.8.1 The NICER Telescope: An Overview

The *Neutron Star Interior Composition Explorer* (NICER) is an X-ray telescope installed on the International Space Station (ISS) that was launched on June 3, 2017, as part of NASA's Explorer program (see Figure 1.4). NICER is specifically designed to study extreme environments around compact objects, such as neutron stars and black holes, by providing high-resolution timing and spectroscopic data in the soft X-ray band (0.2–12 keV). Although its primary focus is on neutron stars, NICER has proven to be a powerful tool for studying BHXRBs, offering unique insights into accretion processes, relativistic effects, and variability.

NICER's primary science goals include constraining the equation of state (EoS) of ultra-dense matter by measuring the mass and radius of neutron stars with high precision.

[1] https://fermi.gsfc.nasa.gov/
[2] http://www.esa.int/science/integral
[3] https://heasarc.gsfc.nasa.gov/docs/cgro/comptel/

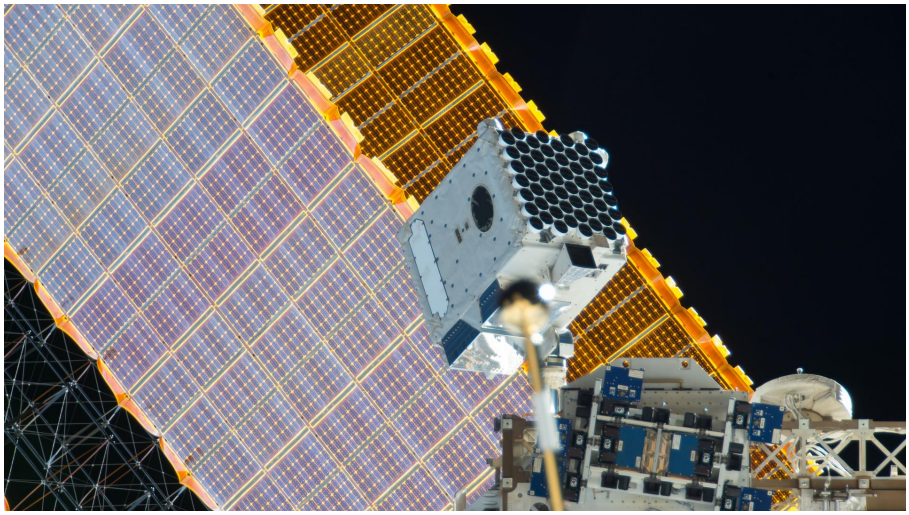

Figure 1.4: Picture of *NICER* mounted on the ISS. Credit: NASA ID iss057e055490

NICER is a non-imaging telescope equipped with an advanced X-ray Timing Instrument (XTI), which consists of an array of 56 co-aligned X-ray concentrators and silicon drift detectors with a characteristic FOV of 5 arcmin but only 52 are functioning since launch. The XTI design allows NICER to achieve sub-microsecond timing accuracy, making it capable of detecting rapid variability from compact sources. The silicon drift detectors provide an energy resolution of approximately 85 eV at 1 keV, enabling detailed spectroscopic studies of emission lines, such as the Fe Kα line.

For studies of BHXRBs, NICER offers several advantages. Its high time resolution enables the detection of fast variability, such as QPOs and rapid fluctuations associated with the inner regions of the accretion flow. The telescope's broadband spectroscopy provides detailed coverage of both thermal and non-thermal emission components, while its high sensitivity to soft X-rays makes it particularly effective in observing thermal emission from accretion disks. NICER's flexibility in scheduling observations, given its location on the ISS, enables rapid-response observations, enabling monitoring campaigns with high throughput of transient events such as outbursts, ensuring critical phases are captured.

NICER has already made significant contributions to BHXRB research. Observations have revealed intricate couplings between accretion disks and coronae, including the detection of time lags between thermal and Comptonized components (Wang et al. 2022). Through its ability to resolve relativistic Fe Kα lines, NICER has provided constraints on black hole spin and accretion disk geometry (Kumar et al. 2022). The telescope has also been instrumental in tracking spectral and timing evolution during state transitions (Alabarta et al. 2020), offering insights into accretion flow dynamics and jet suppression mechanisms. Additionally, NICER's sensitivity to soft X-rays has enabled precise measurements of disk temperatures and inner disk radii (Miller et al. 2018), which are critical for continuum fitting techniques.

In summary, NICER is a groundbreaking tool for studying compact objects, offering unmatched capabilities in time-resolved soft X-ray spectroscopy.

1.8.2 The Swift Telescope: An Overview

The *Neil Gehrels Swift Observatory*, commonly referred to as *Swift*, is a multi-wavelength space observatory launched by NASA on November 20, 2004 (see Figure 1.5). Originally designed to study gamma-ray bursts (GRBs), Swift has evolved into a versatile platform for observing a

wide range of astrophysical phenomena, including BHXRBs. Its ability to perform rapid-response observations and multi-band monitoring makes it a critical tool for exploring transient and variable sources in the universe.

Swift is equipped with three primary instruments that operate across a broad energy spectrum, from ultraviolet (UV) to hard X-rays. These are the Burst Alert Telescope (BAT), the X-ray Telescope (XRT), and the Ultraviolet/Optical Telescope (UVOT). The BAT operates in the 15–150 keV energy range and is designed to detect GRBs and other high-energy transients. Once a transient event is detected with BAT, Swift autonomously slews to the source, allowing XRT and UVOT to begin pointed follow-up observations. The XRT, operating in the 0.3–10 keV energy range, with energy resolution of 190 eV at 10 keV and 50 eV at 0.1 keV, has an angular resolution of 18 arcseconds, provides high-sensitivity X-ray imaging and spectroscopy, while the UVOT extends the wavelength coverage into the optical and UV bands, allowing for multi-wavelength studies of accreting systems.

For BHXRBs, Swift's multi-wavelength capabilities are particularly valuable. The BAT is is often used to track hard states and state transitions. The XRT offers detailed observations of the soft X-ray emission, including thermal components from the accretion disk and relativistic reflection features. The UVOT enables the simultaneous study of optical and UV emission, which is often associated with reprocessed radiation from the accretion disk or the companion star. This comprehensive wavelength coverage allows Swift to study BHXRBs and track their spectral evolution across state transitions.

One of Swift's most critical features is its rapid-response capability. The telescope can autonomously slew to a target within minutes of detecting an event, enabling the observation of the early phases of outbursts or other transient phenomena. This rapid response is particularly useful for detecting new BH transients as they emerge, where the evolution of spectral states occurs on longer timescales (weeks-to-months). Swift's ability to perform long-term monitoring also makes it ideal for tracking the variability of persistent sources or observing recurring outbursts over time.

In the X-ray band, Swift's XRT is a powerful tool for studying accretion physics. The XRT's spectroscopic capabilities allow for detailed modeling of the thermal emission from the disk and non-thermal components from the corona. Observations with Swift have been used to constrain the geometry of the accretion flow and measure inner disk radii using continuum fitting techniques. The study of relativistic reflection features such as the Fe Kα line (García et al. 2019; Kumar 2024) is a complement to other telescopes such as *NuSTAR* and *NICER*. The timing capabilities of the XRT have also been used to detect QPOs (Huppenkothen et al. 2017), which provide insights into the dynamics of the innermost regions of the accretion disk and the effects of strong gravity near the BH. The different modes present different timing resolution. For window timing (WT), the timing resolution is 1.7ms, for photon counting mode (PC) is 2.5s and for burst mode is 0.1ms.

Swift's UVOT adds another dimension to the study of BHXRBs by probing the optical and UV emission. This emission can originate from the companion star, the outer regions of the accretion disk, or reprocessed X-rays. By combining UVOT data with XRT and BAT observations, Swift enables a multi-wavelength approach to understanding accretion and jet physics. For instance, UVOT observations have been used to study the reprocessing of X-ray emission by the outer disk, providing constraints on the geometry and albedo of the disk (Gierliński et al. 2009). In some cases, UVOT data have also been used to detect the presence of winds or outflows from the accretion disk (Yang et al. 2022b).

Swift has made significant contributions to the study of BHXRBs, including the detection of numerous outbursts, detailed monitoring of state transitions, and multi-wavelength studies of jet-disk interactions. Observations with Swift have provided key insights into the coupling between the disk, corona, and jet, as well as the effects of changes in the accretion rate on the emitted

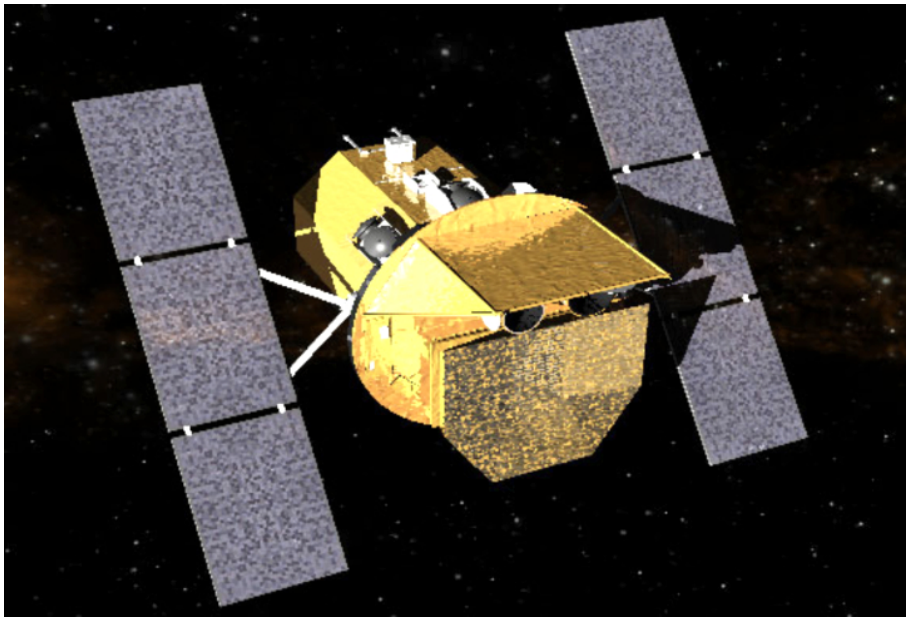

Figure 1.5: Artistic rendition of *Swift*. Credit: NASA

spectrum. The telescope has also been instrumental in identifying state-dependent correlations between X-ray and UV/optical emission, shedding light on the physical processes driving these variations.

The synergy between Swift and next-generation observatories, such as *XRISM*, *Athena*, and the Vera Rubin Observatory, will further enhance our understanding of the physics of BHXRBs and the broader context of accretion and jet formation in the universe.

1.8.3 The NuSTAR Telescope: An Overview

The *Nuclear Spectroscopic Telescope Array* (*NuSTAR*)[4] is a space-based X-ray observatory launched by NASA on June 13, 2012 (Figure 1.6). It is the first focusing high-energy X-ray telescope, capable of observing in the energy range of 3–79 keV with unprecedented sensitivity and angular resolution for that bandpass. This energy range bridges the gap between soft X-ray observatories, such as *Chandra* and *XMM-Newton*[5], and hard X-ray telescopes, such as INTEGRAL[6]. *NuSTAR* is particularly well-suited for studying BHXRBs due to its ability to probe both thermal and non-thermal emission components and in particular its capability to detect relativistic reflection features with high precision.

The observatory consists of two co-aligned telescopes equipped with multilayer-coated optics, which focus high-energy X-rays onto two focal plane modules (FPMA and FPMB). This innovative design of two focal planes, the multilayer optics and the extendable 10-meter boom allows *NuSTAR* to achieve an angular resolution of ~18 arcseconds (full-width half maximum, FWHM) and an energy resolution of 400 eV at 10 keV. The multilayer coatings enable efficient focusing of hard X-rays, making *NuSTAR* a groundbreaking instrument for high-energy astrophysics.

In the context of BHXRBs, *NuSTAR* has provided transformative insights into the physics of accretion and jet formation. One of its key strengths is its ability to perform detailed spectral modeling of the relativistic reflection features produced by X-rays reprocessed in the inner regions

[4] https://www.nustar.caltech.edu/
[5] https://www.cosmos.esa.int/web/xmm-newton
[6] https://www.cosmos.esa.int/web/integral

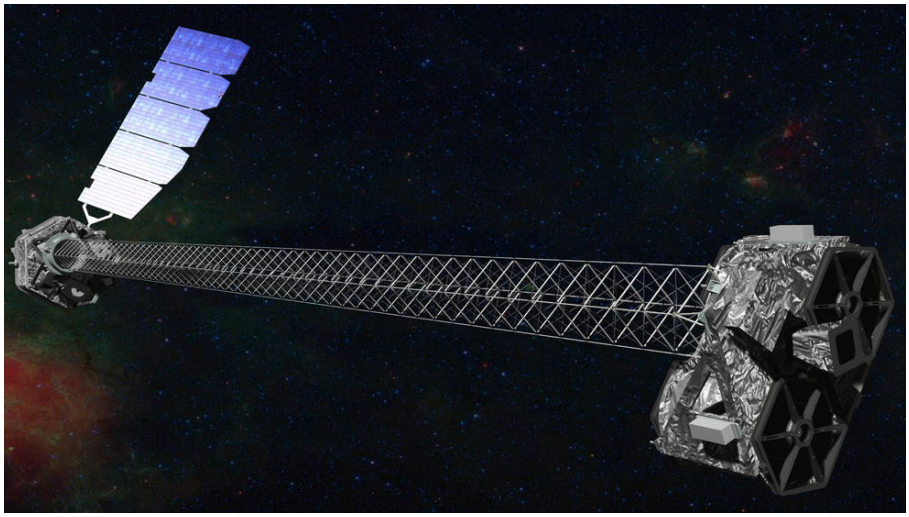

Figure 1.6: Artistic rendition of *NuSTAR*. Credit: NASA ID PIA15265

of the accretion disk. These features, including the broadened and skewed Fe Kα emission line and the Compton hump at 20–30 keV, offer direct probes of the geometry and dynamics of the accretion flow. The broad energy coverage of *NuSTAR* enables simultaneous constraints on both the soft thermal emission from the accretion disk and the hard non-thermal emission from the corona.

One of the primary techniques utilized with *NuSTAR* data is relativistic reflection modeling. This approach involves fitting the X-ray spectrum with models such as `relxill`, which incorporate the effects of Doppler shifts, gravitational redshifts, and relativistic light bending near the black hole. By fitting the shape of the Fe Kα line and the associated reflection continuum, it is possible to constrain the spin of the black hole, the inclination of the accretion disk, and the ionization state of the disk surface. *NuSTAR* has played a critical role in confirming high spin values for several stellar-mass BH (Draghis et al. 2020), providing evidence for efficient angular momentum transport during the accretion process.

Another key capability of *NuSTAR* is its ability to study the corona, the region of hot electrons responsible for upscattering disk photons via Inverse Compton (IC) scattering. The hard X-ray spectrum observed by *NuSTAR* provides constraints on the temperature and optical depth of the corona, as well as its geometry. For instance, observations have revealed correlations between the spectral cutoff energy (indicative of the coronal temperature) and the state of the source (Wang-Ji et al. 2018), offering insights into how the corona evolves during outbursts.

In addition to spectral studies, *NuSTAR* also provides crucial timing information. The observatory's high temporal resolution of $1\mu s$ in timing mode and $100\mu s$ in burst mode, enables the detection of QPOs in the hard X-ray band, which are thought to originate from relativistic effects in the innermost regions of the accretion flow. By studying QPOs across different energy bands, it is possible to investigate the coupling between the disk, corona, and jet, as well as the role of strong gravity in shaping the variability properties of the system.

NuSTAR has also made significant contributions (Koljonen et al. 2018b) to the study of jets in BHXRBs. Hard X-ray observations provide direct evidence of synchrotron or IC emission from relativistic particles in the jet, particularly during the hard state or state transitions. By combining *NuSTAR* data with observations at other wavelengths (e.g., radio, optical, and soft X-rays), it is possible to construct broadband SED and disentangle the contributions of the disk, corona, and jet (Porquet et al. 2024). This multi-wavelength approach has advanced our understanding of the jet-launching mechanism and the coupling between the jet and the accretion flow.

One of the unique advantages of *NuSTAR* is its ability to observe state transitions in BHXRBs with high sensitivity. During these transitions, the spectral and timing properties of the source evolve rapidly (days-to-weeks), providing a unique opportunity to study the interplay between different components of the accretion flow. *NuSTAR* observations have revealed dramatic changes in the reflection spectrum, coronal properties, and variability during these transitions, shedding light on the physical processes driving these changes.

In summary, *NuSTAR* has revolutionized the study of BHXRBs by enabling precise and detailed investigations of their high-energy emission. Its ability to probe the innermost regions of the accretion flow, constrain the properties of the corona, and study relativistic effects has provided critical insights into the physics of accretion and jet formation.

1.8.4 The Chandra X-ray Observatory

The *Chandra X-ray Observatory* (*Chandra*), launched on July 23, 1999, is one of NASA's Great Observatories and represents a significant advancement in X-ray astronomy (Figure 1.7). It provides exceptional angular resolution and sensitivity, making it a key instrument for studying high-energy astrophysical phenomena, including BHXRBs. With a sub-arcsecond angular resolution of $\sim$ 0.5 arcseconds, *Chandra* has enabled detailed imaging and spectroscopic studies of X-ray sources that were previously unattainable.

Chandra is equipped with a high-resolution mirror system based on grazing incidence reflection, allowing it to focus X-rays with unprecedented precision. The telescope includes two primary scientific instruments: the Advanced CCD Imaging Spectrometer (ACIS) and the High-Resolution Camera (HRC). ACIS provides imaging and moderate-resolution spectroscopy ($\sim$ 0.2 keV at 1 keV) in the energy range of 0.2–10 keV, while HETGS enables high-resolution spectroscopy, with energy resolution as fine as $\Delta E/E \sim 1000$, in the energy range of 0.4–10 keV.

In the context of BHXRBs, *Chandra* has been instrumental in investigating the structure and dynamics of accretion disks, the properties of relativistic jets, and the physics of high-energy radiation near compact objects. One of the key capabilities of *Chandra* is its ability to resolve spatially complex regions, such as crowded star fields, and to isolate the X-ray emission from a BHXRB, distinguishing it from surrounding sources like the nearby stellar companions.

Accretion Disk Studies with Chandra

The spectroscopic capabilities of *Chandra* have allowed for detailed investigations of the accretion disk properties in BHXRBs. The thermal component of the disk, typically modeled as a multi-temperature blackbody, is often observed in the soft X-ray band (0.3–2 keV). By fitting disk models such as `diskbb` or `kerrbb2` to the observed spectrum, it is possible to estimate key disk parameters, including the inner disk temperature ($T_{\rm in}$), the inner disk radius ($R_{\rm in}$), and the BH spin (Laycock et al. 2014; Liu et al. 2008). Additionally, *Chandra*'s high spectral resolution enables the study of emission and absorption features in the X-ray spectrum, such as the Fe Kα line at $\sim$ 6.4 keV, which is broadened and skewed by relativistic effects near the BH. For galactic sources, *Chandra* presents pile-up issues that affects BH spin measurements and reflection modeling.

Relativistic Reflection and Winds

Chandra's high-resolution grating spectra have been crucial for studying disk winds in BHXRBs. The Fe Kα emission line, often seen in the X-ray spectrum of these systems, provides a powerful probe of the inner accretion disk. Its shape and energy profile are affected by Doppler shifts, gravitational redshifts, and light bending caused by the strong gravitational field near the black hole.

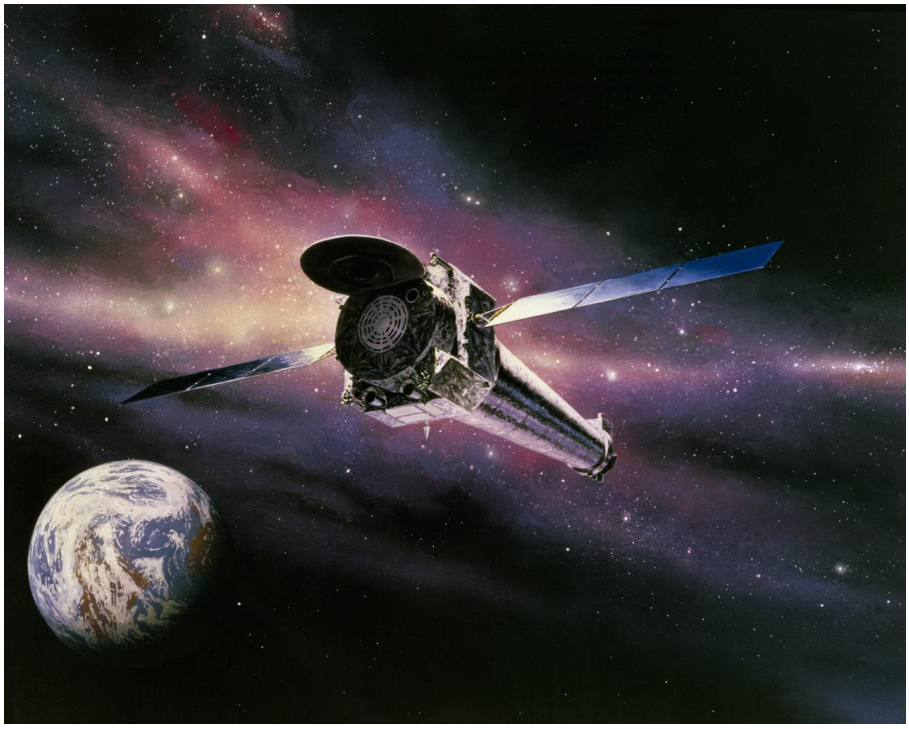

Figure 1.7: Artistic concept of *Chandra*. Credit: NASA ID 9501245

By modeling this line with relativistic reflection models such as `relxill`, *Chandra* observations have provided constraints on BH spin, disk inclination, and ionization (Miller et al. 2015).

Disk winds, another prominent feature of BHXRBs, manifest as absorption lines and edges in the X-ray spectrum, particularly in the soft X-ray band. With *Chandra*'s HETGS, it is possible to resolve these features and study the physical properties of the winds, including their ionization state, velocity, and geometry. Observations have revealed highly ionized winds with velocities ranging from hundreds to thousands of kilometers per second, offering insights into the mass-loss rates and feedback processes associated with accretion (Miller et al. 2016).

Jet and Corona Studies

The X-ray emission from BHXRBs also includes contributions from the corona, producing a power-law spectrum. *Chandra* has been used to study the spectral and temporal properties of the corona, providing constraints on its geometry and physical characteristics, such as temperature and optical depth. *Chandra* does not directly measure the coronal temperature (its energy range is too low). It constrains it indirectly via Fe K line broadening, reflection modeling, and reverberation lags (Tzanavaris & Yaqoob 2018; Gediman et al. 2024). Variability studies with *Chandra* have revealed QPOs (Huppenkothen et al. 2017) and other timing features that are linked to processes occurring in the corona or at the base of relativistic jets.

In the HS of BHXRBs, where jets are prominent, *Chandra* has been instrumental in resolving ballistic X-ray jets interacting with the interstellar medium (Espinasse et al. 2020). This emission is thought to arise from synchrotron or inverse Compton processes. By combining *Chandra* data with observations at other wavelengths, such as radio and infrared, it is possible to construct broadband SEDs and study the coupling between the jet and the accretion disk (Corbel et al. 2005).

Multi-Wavelength Campaigns

Chandra has been a critical component of multi-wavelength campaigns to study BHXRBs across the electromagnetic spectrum. These campaigns, which often include telescopes such as *NuSTAR*, *Swift*, and *NICER*, provide complementary data that enhance our understanding of the physical processes governing accretion and ejection. *Chandra*'s high-resolution X-ray spectra, combined with hard X-ray observations from *NuSTAR* or soft X-ray timing data from *NICER*, have led to breakthroughs in characterizing the interplay between the disk, corona, and jet in BHXRBs.

Contributions to Black Hole Spin Measurements

One of the most significant contributions of *Chandra* to BHXRB research is in the disk winds and wind/jet interplay (Neilsen & Lee 2009a). By modeling the relativistic reflection spectrum and the Fe Kα line, it is possible to infer the dimensionless spin parameter (a_*) of the BH. *Chandra*/HETG is exquisite at examining winds and so has been important for disentangling wind features from continuum / reflection (Miller et al. 2004).

Future Directions

As one of the most advanced X-ray telescopes currently in operation, *Chandra* continues to provide invaluable data for understanding the complex physical processes in BHXRBs. Future studies with *Chandra* will focus on detailed mapping of disk winds, and further extragalactic spin measurements via continuum fitting.

Chapter 2

Self-Consistent Analysis of MAXI J1813-095

Content of this Chapter

I present here the results of the analysis of seven observations of the MAXI J1813-095 black hole X-ray binary candidate using the *NICER*, *Swift*, *Chandra* and *NuSTAR* telescopes. These results have been published in *The Astrophysical Journal* (Ubach et al. 2024b). I was responsible for the complete data reduction, analysis, and writing of the article.

MAXI J1813-095 is a black hole X-ray binary that underwent a failed transition outburst in 2018. I studied 7 epochs using different instruments during its low luminosity outburst self-consistently.

2.1 Introduction

The BH candidate MAXI J1813-095 (hereafter MAXI J1813) was discovered on 2018 February 19 (Kawase et al. 2018) with *MAXI*/GSC. Follow up observations with the *Swift*/XRT localized the source to RA = $18^h13^m34.0^s$; DEC = -09°31′59.0″ (Kennea et al. 2018). GROND followup identified an optical counterpart (Rau 2018), and ATCA observations revealed a compact jet and classified the source as a likely radio-quiet BHXRB (Russell et al. 2018). From multi-wavelength observations, Armas Padilla et al. (2019) suggested that the companion star could be a G5V star at a distance of > 3 kpc. While the nature of the compact object in MAXI J1813 has not yet been dynamically confirmed, its characteristics are consistent with a BH primary and it is not known to have exhibited pulsations or thermonuclear X-ray bursts.

In this work, we study the geometry of the inner accretion flow of MAXI J1813 in its hard state via a self-consistent consideration of coronal Comptonization in reflection spectroscopy. As we demonstrate, its X-ray emission is consistent with being dominated by non-thermal coronal power-law emission and associated reflection features, as is typical of a BH transient in the hard state (e.g. Fuerst et al. 2018; Armas Padilla et al. 2019).

Figure 2.1 shows the 2018 MAXI lightcurve in X-rays of MAXI J1813 of the full outburst which lasted ~90 days. The stalled outburst as seen in 2018 for MAXI J1813, quickly reached the peak of X-ray flux within the first observations of its outburst. The observations with *NICER*, *Swift*, *NuSTAR* and *Chandra* are shown as solid vertical lines, corresponding to each observation. In the cases where the observations didn't overlap, multiple lines are drawn in Figure 2.1.

In this study, we analyze seven observations of MAXI J1813 with four different instruments. Five observations use *NICER*, all seven use *Swift*, three observations use *Chandra* and three

Table 2.1: Log of *NICER* (Ni), *Swift* (S), *Chandra* (Ch), and *NuSTAR* (Nu) observations of MAXI J1813-095.

Observations	Data Sets	Date (mm-dd-yyyy)	Obs. ID	Exposure times (ks)
Obs 1	Ni1+S1	02-21-2018	1200090101 & 00010563002	0.6 & 1
Obs 2	Ni2+S2	02-22-2018	1200090102 & 00811167000	0.4 & 0.25
Obs 3	Ni3+S3	02-23-2018	1200090103 & 00010563003	2.4 & 0.9
Obs 4	Ni4+S4	02-25/26-2018	1200090104 & 00010563004	1.1 & 0.4
Obs 5	Ni5+S5+Ch1+Nu1	02-27/28-2018	1200090105 & 00088654001 & 20264 & 80402303002	1.3 & 1.9 & 20 & 23.2
Obs 6	S6+Ch2+Nu2	03-06-2018	00088654002 & 20265 & 80402303004	1.8 & 19.9 & 20.5
Obs 7	S7+Ch3+Nu3	03-25-2018	00088654003 & 20266 & 80402303006	1.9 & 18.5 & 20.4

observations use *NuSTAR* (see Table 2.1). Hereafter, these will be referred to as Obs 1–7. We focus on a self-consistent reflection spectroscopic analysis of MAXI J1813's hard state in which we examine the system properties and consider the question of disk truncation.

X-ray reflection in XRBs involves the reprocessing of high-energy X-rays produced in the corona at the accretion disk surface, leading to the characteristic signatures (e.g., Fe-Kα fluorescence) which can be observationally constrained. Jiang et al. (2022) studied MAXI J1813 using the last 3 observations in our analysis including data from *Swift* and *NuSTAR*. They fit the data using a variety of relativistic disk reflection and the Comptonization models. The three reflection models included an earlier version of `relxillCp` which keeps the electron temperature fixed at 300 keV. The other two reflection models used in their analysis are `relxilllpcp` (Dauser et al. 2016) and `reflionx` (Ross & Fabian 2005). They analyzed each of the three observations with all three models, using `nthcomp` for the Comptonization of the disk (Życki et al. 1999) and `TBnew` to account for Galactic absorption (Wilms et al. 2000). A continuum-only joint analysis to assess the prominence of reflection features, showed a clear Fe-K emission line at ~6.5 keV and a Compton hump at ~20 keV with a stable Γ ~1.6-1.7. From the reflection analysis, The iron abundances were near solar, and the ionization was high (~3). The best joint fit was obtained using `relxilllpcp`. From this, the reflection fraction was found to be low, ~0.18; notably this value was significantly lower, ~ 0.08 in the fit with `relxillCp`, owing to those models respective geometric assumptions regarding the corona.

Jana et al. (2021b) studied MAXI J1813 using *NICER*, *NuSTAR* and *Swift* data but using less data than we consider in our analysis. Jana et al. (2021b) performed a timing analysis with the *NICER* data finding no quasi-periodic oscillations (QPOs). Their spectral analysis was performed using a disk blackbody component and a power-law model to extract the thermal and non-thermal fluxes, and to find the photon index and inner disk temperature. They included Galactic absorption (`TBabs` (Wilms et al. 2000)) and a gaussian to fit the Fe-K, with a full model `TBabs(diskbb + power-law + gaussian)`. Another model they explored was the `reflect` model in order to determine the reflection fraction, photon index and inclination. Lastly, they used a physical two-component advective flow (TCAF) model to estimate the mass of the black hole and a `laor` component to model the Fe-Kα reflection line. The estimated black hole mass was found to be $\sim 7.4 M_{\odot}$.

In Section 2.2, we describe the observations and data reductions. In Section 2.3, we present the data and our analysis utilizing a self-consistent spectral reflection model. In Section 2.4 we discuss our results across the different observations. In Section 2.5, we present our conclusions.

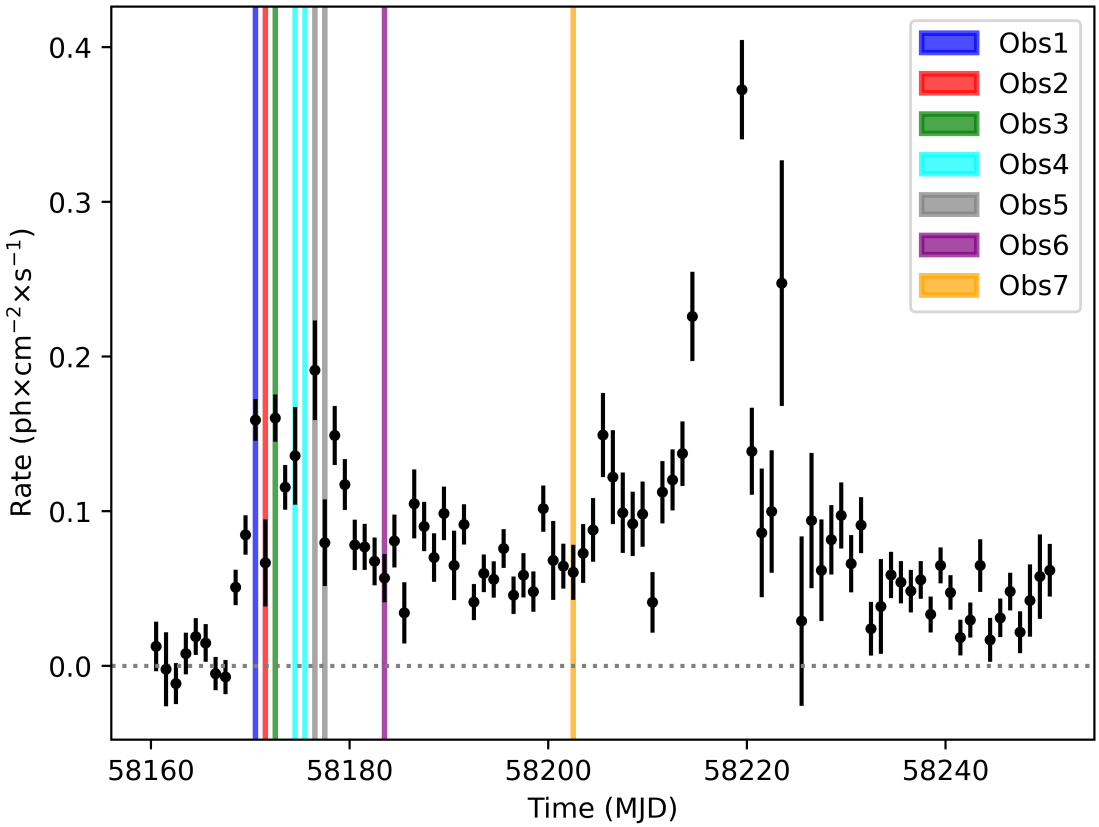

Figure 2.1: The lightcurve of MAXI J1813 from the MAXI telescope during the stalled outburst from 2 to 20 keV. MAXI J1813 reaches its peak of luminosity quickly. The vertical solid lines, correspond to each observation (see Table 2.1). Observations 4 and 5 were not taken strictly simultaneously by each observatory, but were within 1 day. We therefore mark them as two separate lines in each case.

2.2 Data Selection and Reduction

We used data from four different instruments. We aggregate observations within ∼24 hours of one another among these instruments to maximize coverage of the source. We took data from 21-02-2018 to 25-03-2018 (see Table2.1) where *Swift* is present in all observations overlapping with *NICER* in Obs 1–5 and with *Chandra* and *NuSTAR* in Obs 5–7. *NICER* and *Swift* energy ranges were chosen in such a way as to ensure that the data were uniformly above the background. Although we have aggregated the observations, in some cases there may be more than one distinct good-time-interval (GTIs) for a given instrument's observation. In such instances, those GTIs are treated as distinct spectra.

2.2.1 *NICER*

NICER observations were first screened using the default settings in NICERDAS v8, i.e., requiring distance from the Earth limb > 15 deg, distance from the *bright* Earth limb > 30 deg. Data from the South-Atlantic Anomaly are excluded, as well as any data within 60° of the Sun unless the "sunshine" flag is equal to 0. Individual focal-plane modules (FPMs) were screened to remove any outlier on the basis of undershoot, overshoot, or X-ray event rates with a $\sim 10\sigma$ threshold of variance with respect to the detector ensemble for rejection. Detectors 14, 34, and 54 were excluded from analysis owing to potential calibration issues with these detectors. The resulting data products were screened for edge-clipping particle events using the standard "trumpet filter" on the "PI ratio" (i.e., the ratio of slow-chain to fast-chain event energies), and the 3C50 background model was employed for spectral analysis (Remillard et al. 2022). Response products have been generated using calibration release xti20210707[1].

2.2.2 *Swift*

Swift observed MAXI J1813 at three epochs simultaneously with *NuSTAR* and *Chandra*, and five epochs with *NICER* over a total of seven observations. In total, *Swift* observed MAXI J1813 twelve times between 2018 February 20 and 2018 March 25, of which we only used those coinciding with observations including other instruments. *Swift*/XRT observations of MAXI J1813 were carried out in windowed-timing (WT) mode. We extracted cleaned event files with the FTOOLS task xrtpipeline version 0.13.7 and calibration (CALDB) file version 20210915. We chose a box region of radius 95"×90" for source and 180"×90" for the background. Light curves, source, and background spectra were extracted using XSELECT version 2.5a.

2.2.3 *NuSTAR*

We reduced the *NuSTAR* data using the *NuSTAR* Data Analysis Software (NuSTARDAS) package and calibration data of v20210824. MAXI J1813 spectra were extracted for both FPMA and FPMB detectors from a 100" radius circle centered on the source, while the background spectra were extracted from a source-free circle of 200" on the same detector chip. Data are analyzed from 3-75 keV for each FPM.

2.2.4 *Chandra*

We make use of *Chandra*'s Advanced CCD Imaging Spectrometer (ACIS) instrument. Owing to a contamination layer on the filter, ACIS observations have reduced sensitivity below $\sim 1-2$ keV.

[1] We have confirmed that differences are negligible within statistical uncertainty using the most recent calibration release (20221001).

Chandra observed MAXI J1813 during three epochs coinciding with *Swift* and *NuSTAR* (Obs 5–7), with *NICER* data available as well for Obs 5. The observations were performed with the ACIS in continuous-clocking (CC) mode. No gratings were employed. The X-ray data analysis was performed using the *Chandra* Interactive Analysis of Observation (CIAO) software 4.14.1 (Fruscione et al. 2006), with CALDB version 4.9.8.

We used a box of 20"×20" for source extraction, and computed responses with point-spread function corrections (see Appendix 2.A and 2.B for more details on the *Chandra* extractions and analyses). For background extraction, we used a source-free box of 20"×100". Data were analyzed from 1.4-10 keV.

2.3 Analysis & Results

Spectral analysis was carried out using XSPEC 12.13.0c (Arnaud 1996). The principal aim of our spectral analysis is to leverage the broadband X-ray data to examine the accretion geometry (and determine associated parameters of the BH system) throughout the stalled outburst. *Chandra* data are considered separately in Appendix 2.A owing to complications related to photon pileup in the data. Briefly, our adopted self-consistent physical model is incompatible with the use of the *pileup* model that is needed to correct *Chandra* spectral distortion. Unless specified otherwise, all uncertainties are presented at 90% confidence throughout.

2.3.1 Preliminary Continuum Analysis

As a first step, we fit the spectral continuum to characterize the data and search for the presence of reflection signatures like Fe-Kα emission, as identified in MAXI J1813 in other works like Jiang et al. (2022) and Jana et al. (2021b). We use *nthcomp* to model a Comptonization continuum spectrum (Życki et al. 1999), with neutral gas absorption modeled by *TBabs* (Wilms et al. 2000). A representative fit and data-to-model ratio for Obs 5 are shown in Figure 2.3. The residuals show broadened Fe-K fluorescence, indicative of relativistic reflection in the data. Our continuum analysis of all 7 observations produces results consistent with MAXI J1813 having remained in the canonical hard state for the duration of its outburst. The Compton power-law dominates the spectrum and exhibits a photon index Γ=1.6–1.8, typical of a hard state.

2.3.2 Self-Consistent Spectral Model

We next formulate a self-consistent spectral model which describes the Comptonization of seed thermal disk photons, and a reflection component associated with the illumination of the disk's surface by back-scattered Compton photons. Our model is constructed to require that *all* photons emerging from the disk's surface are Comptonized by the same corona, and so we impose the same Comptonization kernel on both direct disk emission and reflection emission components. Compared to models which neglect the role of Compton-scattering on the reflection emission, this self-consistent formalism generally increases the reflection fraction. The disk thermal component is modeled using the multicolor blackbody model `diskbb` (Makishima et al. 1986). This is defined by two parameters, a characteristic temperature kT, and a normalization. To model Comptonization, we use the convolution model `simplcut` which can be supplied with an arbitrary seed spectrum (in this case, the disk emission) (Steiner et al. 2009; Steiner et al. 2017; Steiner et al. 2017). Its key parameters are a photon index Γ, a scattering fraction f_{sc} (i.e., the proportion of seed photons which are Comptonized by the corona), electron temperature kT_e, and the reflection fraction R_f which describes the apportionment of Compton-scattered photons which illuminate the disk. Reflection is described using `relxillCp` version 2.1, from the `relxill` model library

(Dauser et al. 2013; García & Kallman 2010). We employed `simplcut` in order to be able to also Comptonize the reflection component. Simplcut, Γ, kT_e and R_f parameters are matched in the two models, and both use `nthcomp` for the kernel, but `simplcut` is capable of working with an arbitrary seed spectral shape (here both thermal and the reflection emission). Moreover, by using simplcut in this way, we properly account for the fraction of coronal photons which hit the disk versus those which reach the observer; otherwise those two quantities aren't properly coupled. The radial reflection emissivity profile is defined by power-law indices q_1 and q_2 with a break radius between them; here we have simply set $q_1 = q_2 = 3$. The innermost disk radius R_{in}, BH spin a_*, and inclination i together define the disk and spacetime geometry. We fix the spin to its maximum allowed value, $a_* = 0.998$, and fit for R_{in} and i. The strength of Fe-K fluorescence and the Compton hump is modulated by the iron abundance, Z_{Fe}, which is a free parameter when fitting with *NuSTAR*. The disk's surface is approximated as a uniform slab of density n with ionization parameter ξ.

The reflection component described by *relxillCp* is produced when Compton disk emission scatters in the corona, and a fraction of those scattered, energized photons return to illuminate the surface of the disk. The emission seeding the coronal Compton signal is a combination of thermal emission produced by disk viscosity / reflection thermalization and reflection reprocessing at the surface of the disk. The present formulation of *relxill* and its variants do not allow for an arbitrary seed spectrum and instead is set by a power-law spectral illumination extending down to ~ 0.1 keV. Unfortunately, for disk spectra of interest for BHXRBs, this power-law approximation is problematic at low energies, especially those below the disk's characteristic temperature, as we illustrate in Figure 2.2, viz. compare the blue and green curves. Given that `simplcut` scatters photons between energies, it is important that the reflection continuum shape does not behave unphysically out of the fitted bandpass, otherwise that unphysical behavior could alter the scattered signal over the observed bandpass. To correct for this unphysical runaway, we apply an empirical correction by defining a multiplicative factor that is unity at high energies but falls off as a power-law at low energies. This multiplicative broken power-law (`mbknpo`) has two terms: the break energy, which has been fixed to $b = kT_{disk} \times 4.5$ from empirical exploration of Comptonization models, and the spectral index below the break which has a fixed relationship to the Compton power-law photon index: $I = \Gamma - 1.5$ (see Svoboda et al. 2024; Steiner et al. 2024). It's functionality is illustrated in the blue curve of Fig. 2.2.

Put together, our physical model is formulated as: `TBabs×(simplcut(diskbb + mbknpo×relxillCp))`. As a final addition, in order to account for cross-calibration differences between missions, which is often of order $\gtrsim 10\%$ in absolute flux, we include a flux standardization model `crabcorr` (Steiner et al. 2010). This multiplicative model was designed to standardize flux measurements of the Crab (or other calibration targets) between instruments. But where such measurements are variable in time, uncertain, or unavailable, its two parameters (a cross-normalization constant and a difference in spectral index, $\Delta\Gamma$) can also be fitted directly. In fullness, our spectral model becomes:

`crabcorr×TBabs×(simplcut(diskbb + mbknpo×relxillCp))`.

2.3.3 Fitting Results

We define a logarithmic energy grid from 10 eV to 500 keV in 500 intervals for computing the model, and apply this model to Obs 1–7. For Obs 1–5 which include *NICER* data, we adopt XSPEC's *pg*-statistic for fitting, which assumes Poisson-statistics for the data and Gaussian-statistics for the background uncertainty, as appropriate for *NICER* given use of the 3C50 background model. For Obs 6 & 7, we instead use a χ^2 fit statistic since these observations have no NICER data, and Gaussian statistics better capture the systematics present in the *Swift Chandra*

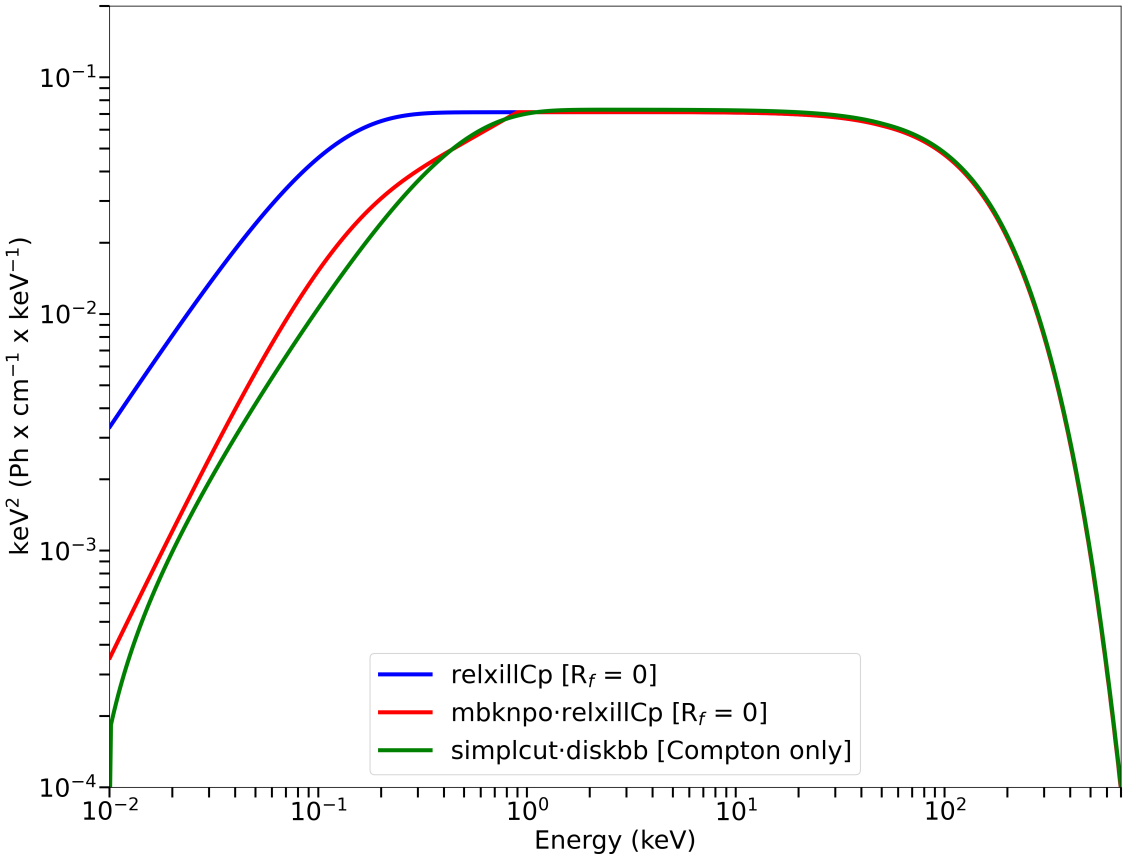

Figure 2.2: An illustration of the runaway flux problem when applying current reflection models to BHXRBs. The blue line shows the power-law spectrum adopted by *relxillCp* which illuminates the disk. The green line shows the desired ("true") spectrum corresponding to Compton-scattered emission from a 0.2 keV *diskbb* component. The red line shows our adopted multiplicative correction applied to the blue curve. This correction curtails the unphysical runaway at low energies and provides a reasonable approximation to the Comptonization spectrum.

Table 2.2: The observed flux of MAXI J1813. The X-ray luminosity is computed from the unabsorbed 0.7- 10 keV flux, adopting a distance of 8 kpc and assuming a BH mass of 10 solar masses in computing the Eddington luminosity.

Observations	$\mathrm{Flux}_{0.7-10\,(\mathrm{keV})}$ ($10^{-10}\mathrm{erg\cdot cm^{-2}\cdot s^{-1}}$)	L_x/L_{Edd} (unabs.)
Obs 1	8.6±0.1	0.008
Obs 2	8.8±0.2	0.008
Obs 3	8.1±0.2	0.007
Obs 4	6.6±0.1	0.006
Obs 5	6.2±0.2	0.004
Obs 6	5.2±0.1	0.005
Obs 7	5.8±0.1	0.004

NuSTAR data. We note that this choice of statistic has insignificant impact on the best-fitting parameter values in the resulting fit. We fix the neutral hydrogen column to $N_{\mathrm{H}} = 1.35 \times 10^{22}$ cm^{-2} based on our preliminary fits presented in Section 2.3.1. For Obs 1–4 which have no *NuSTAR* high-energy data, we fix $kT_e = 100$ keV and adopt a fixed iron abundance of $Z_{\mathrm{Fe}} = 3$ based on fits to Obs 5–7.

We analyze data in the 0.7-10 keV energy range with *NICER* and *Swift*, an energy range of 3-75 keV with *NuSTAR*. In Table 2.2, we present the flux for each observation and the corresponding X-ray luminosity, assuming a fiducial distance of 8 kpc and mass of 10 $M_{\odot}$.

Our full fitting results to Obs 1–7 are presented in Table 2.3. We remark that, operationally, the reflection fraction $\mathrm{R_f}$ is determined iteratively self-consistently by matching the disk illumination assumed by *relxillCp* to that produced by *simplcut* (see Steiner et al. 2016 2017). In this way, the self-consistent R_f is determined iteratively from the fit, parameterizing the relative strength of reflection flux observed compared to the coronal continuum flux observed (i.e., sometimes alternatvely termed as "reflection strength"). As shown in Table 2.3, the thermal component is consistent with a disk black-body emission of $kT_{in} \sim$ 100-300 eV along the observations, which is consistent with the values given by Armas Padilla et al. (2019) and Jana et al. (2021b) from joint *NuSTAR* and *Swift* observations corresponding to Obs. 5–7. According to these results, we conclude that any thermal emission must be cool and weak, as is typical for the hard state.

Our best-fitting results using `relxillCp` suggest a thin disk with an inner radius of $R_{\mathrm{in}} = 2.1 + /-1.3 R_{\mathrm{g}}$ around the BH (90% confidence). This value describes the weighted mean of the results in Table 2.3, a result which is strongly anchored in the high-precision fit obtained for Obs 5. Obs 5 is unique in having very high signal-to-noise across the full bandpass, as it is notably the *only* observation which includes both *NICER* and *NuSTAR* data. Because of the comparatively weaker constraining power of the other observations, we cannot rule out the possibility that Obs 5 alone has the inner-edge close in compared to the other observations, but we feel the most likely interpretation is that the disk inner-radius is stable and small throughout, and the fits are simply less constraining on R_{in}. Adopting this picture, the low weighted-mean of R_{in} suggests that either the BH is very highly spinning and very slightly truncated, or that the disk extends to the ISCO and the BH spin is $a_* \gtrsim 0.7$. We find the inclination at values of i = 14-47° throughout the observations with values in the last three observations closely matched by Jiang et al. (2022). We find that the inclination values are consistent with a constant value of $\sim 28° \pm 10°$ (90%), from the weighted mean. All the fits show a moderate-to-high ionization ($log\ \xi \sim 2 - 3.2$), with density ($n_e \sim 10^{16-19}\mathrm{cm^{-3}}$).

Figure 2.4 presents spectral fits for two representative observations (Obs 1 and Obs 5) for our campaign in the topmost panels. The bottom series of panels depict data-to-model ratios, all

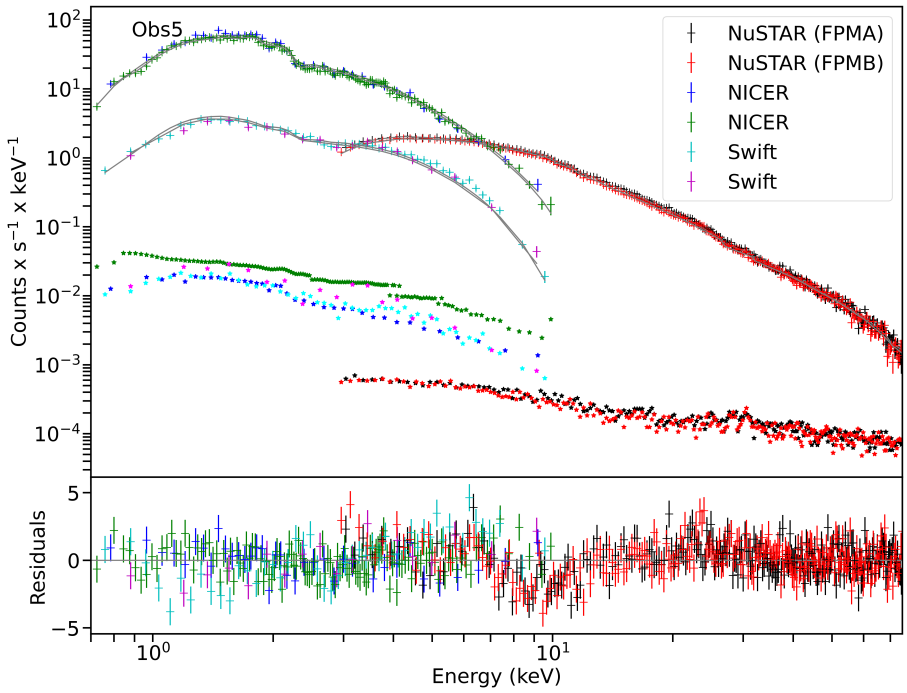

Figure 2.3: The spectrum for Obs 5. Top: *NICER* (blue and green), *Swift* (purple and cyan: XRT) and *NuSTAR* (black: FPMA; red: FPMB) source and associated background spectra (as stars) of MAXI J1813 for a continuum fit of `TBabs` × `nthcomp`. Bottom: Associated data-to-model ratio plot. The residuals – *NuSTAR* in particular – show a broad peak around 6.5 keV corresponding to Fe-K fluorescence, an indicator of spectral reflection. We applied a rebinning on *NICER* and *Swift* in order to make the Fe-K line more visible with *NuSTAR* showing a broad small peak. Two GTIs apiece for each of *Swift* and *NuSTAR* are included in Observation 5. We fit for spectral differences between GTIs to account for potential variation.

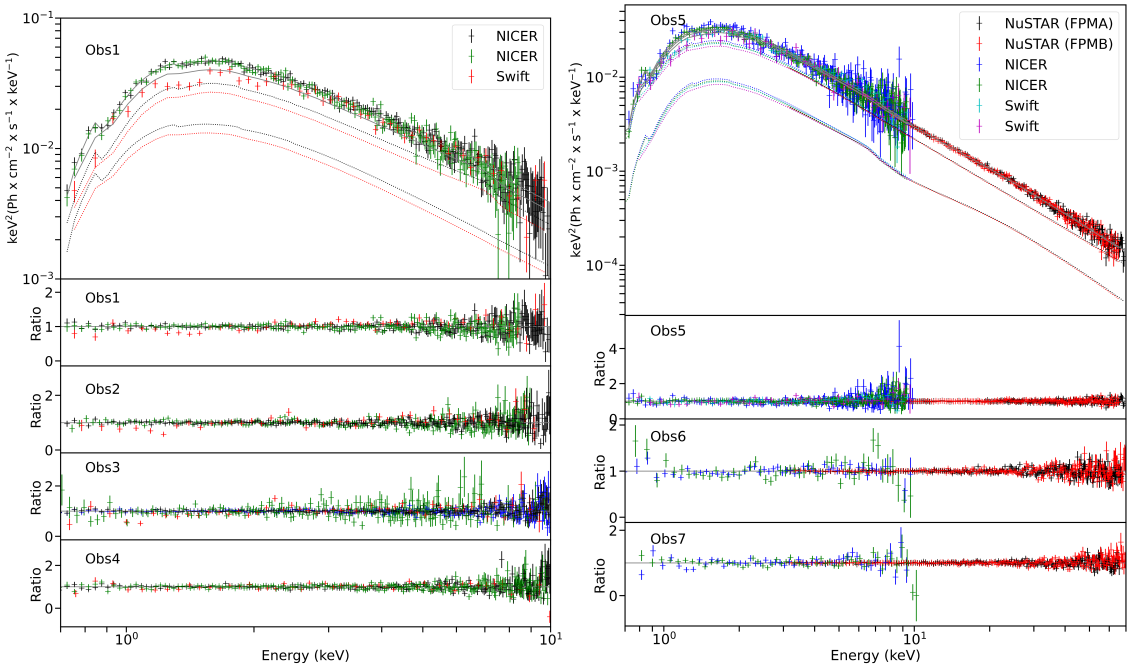

Figure 2.4: Top panels show the Obs 1 and Obs 5 unfolded spectra and the lower panels are the ratio plots of each observation with the best fit. Both **spectra** show the continuum and the reflection model. The two *NICER* GTIs shown with the best S/N ratio. For *Swift* we used only GTI due to only one was created for the left panel and two for the right panel.

tightly clustered around unity without obvious residual features. These illustrate the quality of our fits.

Subsequent to optimizing our spectral fits, we determine the uncertainties using Markov-Chain Monte Carlo (MCMC). The XSPEC MCMC implementation is based on the work of Foreman-Mackey et al. (2013), who devised a affine-invariant sampler (Goodman & Weare 2010) consisting of a number of "walkers" which navigate and map out the posterior parameter space in proportion to its probability. Our MCMC runs consist of 54 walkers, with an initial chain length of 100000. After burning in using three iterations, we perform 10–50 million chain-length runs, having extended as needed to reach convergence which is essential for obtaining accurate estimates of parameters and credible intervals from MCMC simulations. The posterior uncertainties given in Table 2.3 come from this MCMC analysis, and we note that the ranges presented are consistent with results from using the "error" command in XSPEC. Figure 2.5 shows contour plots for Obs 1 and Obs 5, presenting pair-wise correlations between all combinations of $R_{\rm in}$, $log\xi$, $Z_{\odot}$, $kT_{\rm e}$ and i. On the diagonal, a histogram of each parameter can be seen. Notably, while $R_{\rm in}$ is only weakly constrained to be $\lesssim$ 80 $R_{\rm g}$ for Obs 1, in the case of Obs 5, $R_{\rm in}$ is very precisely constrained to $\approx 2.0 \pm 0.5 R_g$ (1σ). We illustrate the performance of our MCMC runs in Figure 2.6, which depicts the autocorrelation of $R_{\rm in}$ and i for Obs 5. As is shown here, we have run our chains to at least $\gtrsim$ 10 times the typical autocorrelation length of a walker for the slowest-converging parameter in order to obtain good sampling of the posterior distribution. The MCMC results again confirm the key constraining power of observation 5, owing to the strong synergy between *NICER* and *NuSTAR* in particular.

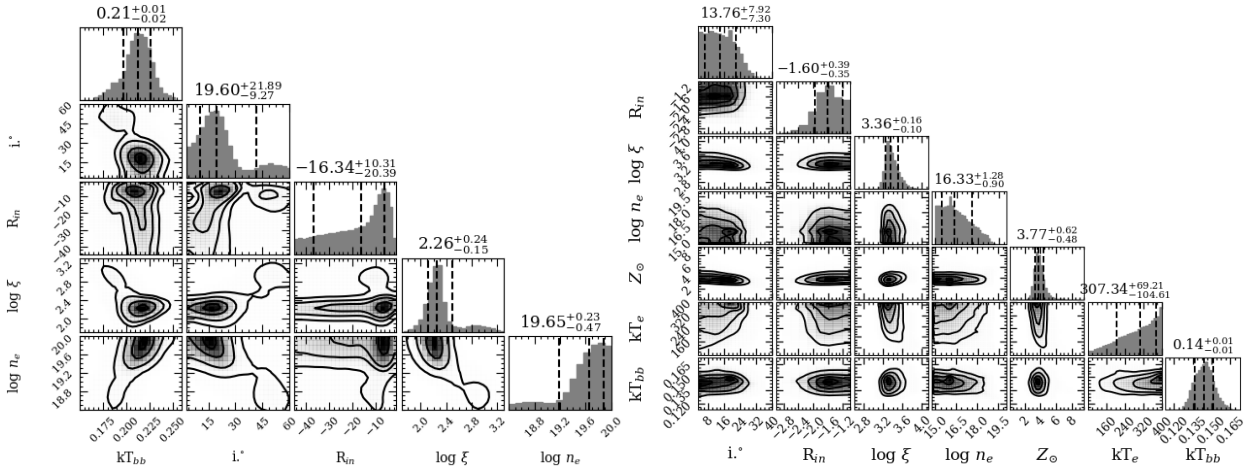

Figure 2.5: Corner plots show MCMC posterior distributions of parameters of interest for Obs 3 (left) and Obs 5 (right). We emphasize on the inner radius parameter showing a better constrain in Obs 5 although in both cases the 1σ contour is showing a sligthly truncated or non-truncation of the disk. In both cases the disk is moderate to high ionized and dense.

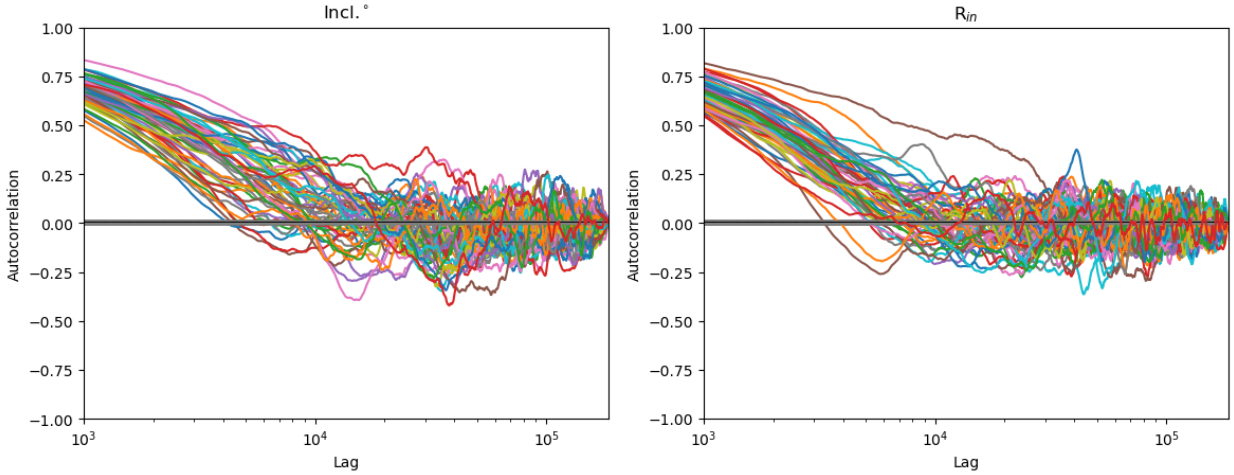

Figure 2.6: Autocorrelation lags for Obs 5 MCMC walkers for i and $R_{\rm in}$. Each colored line shows the behavior of an individual walker. As shown here, the chains have been run to well over 10 times the characteristic autocorrelation length. This is important to ensure the converged chains obtain representative samples of the posterior parameter space with a useful effective sample size. Note how this measure can differ somewhat between different parameters.

Table 2.3: Best-fitting model parameters for Obs 1–7. The quoted errors are at the 90% confidence level based upon MCMC posteriors with uniform priors. For the purposes of fitting over the maximum allowed parameter space, the BH spin has been fixed at $a_* = 0.998$ with a free inner radius and N_H fixed at 1.35×10^{22} cm^{-2} observations.

Parameters	Obs 1	Obs 2	Obs 3	Obs 4	Obs 5	Obs 6	Obs 7
Γ	$1.69^{+0.04}_{-0.09}$	$1.68^{+0.03}_{-0.14}$	$1.65^{+0.03}_{-0.02}$	$1.68^{+0.02}_{-0.03}$	$1.61^{+0.01}_{-0.01}$	$1.67^{+0.02}_{-0.02}$	$1.79^{+0.05}_{-0.04}$
$f_{\rm sc}$	$0.40^{+0.13}_{-0.24}$	$0.39^{+0.13}_{-0.22}$	$0.46^{+0.07}_{-0.11}$	$0.34^{+0.12}_{-0.13}$	$0.28^{+0.06}_{-0.06}$	$0.41^{+0.25}_{-0.17}$	$0.75^{+0.08}_{-0.21}$
R_f*	$0.97^{+0.19}_{-0.25}$	$0.75^{+0.26}_{-0.17}$	$0.86^{+0.21}_{-0.06}$	$0.67^{+0.1}_{-0.34}$	$0.80^{+0.14}_{-0.02}$	$0.76^{+0.13}_{-0.15}$	$0.95^{+0.13}_{-0.11}$
$kT_{\rm disk}$ (keV)	$0.18^{+0.03}_{-0.03}$	$0.18^{+0.36}_{-0.06}$	$0.21^{+0.02}_{-0.03}$	$0.16^{+0.06}_{-0.04}$	$0.14^{+0.01}_{-0.01}$	$0.12^{+0.05}_{-0.02}$	$0.12^{+0.07}_{-0.02}$
Norm$_{\rm disk}$	$(33^{+40}_{-20})\times10^3$	$(15^{+80}_{-10})\times10^3$	$(15^{+10}_{-10})\times10^3$	$(42^{+20}_{40})\times10^3$	$(100^{+70}_{-40})\times10^3$	$(16^{+20}_{-20})\times10^4$	$(36^{+210}_{-30})\times10^3$
Incl. (°)	47^{+30}_{-40}	43^{+20}_{-10}	20^{+40}_{-10}	37^{+30}_{-20}	14^{+10}_{-10}	40^{+10}_{-10}	23^{+10}_{-10}
R$_{in}$ (R$_g$)	34^{+77}_{-31}	16^{+13}_{-13}	20^{+36}_{-14}	15^{+14}_{-13}	$2.0^{+0.8}_{-0.7}$	10^{+46}_{-9}	12^{+36}_{-6}
log ξ(erg cm s^{-1})	$3.18^{+0.62}_{-1.20}$	$2.81^{+0.66}_{-0.39}$	$2.26^{+0.73}_{-0.26}$	$2.46^{+0.73}_{-0.61}$	$3.36^{+0.28}_{-0.16}$	$1.87^{+0.66}_{-0.34}$	$2.75^{+0.11}_{-0.97}$
Z$_{\rm Fe}$(Z$_\odot$)**	3	3	3	3	$3.8^{+1.2}_{-0.8}$	$2.9^{+2.8}_{-1.7}$	$1.1^{+1.1}_{-0.3}$
logn_e(cm^{-3})	$17.6^{+1.7}_{-2.4}$	$18.7^{+1.1}_{-2.6}$	$19.6^{+0.3}_{-1.2}$	$18.6^{+1.3}_{-2.6}$	$16.3^{+2.0}_{-1.2}$	$16.1^{+2.3}_{-0.9}$	$16.1^{+1.3}_{-1}$
kT_e(keV)***	100	100	100	100	307^{+90}_{-170}	249^{+140}_{-170}	294^{+100}_{-180}
Norm$_{\rm Refl}$	$(2.9^{+2.9}_{-1.6})\times10^{-3}$	$(4.3^{+3.6}_{-1.4})\times10^{-3}$	$(1.4^{+1.1}_{-0.5})\times10^{-2}$	$(2.3^{+1.8}_{-0.9})\times10^{-3}$	$(2.3^{+0.9}_{-0.9})\times10^{-3}$	$(1.8^{+1.1}_{-0.5})\times10^{-3}$	$(2.4^{+0.8}_{-0.8})\times10^{-3}$
cross-norm (XRT)	$0.86^{+0.02}_{-0.02}$	$0.94^{+0.03}_{-0.03}$	$0.86^{+0.03}_{-0.02}$	$1.07^{+0.03}_{-0.03}$	$0.98^{+0.03}_{-0.03}$	$0.96^{+0.02}_{-0.02}$	$0.93^{+0.03}_{-0.02}$
$\Delta\Gamma$ (XRT)	0	0	0	0	0	0	0
cross-norm. (FPMA)	-	-	-	-	1	1	1
$\Delta\Gamma$ (FPMA)	-	-	-	-	0	0	0
cross-norm. (FPMB)	-	-	-	-	$1.01^{+0.02}_{-0.02}$	$1.00^{+0.02}_{-0.02}$	$0.99^{+0.02}_{-0.01}$
$\Delta\Gamma$ (FPMB)	-	-	-	-	$(1.0^{+0.7}_{-0.7})\times10^{-2}$	$(1.6^{+0.7}_{-0.7})\times10^{-2}$	$(6.4^{+7.5}_{-7.1})\times10^{-3}$
cross-norm. (NICER)	1	1	1	1	$1.10^{+0.03}_{-0.03}$	-	-
$\Delta\Gamma$ (NICER)	0	0	0	0	$(6.1^{+2.2}_{-2.3})\times10^{-2}$	-	-
χ^2/ν	(PG-stat)528/461	(PG-stat)509/464	(PG-stat)760/657	(PG-stat)720/705	(PG-stat)1056/928	585/522	570/536

* Reflection fraction values are determined iteratively by matching illuminating and scattered components self consistently. The errors bars have been assessed by repeating this process for random samples from the chain.
** The iron abundance is sensitive to the Compton hump strength and so has been fixed at 3 for Obs 1–4 without *NuSTAR* data based upon a round average from the fits to Obs 5–7.
*** The electron temperature is fixed to a round 100 keV for Obs 1–4 owing to a lack of high-energy spectral coverage in the absence of *NuSTAR* coverage.

2.4 Discussion

We obtain the reflection fraction iteratively, by comparing the incident coronal emission which is assumed by *relxillCp* to reach the disk (operationally, obtained with a *relxillCp*) component omitted from the fit for which R_f is set to 0, and then scaled by $((1+R_f)\times R_f^{-1})$ with the Compton component being output from *simplcut* (Section 2.3.2), and adjusting them to match. The primary change from refitting while iteratively adjusting R_f was on $f_{\rm sc}$. We required the incident and output Compton components to match within 5% in each fit.

Our previous investigation, Jiang et al. (2022), revealed evidence of reflected emission from the inner region of the disk. Here, in this follow-up work in which we impose a self-consistent modeling framework, we reach similar conclusions about several properties of the system, e.g., $R_{\rm in}$ and i. However, a crucial difference between our work and the analyses of Jiang et al. (2022) and Jana et al. (2021b) is we find a much larger R_f, very close to unity. This difference is because here we account for the fact that a proportion of the disk reflection emission also scatters in the corona, resulting in a hardened continuum component which is mingled with the continuum produced by Compton-scattered thermal-disk emission. Consequently, when including this effect, the reflection fraction is several-fold larger than when this consideration is omitted. Moreover, this larger reflection fraction, of order unity, is consistent with most static coronal geometries (see, e.g., Dauser et al. 2016). The identifiable Fe-Kα feature is associated with the transmitted portion of reflection emission passing through the corona. Other aspects of Jiang et al. (2022) are consistent with our analysis, including the disk ionization and the temperature of the cool disk emission. In contrast, Jana et al. (2021b) fitted a significantly hotter thermal component. Jana et al. (2021b) also fit the inner radius via the *laor* model obtaining an inner radius of $\sim 2.6 R_g$ quite similar to our constraint.

Our self-consistent disk reflection analysis with the `relxillcp` model, showed similarities with previous studies in the same epoch. The most important similarity is consistently small inner radius found in all three studies (all finding $R_{\rm in} < 7 R_{\rm g}$) which rules against large-scale truncation for MAXI J1813's hard state peak. This is despite a putative low Eddington luminosity, for a nominal mass of $10 M_{\odot}$ and a fiducial distance of 8 kpc. This finding is noteworthy in that a topic of high interest over recent years in BHXRBs has been whether or not accretion disks are truncated at many tens or hundreds of R_g in hard states. In particular there are disagreements between results based on timing data (e.g., Wang et al. 2021; De Marco et al. 2021), versus those determined using reflection spectroscopy (e.g., Jiang et al. 2019; García et al. 2019). Other spectral results have also generally favored interpretations in which at sufficiently high luminosities (above a few percent of $L_{\rm Edd}$), the disk is at the ISCO or else only slightly truncated (e.g. Reis et al. 2010; Plant et al. 2015).

The parameters of the reflection model across the 7 observations are heterogeneous in precision, but with consistent values. In particular, they are consistent with a single inner-disk / coronal geometry across the month-long span of the observations. The coronal temperature can only be constrained using high-energy *NuSTAR* data, and is consistently $\rm kT_e > 100$ keV for Obs 5–7, for which *NuSTAR* data is available. R_f is consistent and near unity, ranging between ~0.7–1.0. The data support a moderately-high density, $n_{\rm e} \approx 10^{16} - 10^{19} {\rm cm}^{-3}$, and a high metallicity, with $Z \approx 3 Z_{\odot}$. As mentioned in Section 2.3.3, the strongest constraints are achieved from Obs 5, which is the only observation featuring broadband coverage with both *NuSTAR* and *NICER*, i.e., the two highest throughput facilities in their respective bandpasses. Because this constraint is so dominant over our net results, we have also investigated our joint constraints when omitting Obs 5. Without observation 5, in which we joint *NuSTAR*, *NICER* and *Swift*, the inner radius increases, at 90% confidence level to $\sim 16 \pm 0.7 R_g$ and the inclination goes up to $\sim 34 \pm 6^{\circ}$. This increase in the inclination is still consistent with previous works and the inner radius appears to be slightly truncated.

Our parameters show a canonical hard state with typical values, showing a hot corona dominating the emission (> 100 keV), a thin cold disk ~0.2 keV and a spectral index of 1.6-1.8. The values for the disk ionization and disk density are moderate to high which is expected in such stage of an outburst. By imposing a self-consistent disk reflection modeling, all these parameters remain similar but we account for Compton-scattered reflected photons, driving to a higher reflection fraction close to unity. These reflection values close to unity could be indicative of a compact corona or a corona closer to the compact object. Contrary to the typical picture of a hard state, the

inner disk is close to the ISCO.

We turn to two recurrent black hole transients which are useful touchstones with which to contextualize our results: GX 339-4 and H1743-322. Both systems have presented full outbursts and also recent stalled outbursts, which we use as a point of comparison here. In 2018, H1743-322 had a month-long stalled outburst observed by *Swift*, *NICER*, *NuSTAR* and *XMM-Newton*, which was analyzed by Stiele & Kong (2021). It's X-ray lightcurve and hardness evolution is very similar to that exhibited by MAXI J1813. It's peak brightness in this stalled outburst was in the vicinity 10-20 mCrab, whereas it's historical brightness peak has been $\gtrsim$ 1 Crab (Remillard & McClintock 2006). Stiele & Kong (2021) identify a similar $\Gamma \approx 1.65$ and a similarly cool accretion disk component $kT_{\rm disk} \approx 0.2$ keV. The disk ionization measured is relatively low, $\log \xi \approx 1.7-1.8$, and best estimate for the disk inner radius found to be $\sim 6-8\ R_g$. This large $R_{\rm in}$ and low ionization broadly comport with the expectation of its likely having low spin (Steiner et al. 2012a; Nathan et al. 2024), and would be consistent with moderate-to-no truncation. Notably, this analysis was analogous to our earlier non-self-consistent modeling of MAXI J1813 (Jiang et al. 2022), and just as the R_f was low in our earlier analysis, for H1743-322 the `relxill` fits returned a low reflection fraction ($\sim$ 0.3). As the reflection fraction increased $\sim$ 5-fold in this analysis from imposing self-consistency with the Comptonization of reflection emission, we expect this model would return a similarly larger R_f (closer to unity) for those H1743-322 data (see Dauser et al. 2016).

However, the 2017 stalled outburst of GX 339-4 presents very differently. That outburst, which lasted $\sim$ 5 months, was examined in García et al. (2019), primarily focused on two epochs using *Swift* and *NuSTAR* data. As for H1743-322, these observations were at a flux several percent of the historical peak of GX 339-4. The best-fitting model adopted in that analysis utilized a dual-lamppost coronal model for which the spectrum was canonically hard $\Gamma \sim 1.5$. The closer-in reflection component required very high ionization $\log \xi \sim 4$. Their fits found modest-to-no disk truncation and require that the spin must be quite high. This analysis also did not impose the self-consistent coronal scattering of reflection emission, but notably the reflection *strength* in their model was already very high; $\sim$ 2. Applying the self-consistent model would result in a higher-still reflection strength for that adopted picture. Alternatively, we tentatively suggest that the near-featureless reflection continuum associated with $\log \xi \sim 4$ would naturally be described by the Comptonized reflection emission from a *single* coronal component, negating the need for the more complex model adopted there. Such an analysis, however, is outside the scope of this work.

We also explored the fits to Obs 5 in search of statistically meaningful departure of the inner emissivity from the nominal profile $q = 3$. This was accomplished by freeing the inner emissivity (q_1) while fitting for a break radius, taken to be near $\sim 10 R_g$. However, the improvement in the fit was insignificant and more importantly, with the marginal improvement associated with a moderately higher q1, the inner radius became slightly smaller (while still falling within uncertainties). We also used the constraint on spin to very approximately estimate a possible distance of the source, making use of the thermal disk component. Here, we exchange *diskbb* for the relativistic disk model *kerrbb* (Ross & Fabian 2005). We adopt the same fiducial mass, 10 $M_\odot$, a spin and inclination linked to the reflection fits to Obs 5, and adopt a nominal color correction factor of 1.7. We fit for just the mass accretion rate and the distance, with a best-fitting distance of $\sim$1.5 kpc and a corresponding $L/L_{\rm Edd} \lesssim 0.1\%$. We have also explored a fit to Obs 5 in which, rather than fitting for radius, we assume the disk reaches the ISCO and fit instead for the spin. This results in a constraint that spin $a_* > 0.77$ and a best fit of $a_* \sim 0.9$, which is consistent with our benchmark fits using a free $R_{\rm in}$.

2.5 Conclusions

MAXI J1813-095 underwent a stalled outburst in 2018 during which it remained in a canonical hard state with Γ = 1.6-1.8, while exhibiting substantial spectral reflection. Assuming fiducial BH mass and distances of 10 $M_\odot$ BH and 8 kpc, respectively, the peak luminosity of this outburst is estimated as $\lesssim$1% of the Eddington luminosity. We present a self-consistent spectral analysis of the Comptonized reflection and disk continuum components, from which we constrain the inclination and inner radius to 28 ± 6.5° and ~2.1 ± 0.8 R_g, respectively. Conservatively adopting an extreme distance (~30 kpc), we can confidently rule out large-scale truncation for L $\lesssim$ 10% Eddington luminosity for this stalled outburst.

This is consistent with either a moderate spin ($a_* \gtrsim 0.7$) and no disk truncation, or else mild disk truncation for an extreme-spin BH ($a_* > 0.9$). By having imposed self-consistency in the model by scattering not just the thermal disk emission, but also reflection emission, in the corona, we find that the reflection fraction is much larger compared to earlier analyses omitting this consideration. Our higher reflection fraction, $R_f \approx 0.7 - 1.0$ **is in line** with expectation for typical static-coronal geometry, and so supports the viability of a static - rather than outflowing - corona. We find that for MAXI J1813, self-consistency of the coronal scattering does not substantially impact conclusions regarding the BH spin or inclination.

Data Availability

This study makes use of *NICER*, *Swift*/XRT, Chandra and *NuSTAR* archival data which can be acquired from HEASARC: https://heasarc.gsfc.nasa.gov/cgi-bin/W3Browse/w3browse.pl. This paper employs a list of Chandra datasets, obtained by the Chandra X-ray Observatory, contained in **[DOI: 20264, 20265, 20266]** https://doi.org/10.25574/cdc.288.

Appendix

2.A Pile-up in ACIS CC-Mode data

Photon pileup arises due to a high flux of X-ray photons reaching the detector. When two different X-ray photons strike the same or neighboring pixels within the detector's integration time, their signals are conflated as a single event. This results in a phenomenon known as"pileup", where the signals from multiple photons become merged and/or the event grade (sometimes called the "pattern") can be distorted, impacting spectral analysis by rejecting some real events and combining energies for others. *Chandra* observed this source on 02-28-2018, 03-06-2018 and 03-25-2018 in continuous clocking-mode (CC-mode), with data showing signs of photon pileup. To assess this, we compared our spectra without the central pixel, for which pileup is worst, to a spectrum including the central pixel and another spectrum excluding central pixel, one pixel up and one pixel down. In Figure 2.A.1 we show the three ratio plots to the spectra previously mentioned, in which we clearly see photon pileup manifest from 6-10 keV. To minimize these effects we obtained two more spectra excluding the central pixel and the two nearest pixels to the central pixel. We found that when excluding the central pixel the pileup effect between 6-10 keV decreases substantially. For this reason, we find it necessary to apply a corrective pile-up model and next fit *Chandra* with the other instruments and confirm that *Chandra* data are in agreement with the analysis performed in Section 2.3.

We employ the *pileup* model (Davis 2001) to correct for the redistribution of soft X-ray photons events in energy and grade. The *pileup* model was designed for correction for *Chandra* imaging data and operates by simulating the effects of photon pileup on the observed spectrum. It convolves an input spectral model with a pileup response. Notably, CC-mode data is 1-dimensional and so the pileup effects are likely to be somewhat distorted compared to 2-dimensional data. We accordingly allow for the frametime parameter — which for imaging data would usually be fixed – to be free.

2.B Chandra analysis

The *pileup* model is unfortunately incompatible with *simplcut*. The former requires the default energy grid to be used for computations, whereas the latter requires an extended energy grid to compute redistribution properly. As a consequence, we adopt an approximate model which describes the same behavior as in our main analysis, but here we substitute `simplcut` with `nthcomp` as in Jiang et al. (2022).

In Table 2.B.1, we present the best fit including *Chandra* data for observations 5, 6 and 7. We set the same free parameters as those in the standard analysis and add the *pileup* model. The *Chandra pileup* model fits for the frametime and the alpha parameter, which α parameterizes "grade migration" in the detector, and represents the probability, per photon count greater than one, that the piled event is not rejected by the spacecraft software as a"bad event". Specifically, if

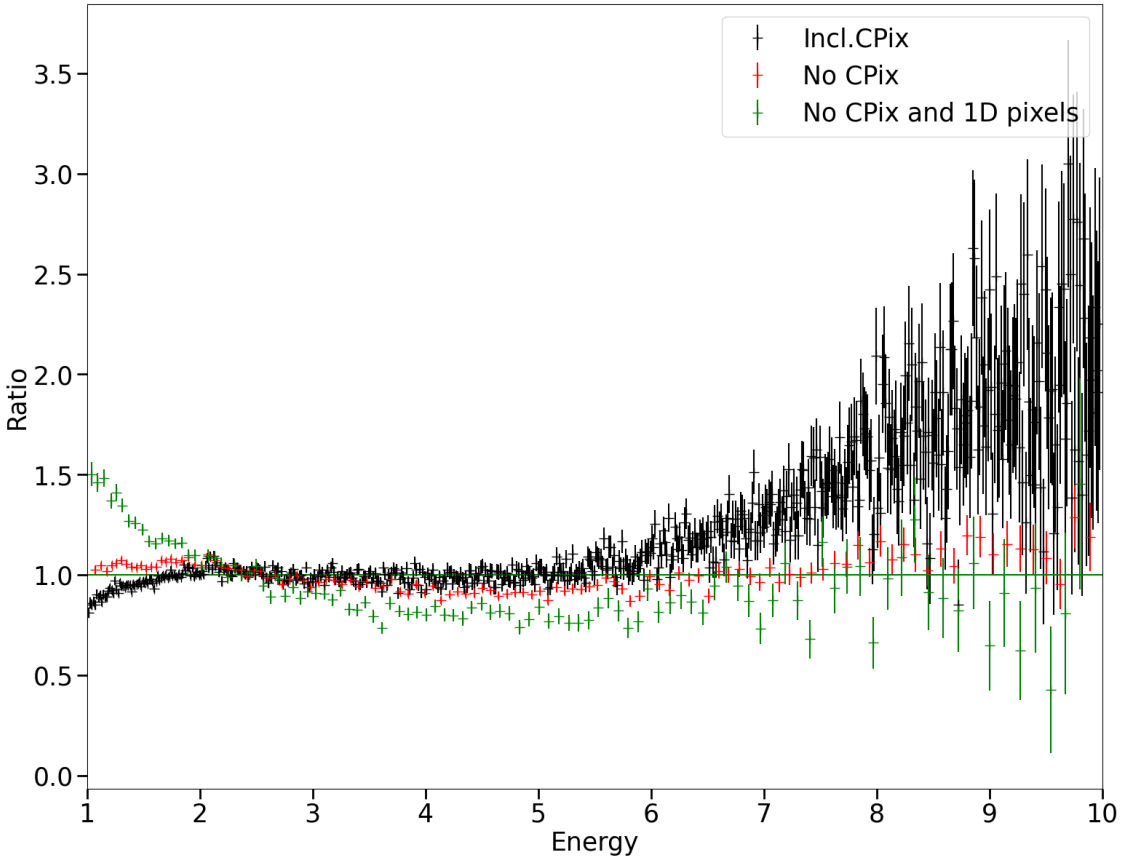

Figure 2.A.1: In this figure shows three ratio Chandra spectres plot (black full source, red excluding the central pixel and in green excluding the central pixel and the immediately adjacent pixels up and down) for observation 5 with a simple model `TBabs(simplcut(diskbb))`.

N photons are piled together in a single frame, the probability of them being retained (as a single photon event with their summed energy) is given by $\alpha^{(N-1)}$. The true frametime of CC-mode is 2.85ms, but the best fit is a factor ~3 larger. We speculate that this is a reasonable increase given the compression from a 2-dimensional image to 1-dimensional streak.

As a bottom line, we obtain broadly similar physical quantities as reflected in Table 2.3. Including *Chandra* data we didn't fit it self-consistently so the R_f is unreliable compared to the Table 2.3. Figure 2.B.1 shows the three spectra with Chandra that corroborate that Chandra observations are consistent with the other instrument observations. We find that this practical approach, namely fitting CC-mode data with the *pileup* model using a fitted frametime, is successful at reconciling the mildly piled-up *CC-mode* data with the other observatories.

Table 2.B.1: Best-fit parameters for the averaged *NICER* (Ni), *Swift* (S), *NuSTAR* (Nu) and *Chandra* (Ch) spectra of MAXI J1813. The quoted errors are at the 90% confidence level with a BH spin fixed at 0.998, N_H fixed at 1.35×10^{22} cm^{-2} and reflection fraction fixed at 1 along the observations. Obsid5-Obsid7

Parameters	Obs 5 (Ni5+S5+Nu1+Ch1)	Obs 6 (S6+Nu2+Ch2)	Obs 7 (S7+Nu3+Ch3)
Γ	$1.54^{+0.01}_{-0.01}$	$1.66^{+0.04}_{-0.02}$	$1.69^{+0.01}_{-0.01}$
kT_{disk}	$0.14^{+0.01}_{-0.01}$	$0.51^{+0.03}_{-0.4}$	$0.46^{+0.01}_{-0.01}$
$Norm._{disk}$	$(6^{+0.6}_{-0.6})\times10^{-2}$	$(8^{+3}_{-0.3})\times10^{-2}$	$(9^{+0.4}_{-0.4})\times10^{-2}$
Incl.	12^{+12}_{-7}	42^{+14}_{-4}	25^{+5}_{-7}
R_{in} (R_g)	$8.2^{+2.8}_{-1.6}$	$8.8^{+12.3}_{-5.9}$	$7.7^{+3.2}_{-2.4}$
log ξ (erg cm s^{-1})	$3.65^{+0.04}_{-0.04}$	$1.99^{+0.11}_{-0.25}$	$3.1^{+0.1}_{-0.1}$
$Z_{Fe}(Z_\odot)$	$0.8^{+0.1}_{-0.1}$	$0.98^{+1}_{-0.3}$	$1.8^{+0.7}_{-0.5}$
log n(cm^{-3})	$19.8^{+0.1}_{-0.4}$	20	$16^{+1.5}_{-0.8}$
kT_e(keV)	254^{+109}_{-90}	>267	189^{+160}_{-110}
$Norm._{Refl}$	$(1.5^{+0.2}_{-0.2})\times10^{-3}$	$(1^{+0.7}_{-0.2})\times10^{-3}$	$(7^{+1}_{-1})\times10^{-4}$
Frame time	$(5.3^{+3.2}_{-1.6})\times10^{-3}$	$(8.8^{+8.7}_{-4.1})\times10^{-3}$	$(7^{+5}_{-3})\times10^{-3}$
Alpha	$0.67^{+0.26}_{-0.22}$	$0.47^{+0.35}_{-0.14}$	$0.5^{+0.4}_{-0.2}$
dNorm. (ACIS)	$0.85^{+0.03}_{-0.02}$	1.51	1.58
dΓ (ACIS)	0	0	0
dNorm.** (XRT)	$0.91^{+0.02}_{-0.02}$	$0.90^{+0.01}_{-0.01}$	0.85
dΓ (XRT)	0	0	0
dNorm. (FPMA)	1	1	1
dΓ (FPMA)	0	0	0
dNorm. (FPMB)	$0.99^{+0.003}_{-0.003}$	$0.97^{+0.004}_{-0.004}$	0.98
dΓ (FPMB)	0	0	0
dNorm. (NICER)	$0.96^{+0.02}_{-0.02}$	-	-
dΓ (NICER)	$(8.6^{+1.2}_{-1.2})\times10^{-2}$	-	-
χ^2/ν	1289/1077	1040/651	881/653

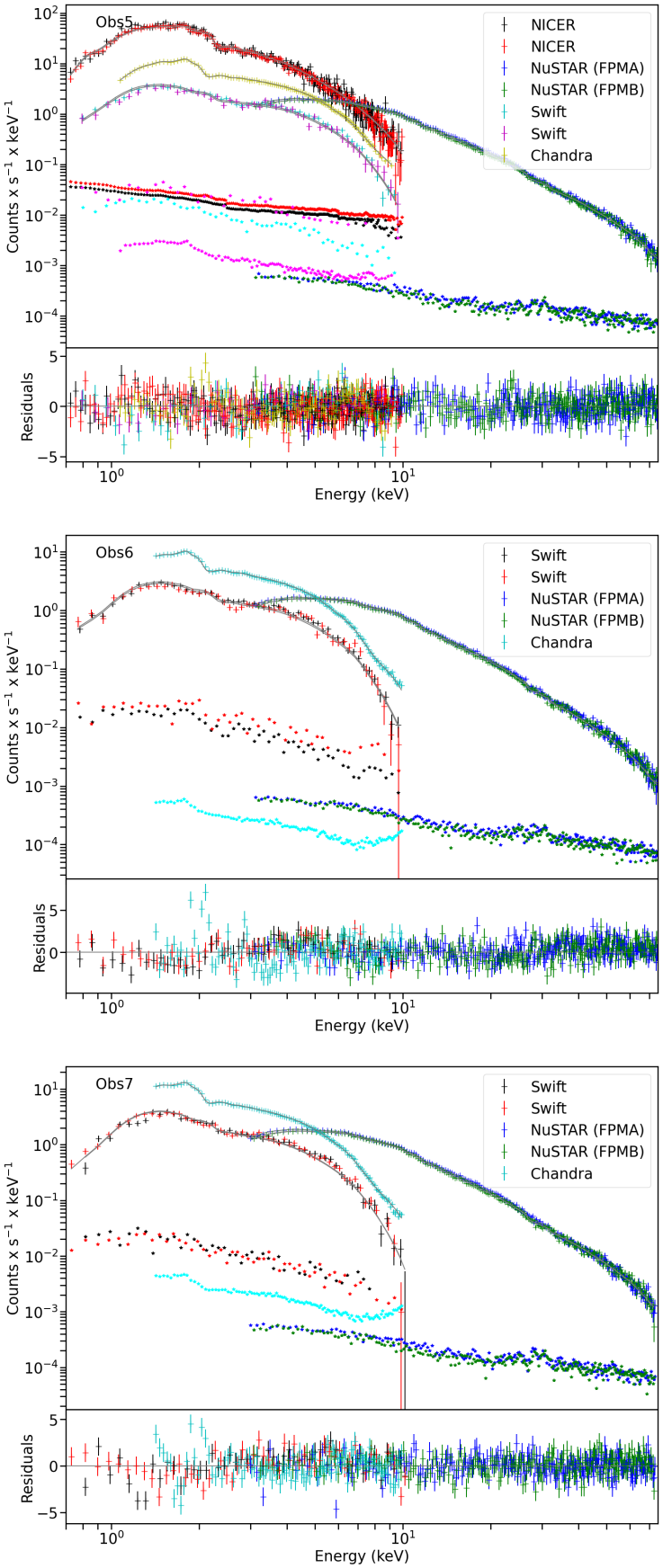

Figure 2.B.1: *Top*: *Chandra* in yellow, jointly with *NICER*, *Swift*, and *NuSTAR*, corresponding to observation 5. *Middle*: *Chandra* data is represented by the color cyan jointly with *Swift* and *NuSTAR*. *Bottom*: *Chandra* data is represented by the color cyan jointly with *Swift* and *NuSTAR*. In all cases, *Chandra* is consistent with the other instruments.

Chapter 3

Detection of Self-Obscuration and Disk Winds of MAXI J1803-298

Content of this Chapter

I present here the results of the analysis of 28 epochs of MAXI J1803-298 black hole X-ray binary candidate using the *NICER* telescope. These results are submitted to *The Astrophysical Journal* and being reviewed. I was responsible for the complete data reduction, analysis, and writing the article. MAXI J1803-298 is a black hole X-ray binary of unknown distance and mass that underwent into a complete outburst in 2021. I studied 28 epochs from SIMS to SS tracking the evolution of the winds with the surprise of the self-obscured inner disk detection.

3.1 Introduction

MAXI J1803-298 (hereafter MAXI J1803) is a BH candidate discovered in May 1, 2021, by the *Monitor of All-sky X-ray Image* Gas Slit Camera (MAXI/GSC) at 19:50 UT. Its coordinates are R.A. = 270.923° and Dec = -29.804° (J2000) (Serino et al. 2021). Following its discovery, several telescopes, including the *MeerKAT* (Espinasse et al. 2021), Neutron star Interior Composition Explorer (*NICER*) (Gendreau et al. 2021), Neil Gehrels Swift Observatory (*Swift*) (Gropp et al. 2021), Multicolor Imaging Telescopes for Survey and Monstrous Explosions (*MITSuME*) (Hosokawa et al. 2021), Southern African Large Telescope (*SALT*) (Buckley et al. 2021), International Gamma-Ray Astrophysics Laboratory (*INTEGRAL*) (Chenevez et al. 2021), Nuclear Spectroscopic Telescope Array (*NuSTAR*) (Xu & Harrison 2021), Hard X-ray Modulation Telescope (*HXMT*) (Wang et al. 2021), and Astronomy Satellite (*AstroSAT*) (Jana et al. 2021a), conducted follow-up observations across multiple energy bands of this source. Subsequent observations revealed a transition between X-ray spectral states in the months following its discovery (Steiner et al. 2021). *Swift* (Miller & Reynolds 2021), *NuSTAR* (Xu & Harrison 2021), and *NICER* (Homan et al. 2021, Miller & Reynolds 2021) detected strong periodic X-ray absorption dips in MAXI J1803-298, indicating a highly inclined system (> 60°) with respect to the line of sight (Kostić, U. et al. 2009; Ponti et al. 2012; Paice et al. 2019; Buisson et al. 2021; Adegoke et al. 2024). *NICER* (Ubach et al. 2021), *AstroSat* (Chand et al. 2021), and *HXMT* (Wang et al. 2021) detected a type-B low-frequency quasi-periodic oscillations (QPOs) during the follow up observations.

In this work, we examine the geometry of the inner accretion flow onto MAXI J1803 during both the SIMS and SS. The SS analysis demonstrates that the X-ray emission is dominated by the

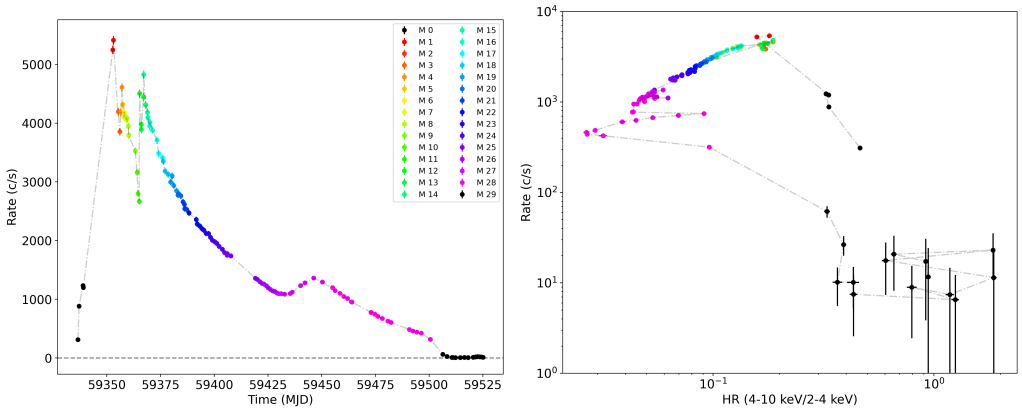

Figure 3.1.1: *Left*: The NICER light curve, normalized to 52 Focal Plane Modules (FPMs), throughout the entire outburst. *Right*: The HID of the full outburst, starting at the HS and finishing the outburst in the fainter HS. In both panels, the SIMS and SS observations are color-coded by time, showing which spectra were merged.

thermal disk, along with associated Fe XXV and Fe XXVI absorption lines, typically indicative of winds, which is common for highly inclined BH transients in the SS (Chand et al. 2022). We present the first evidence for self-obscuration associated with high mass accretion rates near the luminosity peak (i.e. over timescales of days, unlike HS dips). To assess this finding, we study the disk normalization throughout the SIMS and SS and compare it with the canonical BH transient GX 339-4 and a high inclined system such as H1743-322 during a bright, faint and "stalled" outbursts to see if there is a similar behavior as MAXI J1803.

The chapter is organized as follows. We introduce the *NICER* observations and data reduction in Section 3.2. In Section 3.3 we describe the data analysis and present our results. We offer a discussion and conclusions in Section 3.4 and Section 3.5, respectively.

3.2 Observations and Data Reduction

3.2.1 NICER

As MAXI J1803 entered into an outburst, *NICER*, which is located on the International Space Station, observed it regularly. The main objectives of *NICER* are to characterize neutron stars, specifically to constrain the equation of state. We process *NICER* data using *NICERDASv10* distributed by HEASOFT v6.31.1. CALDB calibration files xti20221001 have been used for the data reduction. We reduced the data using the *NICER* pipeline utilities *nicerl2* and *nicerl3*. Specifically, we used the task *nicerl3-lc* and *nicerl3-spec* to obtain the lightcurves and spectra of each observation. The energy range adopted for NICER analysis was 0.25-10 keV, appropriate for studying the X-ray properties of our source. Because of the low background flux estimates obtained using the nibackgen3C50 task, we did not carry out background subtraction in the light curve analysis. We combined the resulting spectral data in time bins from 125 observations to 30 merged spectra (M0–M29) in order to achieve a minimum signal of ~20 million counts per spectrum. The merging was required to enhance the detection of Fe XXV and Fe XXVI absorption lines in the individual spectra (see Figure 3.2.1). A 1% systematic error was included in the data to account for the calibration uncertainties at lower energies. Table 3.2.1 shows the date, exposure time, count rate, hardness ratio (4-10 keV /2-4 keV), total counts and the flux from 0.25 to 10 keV of the merged spectra in the SIMS and SS.

Table 3.2.1: Table of all the MAXI J1803-298 merged spectra. We present the exposure times, observation dates and photon count rates of the entire SIMS and SS after the merging process. The merged rate is normalized to an equivalent 52 FPMs active.

Merged observation	Time (MJD-59350)	Exp. time (ks)	$\text{Rate}_{\text{Norm.}}$ (10^3 c/s)	Hardness	Counts (10^6)	$F_{0.25-10keV}$ (10^{-8} erg/s)
M1	2.75-3.01	14.9	5.3	0.15-0.18	79.9	1.42
M2	5.01	5.8	4.2	0.17	25.6	1.03
M3	5.34-6.05	6.8	3.7	0.17-0.16	27.6	0.94
M4	6.50-7.02	8.4	4.4	0.16-0.17	33.6	0.93
M5	7.40	7.6	4.1	0.17	28.1	0.84
M6	7.98-7.18	5.4	3.9	0.17-0.18	22.9	1.04
M7	9.08	4.6	3.8	0.19	21.1	1.28
M8	9.23-10.13	5.6	3.5	0.16-0.18	25.1	1.21
M9	13.21	4.9	3.2	0.13	20.5	0.98
M10	14.05-14.5	5.3	4.0	0.13	21.6	0.95
M11	15.02	6.0	4.6	0.13	23.5	0.91
M12	15.21-16	8.7	4.2	0.13	34.4	0.91
M13	16.08-17.01	7.7	4.0	0.12-0.13	29.6	0.88
M14	17.08-18.05	12.3	3.9	0.12	46.6	0.85
M15	18.89-19.08	9.9	3.6	0.11	35.8	0.80
M16	19.85-21.21	11.5	3.4	0.10-0.11	39.1	0.73
M17	22.76-24.05	6.2	3.2	0.10-0.11	20.0	0.68
M18	26.18-28.51	8.1	3.0	0.09-0.10	24.4	0.62
M19	29.68-32.38	9.6	2.8	0.09	26.9	0.56
M20	33.11-34.39	9.4	2.6	0.09	25.1	0.53
M21	35.48-37.18	9.8	2.4	0.08-0.09	24.6	0.49
M22	38.21-44.20	9.0	2.1	0.08	20.0	0.42
M23	45.10-48.22	10.3	2.0	0.07-0.08	20.8	0.38
M24	49.10-53.71	11.1	1.8	0.06-0.07	21.0	0.34
M25	54.74-55.96	13.6	1.2	0.05-0.06	20.9	0.27
M26	71.14-79.17	19.7	1.2	0.05-0.06	22.3	0.19
M27	80.05-102.26	19.4	1.0	0.05	22.1	0.19
M28	105.06-150.59	25.9	0.9	0.05-0.09	17.6	0.19

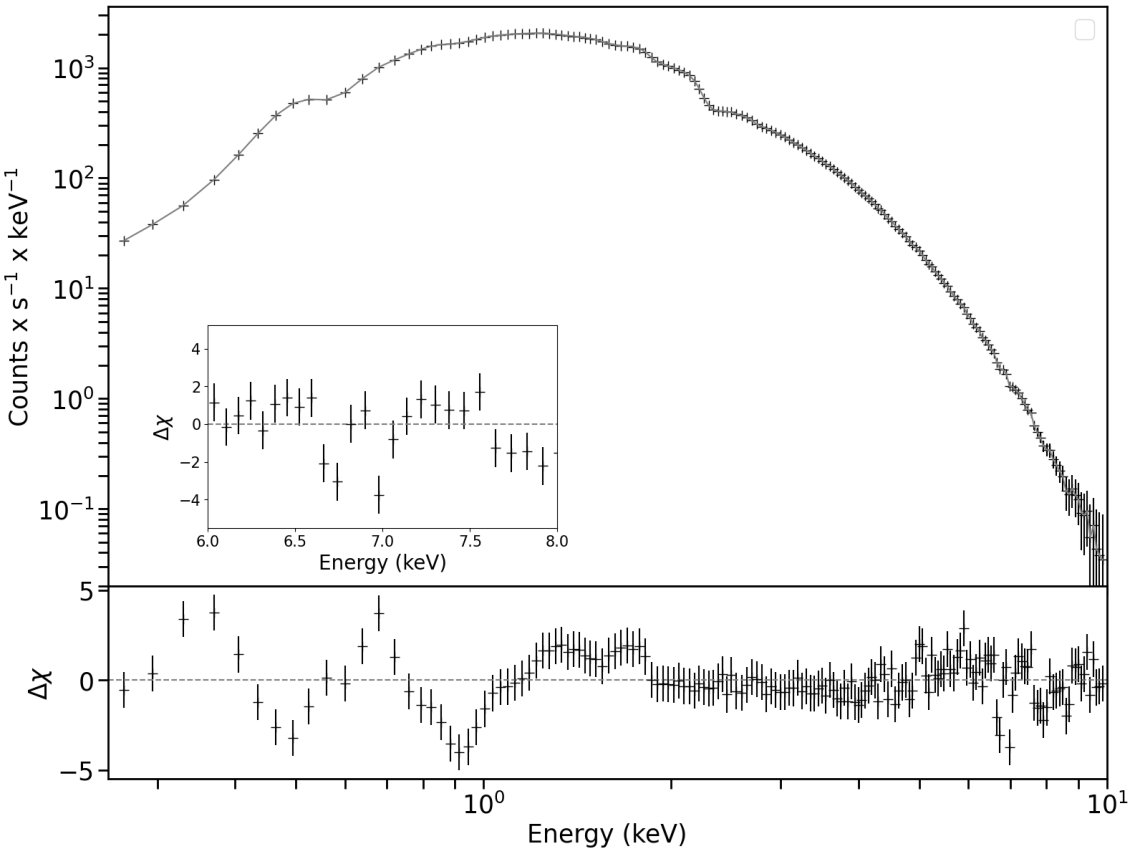

Figure 3.2.1: Example of one of the soft state spectra (M18) observed with *NICER*, which shows prominent absorption lines between 6–7 keV. The inset shows to show the presence of two absorption lines at 6.69 keV and 6.97 keV, corresponding to Fe XXV and Fe XXVI.

3.3 Data Analysis & Results

In this section, we present the best-fit models for both the continuum and wind components of the spectrum, at 90% confidence level unless otherwise noted. In Figure 3.1.1, we present the *NICER* light curve and the HID of the months-long outburst of MAXI J1803. For the continuum modeling, we utilize data from the 0.25—10 keV energy range, applying a χ^2 fitting statistic and a 1% systematic uncertainty to account for calibration residuals. Spectra M1 to M28 show wind absorption lines. These data are unable to reliably constrain the width of the line features (see Figure 3.2.1), and so we fix the width at a reasonable and small value of 10 eV, which corresponds to a velocity spread of $\sim$ 450 km s^{-1}. Wind detection fits utilized just the 2–10 keV energy band, intentionally excluding lower-energy features attributed to calibration systematics that could compromise the accuracy of the fits, and utilizing the *pg*-statistic (i.e., Poisson-distributed data and Gaussian-distributed background). The *pg*-statistic was utilized in order to maximize our sensitivity to the presence of wind features, where the continuum structure was not the main focus. That is, for fitting the continuum, we employed systematic uncertainties on a broadband spectral fit, whereas to maximize sensitivity to subtle line features, we fit a narrower range of data centered on the wind features, and omitting any systematic uncertainties.

3.3.1 Continuum Modeling

We began by performing a preliminary spectral analysis on each observation using the phenomenological model *TBabs*×(*simpl* × *diskbb*). This initial fit revealed the presence of iron absorption lines. In this model, *TBabs* accounts for Galactic hydrogen absorption (Wilms et al. 2000), *simpl* models the Comptonization of the disk emission (Steiner et al. 2009), and *diskbb* represents the blackbody emission from the disk (Makishima et al. 1986). We identified four observations at the beginning of the outburst in the HS and fourteen additional observations at the end, also in the HS. However, due to the the structure obstruction of the international space station (ISS) between observations, we could not capture the transition of the source into the SIMS.

After this initial analysis, we replaced the Galactic absorption model `TBabs` with `TBfeo`, which allows for non-standard abundances of iron and oxygen, helping to mitigate features in the lower energy band of the spectra (Figure 3.2.1). In the 6–7 keV energy range, two absorption lines corresponding to Fe XXV and Fe XXVI (~6.69 and ~6.97 keV) are clearly visible (Figure 3.2.1). However, the lower energy band still shows residual features due to calibration systematics with *NICER*. This was accounted for by the 1% systematic error used when fitting the continuum.

3.3.2 Phenomenological Wind Modeling

The SS data reveal prominent absorption lines at 6.69 keV and 6.97 keV, attributed to highly ionized iron species, Fe XXV and Fe XXVI. These lines, detected using *NICER*, are indicative of ionized disk winds. Their properties, such as equivalent widths and velocity shifts, suggest the presence of an outflow. By tracking the evolution of these lines throughout the SS, we can monitor changes in the ionization state, density, and velocity of the disk winds. This provides critical insights into the interaction between the accretion disk and outflows, shedding light on the mechanisms governing angular momentum loss and the dynamics of state transitions in BHXRBs.

To fit the iron absorption lines in the 6–7 keV range, we conducted a third analysis of the 91 SS spectra, that after the merging process become 28 different spectra, going from M1 to M28 (where M0 and M29 correspond to HS). The resulting spectra, each with over 20 million counts (see Table 3.2.1), improved the signal-to-noise ratio in the iron fluorescence band, enhancing sensitivity to the Fe XXV and Fe XXVI lines while reducing background noise. Now a suitable model is needed to account for absorption from the disk wind. We added two `Gaussian` components to the

previous model. The model used in this case is `TBfeo×(simpl×diskbb)+gaussian+gaussian`, with the hydrogen column density fixed at $N_{\rm H} = 0.33 \times 10^{22}$ cm^{-2}, the ISM oxygen abundance at 1.23 nominal abundance [O], and the iron abundance [Fe] at 0.33 nominal ISM abundance, from Section 3.3.1. The energies of the *Gaussian* components were fixed at the rest-frame energies of Fe XXV and Fe XXVI (6.69 and 6.97 keV, respectively), with a line width of 0.01 keV. Table 3.3.1 presents the best-fit results for each merged spectrum at the 90% confidence level (C.L.). Based on the high scattered fraction ($f_{sc} > 0.25$) and a hardness ratio between 0.15-0.19, the first 8 spectra were characterized to be in the SIMS.

The powerlaw index was constrained between 1.2 and 3.5 to cover the observed energy range. The strengths of both *Gaussian* components were allowed to take negative values to account for the iron absorption lines. Owing to the absolute energy uncertainty of *NICER*, which their calibration assessment reports as 30 eV, a wind velocity manifesting as shifts in the iron lines is not significantly detected with an upper limit ~ 1300 km s^{-1}.

We also measured the equivalent widths of Fe XXV and Fe XXVI at a 90% C.L., including that the absorption from Fe XXVI dominates initially, while Fe XXV strengthens as the system fades during the SS. By the end of the SS, the equivalent widths of both lines become comparable. The strength parameters indicate that Fe XXVI is typically ~10 times stronger than Fe XXV at the beginning of the SS. Figure 3.3.1 illustrates the evolution of spectral parameters over the outburst, showing the equivalent widths of Fe XXV and Fe XXVI as a function of wind evolution in time.

3.3.3 Physical Wind Modeling

To investigate wind velocities, we analyzed five epochs (M12, M14, M18, M22, and M27) to trace the evolution of these disk wind parameters during the SS. We employed the absorption wind model `zxipcf` (Miller et al. 2006; Reeves et al. 2008) to characterize the wind parameters, which was developed using `XSTAR` (Kallman & Bautista 2001; Kallman et al. 2004) instead of the *Gaussian* components (Miller et al. 2006; Reeves et al. 2008). This model was used to estimate the wind properties (column density, ionization, and speed).

The ionization parameter (ξ) is related to the source luminosity L and wind density (n) by:

$$\xi = \frac{L}{nR^2_{\rm wind}} \tag{3.1}$$

where $R_{\rm wind}$ is the radius where the wind is located with respect to the compact object. We relate this to the column density in the wind ($N_{\rm H,wind}$), approximating $nR \sim N_{\rm H,wind}$. Therefore,

$$R_{wind} \approx \frac{L}{N_{H,wind}\,\xi}. \tag{3.2}$$

We adopt fiducial values for the black hole mass, 10 $M_\odot$, and a distance of 8 kpc. The wind radius (R_{wind}) corresponding to the peak of luminosity can be estimated (e.g., Coughenour et al. 2023; Adegoke et al. 2024; Zhang et al. 2024). In Zhang et al. (2024), `XSTAR` was employed for wind fitting using *NICER* data. They report an estimated velocity shift of $z = 0.004c$, which is less than absolute energy uncertainty. Their values of $N_{H,wind}$ are from 1.9 to 9.5×10^{22} cm^{-2} and ξ of $10^{4.2-5.1}$ erg·cm^{-1}·s^{-1} are consistent with those observed with `zxipcf` model used in this study. The different epochs that we studied to track the wind evolution showed $N_{\rm H,wind}$ of $1.5{\times}10^{22}$, $23.1{\times}10^{22}$, $3.0{\times}10^{22}$, $8.4{\times}10^{22}$, and $3.42{\times}10^{22}$ cm^{-2} and ξ of $10^{4.4}$, $10^{5.2}$, $10^{4.0}$, $10^{4.3}$ and $10^{3.6}$ erg cm^{-1} s^{-1} respectively.

Based on our fits in comparison to Eq. 3.2, we find that the disk winds are found at radii $R_{\rm wind} \approx 10^5\ R_g$. The corresponding wind velocities is estimated as $v \sim (GM/R_{\rm wind})^{1/2} \lesssim 1000$ km s^{-1}, consistent with our velocity upper limit associated with the non-detection of a significant velocity shift.

Table 3.3.1: MAXI J1803-298 SIMS and SS wind-absorption fits from M1 to M28. The iron absorption lines (Fe XXV and Fe XXVI) from the winds have been fixed to 6.69 keV and 6.97 keV as well and line width fixed to 0.01 keV. The errors are at 90% confidence.

Merged Obs.	Γ[a]	$f_{sc.}$	$kT_{\rm disk}$ keV	N_{Disk} 10^3	$N_{\rm Fe25}$[b] 10^{-5}	$N_{\rm Fe26}$[b] 10^{-5}	$EW_{\rm Fe\,25}$ eV	$EW_{\rm Fe26}$ eV	pg/ν[c]	χ^2/ν[d]
M1	$3.23^{+0.05}_{-0.05}$	$0.48^{+0.03}_{-0.02}$	$0.88^{+0.01}_{-0.01}$	$1.10^{+0.04}_{-0.03}$	1^{+10}_{-10}	-24^{+10}_{-10}	$-0.1^{+0.5}_{-1.1}$	$4.9^{+1.0}_{-0.4}$	327/137	288/191
M2	$2.82^{+0.03}_{-0.03}$	$0.64^{+0.04}_{-0.04}$	$0.61^{+0.01}_{-0.01}$	$3.3^{+0.3}_{-0.2}$	34^{+14}_{-14}	0.1^{+13}_{-13}	$-8.7^{+1.5}_{-1.2}$	$-0.6^{+4.2}_{-4.1}$	256/124	197/191
M3	$2.76^{+0.02}_{-0.02}$	$0.60^{+0.03}_{-0.03}$	$0.61^{+0.01}_{-0.01}$	$3.1^{+0.2}_{-0.2}$	-2^{+12}_{-12}	-14^{+11}_{-11}	$0.7^{+3.3}_{-0.5}$	$4.1^{+1.4}_{-4.2}$	266/124	240/191
M4	$2.77^{+0.02}_{-0.02}$	$0.61^{+0.03}_{-0.03}$	$0.60^{+0.01}_{-0.01}$	$3.0^{+0.2}_{-0.2}$	-0.8^{+10}_{-10}	-5^{+10}_{-10}	$0.2^{+4.1}_{-1.8}$	$1.4^{+1.1}_{-2.0}$	266/127	242/191
M5	$2.71^{+0.02}_{-0.02}$	$0.58^{+0.03}_{-0.02}$	$0.59^{+0.01}_{-0.01}$	$3.2^{+0.2}_{-0.2}$	3.4^{+11}_{-11}	-8.5^{+10}_{-10}	$-1.1^{+1.2}_{-2.8}$	$2.9^{+1.3}_{-4.3}$	200/124	210/191
M6	$2.81^{+0.03}_{-0.03}$	$0.63^{+0.04}_{-0.04}$	$0.65^{+0.01}_{-0.02}$	$2.5^{+0.2}_{-0.2}$	26^{+15}_{-15}	-3^{+14}_{-14}	$-6.2^{+1.5}_{-4.2}$	$0.7^{+2.0}_{-1.0}$	215/124	202/191
M7	$2.98^{+0.05}_{-0.05}$	$0.62^{+0.06}_{-0.05}$	$0.79^{+0.02}_{-0.02}$	$1.5^{+0.1}_{-0.1}$	14^{+19}_{-19}	-20^{+17}_{-17}	$-2.5^{+1.4}_{-2.8}$	$4.0^{+3.1}_{-2.9}$	199/124	239/191
M8	$2.91^{+0.07}_{-0.07}$	$0.41^{+0.03}_{-0.03}$	$0.86^{+0.01}_{-0.01}$	$1.10^{+0.05}_{-0.05}$	10^{+15}_{-15}	-45^{+14}_{-14}	$-2.1^{+0.7}_{-3.1}$	$10.7^{+1.9}_{-2.1}$	144/125	255/191
M9	$3.17^{+0.22}_{-0.22}$	$0.16^{+0.03}_{-0.03}$	$0.91^{+0.01}_{-0.01}$	$0.85^{+0.03}_{-0.02}$	7^{+12}_{-12}	-15^{+11}_{-11}	$-3.1^{+2.1}_{-3.1}$	$7.4^{+6.7}_{-5.4}$	134/122	285/191
M10	$3.10^{+0.30}_{-0.29}$	$0.10^{+0.03}_{-0.02}$	$0.93^{+0.01}_{-0.01}$	$0.80^{+0.02}_{-0.02}$	15^{+11}_{-11}	-18^{+10}_{-10}	$-7.2^{+3.0}_{-0.5}$	$10.1^{+5.2}_{-2.3}$	120/122	312/191
M11	$2.96^{+0.23}_{-0.24}$	$0.11^{+0.02}_{-0.02}$	$0.92^{+0.01}_{-0.01}$	$0.78^{+0.02}_{-0.02}$	10^{+10}_{-10}	-27^{+9}_{-9}	$-4.5^{+3.6}_{-0.0}$	$15.0^{+1.9}_{-6.0}$	184/122	319/191
M12	$3.28^{+0.17}_{-0.17}$	$0.16^{+0.02}_{-0.02}$	$0.90^{+0.01}_{-0.01}$	$0.85^{+0.02}_{-0.02}$	-4^{+8}_{-8}	-12^{+10}_{-10}	$2.0^{+3.3}_{-2.0}$	$6.8^{+2.5}_{-4.3}$	199/126	367/191
M13	$3.10^{+0.23}_{-0.22}$	$0.10^{+0.02}_{-0.02}$	$0.91^{+0.01}_{-0.01}$	$0.81^{+0.02}_{-0.02}$	-8^{+8}_{-8}	-22^{+7}_{-7}	$4.5^{+3.3}_{-5.1}$	$14.3^{+1.5}_{-4.5}$	194/124	323/191
M14	$2.89^{+0.24}_{-0.23}$	$0.06^{+0.01}_{-0.01}$	$0.91^{+0.01}_{-0.01}$	$0.77^{+0.01}_{-0.01}$	-4^{+6}_{-6}	-19^{+5}_{-5}	$2.7^{+3.1}_{-3.0}$	$14.5^{+3.5}_{-3.3}$	323/127	328/191
M15	$2.72^{+0.37}_{-0.36}$	$0.04^{+0.01}_{-0.01}$	$0.91^{+0.01}_{-0.01}$	$0.76^{+0.01}_{-0.01}$	-8^{+6}_{-6}	-27^{+5}_{-5}	$6.4^{+1.2}_{-4.7}$	$24.8^{+2.7}_{-2.2}$	302/125	303/191
M16	$>3.42^{*}$	$0.04^{+0.01}_{-0.01}$	$0.90^{+0.01}_{-0.01}$	$0.76^{+0.01}_{-0.01}$	-18^{+5}_{-5}	-20^{+4}_{-4}	$17.9^{+1.5}_{-5.4}$	$24.3^{+0.5}_{-5.4}$	324/125	332/191
M17	$>3.38^{*}$	$0.05^{+0.01}_{-0.01}$	$0.86^{+0.01}_{-0.01}$	$0.81^{+0.01}_{-0.01}$	-20^{+6}_{-6}	-21^{+6}_{-6}	$21.7^{+6.7}_{-5.9}$	$27.8^{+4.6}_{-4.7}$	149/120	264/191
M18	$>3.39^{*}$	$0.04^{+0.01}_{-0.01}$	$0.85^{+0.01}_{-0.01}$	$0.81^{+0.01}_{-0.01}$	-12^{+5}_{-5}	-10^{+5}_{-5}	$16.0^{+3.3}_{-4.6}$	$16.7^{+2.2}_{-5.9}$	194/120	285/191
M19	$>3.42^{*}$	$0.03^{+0.01}_{-0.01}$	$0.84^{+0.01}_{-0.01}$	$0.79^{+0.01}_{-0.01}$	-18^{+4}_{-4}	-13^{+4}_{-4}	$31.2^{+6.4}_{-4.7}$	$29.1^{+3.4}_{-8.2}$	220/120	312/191
M20	$>3.43^{*}$	$0.03^{+0.01}_{-0.01}$	$0.82^{+0.01}_{-0.01}$	$0.81^{+0.01}_{-0.01}$	-14^{+4}_{-4}	-9^{+4}_{-3}	$26.2^{+7.4}_{-3.8}$	$22.6^{+7.2}_{-2.6}$	231/119	336/191
M21	$>3.38^{*}$	$0.03^{+0.01}_{-0.01}$	$0.81^{+0.01}_{-0.01}$	$0.80^{+0.01}_{-0.01}$	-10^{+4}_{-4}	-8^{+3}_{-3}	$22.6^{+0.6}_{-9.5}$	$22.0^{+6.0}_{-4.2}$	204/119	322/191
M22	$>3.39^{*}$	$0.04^{+0.01}_{-0.01}$	$0.77^{+0.01}_{-0.01}$	$0.87^{+0.01}_{-0.01}$	-9^{+3}_{-3}	-9^{+3}_{-3}	$27.8^{+4.4}_{-5.1}$	$34.1^{+11.8}_{-15.5}$	148/118	273/191
M23	$>3.38^{*}$	$0.05^{+0.01}_{-0.01}$	$0.74^{+0.01}_{-0.01}$	$0.90^{+0.01}_{-0.01}$	-10^{+3}_{-3}	-4^{+3}_{-3}	$32.1^{+5.1}_{-4.9}$	$18.1^{+7.8}_{-6.0}$	156/119	300/191
M24	$>3.43^{*}$	$0.03^{+0.01}_{-0.01}$	$0.73^{+0.01}_{-0.01}$	$0.87^{+0.01}_{-0.01}$	-7^{+2}_{-2}	-3^{+2}_{-2}	$32.8^{+6.3}_{-14.7}$	$17.8^{+2.1}_{-11.1}$	239/117	399/191
M25	$>3.44^{*}$	$0.03^{+0.01}_{-0.01}$	$0.69^{+0.01}_{-0.01}$	$0.92^{+0.01}_{-0.01}$	-4^{+2}_{-2}	-2^{+2}_{-2}	$27.6^{+1.7}_{-7.6}$	$22.3^{+6.4}_{-6.7}$	178/114	417/191
M26	$1.96^{+0.21}_{-0.21}$	$0.01^{+0.01}_{-0.01}$	$0.63^{+0.01}_{-0.01}$	$0.94^{+0.01}_{-0.01}$	-3^{+1}_{-1}	-1^{+1}_{-1}	$28.7^{+9.4}_{-8.5}$	$11.8^{+15.4}_{-8.7}$	109/115	347/191
M27	$>3.44^{*}$	$0.04^{+0.01}_{-0.01}$	$0.63^{+0.01}_{-0.01}$	$0.97^{+0.01}_{-0.01}$	-3^{+1}_{-1}	-1^{+1}_{-1}	$33.8^{+4.6}_{-3.4}$	$0.02^{+16.0}_{-8.8}$	158/113	444/191
M28	$1.88^{+0.17}_{-0.17}$	$0.01^{+0.01}_{-0.01}$	$0.58^{+0.01}_{-0.01}$	$0.88^{+0.01}_{-0.01}$	-1^{1}_{1}	-2^{+1}_{-1}	$20.6^{+10.0}_{-5.1}$	$31.9^{+16.1}_{-5.0}$	169/113	586/191

[a] Γ has been bounded between 1.2 and 3.5. All Γ with a lower limit are quoted at 90% confidence level.

[b] Negative values correspond to detected absorption lines.

[c] We used from 2 to 10 keV to fit the absorption lines.

[d] We used 0.25 to 10 keV to fit the continuum.

3.3.4 Self-obscured Slim Disk

In the SIMS, NICER observations revealed a gradual decrease in X-ray luminosity over a timescale of several days, just prior to increase and enter to the SS (see Figure 3.3.1). This decrease, distinct from short-term dips, coincides with a sudden increase in the disk normalization parameter, suggesting significant changes in the accretion disk structure.

In Figure 3.4.1 we present a comparison of the disk normalization during the outbursts of MAXI J1803-298 and the canonical, intermediate-inclination BHXRB GX 339-4. This figure shows all SIMS and SS of MAXI J1803 data while GX 339-4 data shows the IS and SS, the transition and the beginning of the SS to see differences in the SIMS to SS. GX 339-4 shows a steady decline in disk normalization as it transitions from the HS to SS, indicating that the inner disk is moving closer to the innermost stable circular orbit (ISCO). In contrast, MAXI J1803-298 exhibits a large increase in disk normalization just before entering the SS. This finding suggests that the inner disk is self-obscured, being responsible of the decrease in temperature of the disk and the increase in disk normalization. Given that we don't have a precise mass or distance to the system, we estimate the peak flux of MAXI J1803 assuming that the faint SS to HS transition occurs at a commonly-seen $\sim 2\% L_{\rm Edd}$. From comparing the ratio of the unabsorbed model fluxes between the peak (*observed*) flux and the transition point, the peak luminosity is inferred to be $\sim 69\% L_{Edd}$. However, if our interpretation of self-obscuration is correct, the true peak luminosity is likely somewhat higher than this, occurring at a point where the observed flux was diminished owing to the obscuration.

The phenomenon of self-obscuration in the inner regions of accretion disks around black holes has been predominantly explored through theoretical studies and simulations (e.g., Li et al. 2010; Wang et al. 2014). In systems with sufficiently high inclination, the inner disk puffing up at high accretion rates can lead to observable consequences. Notably, this increase in vertical thickness can lead to partial obscuration of the innermost disk.

Figure 3.3.1 illustrates the time evolution of various aspects of the outburst, including count rate, flux, hardness ratio, and the equivalent widths of Fe XXV and Fe XXVI. When the source transitions into the SS, the disk temperature typically increases and then slowly declines along the SS. However, we observe a sudden temperature drop by a factor of ~ 2 during the SIMS, followed by a temperature increase as the system settles into the vanilla SS. This temperature evolution may indicate the onset of self-obscuration as the disk thickens with growing

$$\dot{M}$$

and blocks the thermal emission from the innermost regions.

Further investigation is required to fully understand the effects of self-obscuration in accretion disks in high inclined systems. Applying the models derived from Li et al. (2010) and Wang et al. (2014), may provide deeper insights. The expected geometry of a thin disk in the soft state contrasts with the puffed-up structure observed in a "slim disk" (Abramowicz et al. 1988; Sadowski 2011; Yorgancioglu et al. 2023; Cao et al. 2024). In such a disk, the scale-height is inflated by radiation pressure and at sufficiently-high luminosity the accretion can become less radiatively efficient. In the case of MAXI J1803, we suggest a flared scale-height in the inner disk produces self-obscuration of the innermost X-ray emitting region.

To assess the prospect of self-obscuration, we analyzed the transition from the HS to SS in GX 339-4 during its 2018 outburst and compared the results with those from MAXI J1803-298. In the SIMS, both systems display typical HS-SS characteristics, including moderate to high disk temperatures, intermediate disk normalization values between the hard and soft states, high accretion rates, and a scattered fraction marginally above 0.25.

The disk normalization scales approximately as $f_h^{-4} R^2$ where f_h is a hardening factor (e.g., Shimura & Takahara 1995) and R is the disk inner radius (Zimmerman et al. 2005b). Because

f_h changes as a function of the disk temperature, one expects a plot of normalization vs kT to exhibit a single track at a fixed radius. Instead, we see that MAXI J1803 shows two tracks, a lower one in the SS, and one which departs to larger normalization (larger apparent R) in the SIMS ((see Figure 3.4.1)). Notably, at $kT_{\rm disk} \approx 0.5 - 0.6$ keV, the SIMS normalization is very significantly larger, approximately 4-times that of the SS. This trend persists across several days during the SIMS, and is consistent with what one would expect for obscuration just onsetting. Self-obscuration provides a natural explanation for the normalization-temperature trend, and the unusual dip in temperature and flux, and the confluence of these events near the outburst's peak.

Alternatively, strong winds or outflows along the line of sight can scatter emission into other sight-lines or preferentially absorb disk photons if a wind or corona is radially structured, which could have the effect of altering the apparent temperature and normalization of the disk emission compared to the intrinsic values. Also, as the state evolves, the accretion energy may be released differently, e.g., with more energy diverted into the corona, winds, or jets instead of being dissipated in the disk (e.g., Neilsen & Lee 2009b), which could affect the observed spectrum.

3.4 Discussion

3.4.1 Source States

The state transitions observed with *NICER* align with the spectral analysis of MAXI/GSC and Swift/BAT observations reported by Shidatsu et al. (2022). In their study, the power-law photon index Γ in the HS was found to be approximately $\sim$ 1.7, increasing to $\sim$ 2.5 as the source transitioned into the SIMS. Upon entering the SS, Γ decreased slightly to $\sim$ 2.1.

In our analysis, we observe similar values for Γ during both the SIMS and SS. This behavior is further supported by the observed scattered fraction, which is consistent with typical values for these states: $f_{sc} > 0.25$ in the HS and $f_{sc} < 0.1$ in the SS (e.g. Done et al. 2007; Belloni et al. 2011). The disk temperature decreases gradually throughout the SS, but first exhibits an atypical pronounced dip in the SIMS. We attribute this effect to self-obscuration of the accretion disk.

3.4.2 Iron Lines

The presence of the Fe XXV and Fe XXVI absorption lines in the SS is indicative of disk winds. In the SS we see an evolution in the strength of the Fe XXVI relative to the Fe XXV line, associated with the cooling of the disk as it is less ionized compared to the beginning of the SS. This is consistent with the expectation for a constant distance from the X-ray source to the observing gas with declining luminosity. In future studies of XRB outbursts, *XRISM* will be able to observe other iron line species.

Zhang et al. (2024) also explored the winds of MAXI J1803 using much of the same *NICER* data than we do in this paper. They used a grouping of observations into 10 epochs, spanning the HS, SIMS, and SS of MAXI J1803 with *NICER* and primarily aimed to assess the evolution of disk winds. Similar to our analysis with `zxipcf`, they used `XSTAR` to fit the wind properties and to search for velocity shifts, particularly in the SIMS and the bright SS. In their analysis, they found that over the 10 epochs of study, Fe XXVI is very strong at the beginning and throughout the SS epochs of study observed an increase of strength of Fe XXV, according to an accretion disk cooling down while the luminosity decreases.

`zxipcf` is appropriate for a power law spectrum with photon index 2, which might effect the column densities and ionization parameters. Nevertheless, our fits to the wind properties broadly match their findings, e.g., the wind column density, ionization and wind evolution in which we observed strong presence of Fe XXVI at the beginning of the SIMS and SS to similar presence

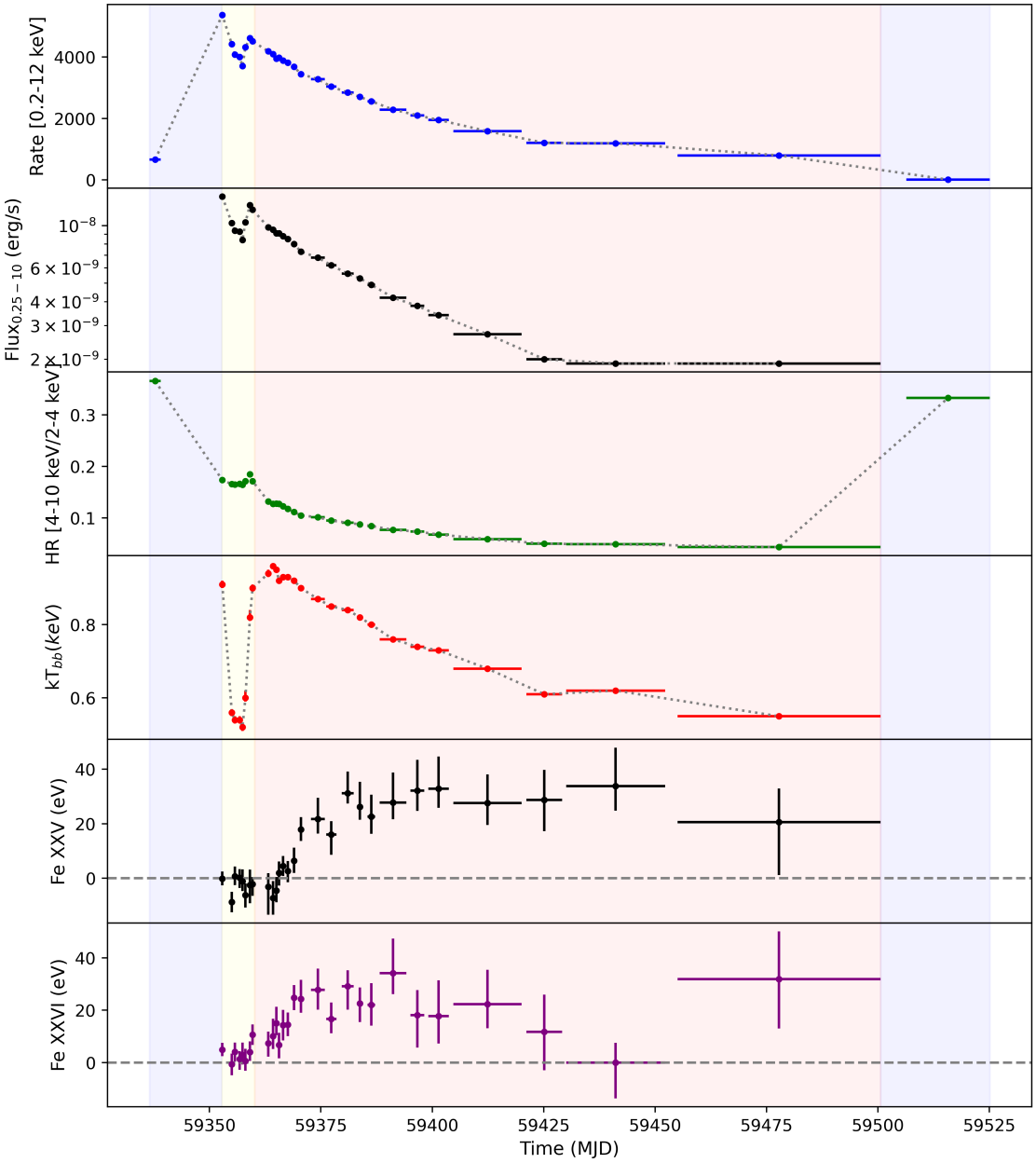

Figure 3.3.1: The count rate, flux, disk temperature, hardness ratio, and the equivalent widths of Fe XXV and Fe XXVI throughout the SIMS and SS phases. The HS is shown for both the count rate and hardness ratio. The blue-shaded regions represent the HS, the yellow region represents the SIMS, and the red region corresponds to the SS. Note the dramatic days-long drop in the disk temperature during the SIMS with a corresponding drop in the count rate. This behavior is suggestive of disk self obscuration.

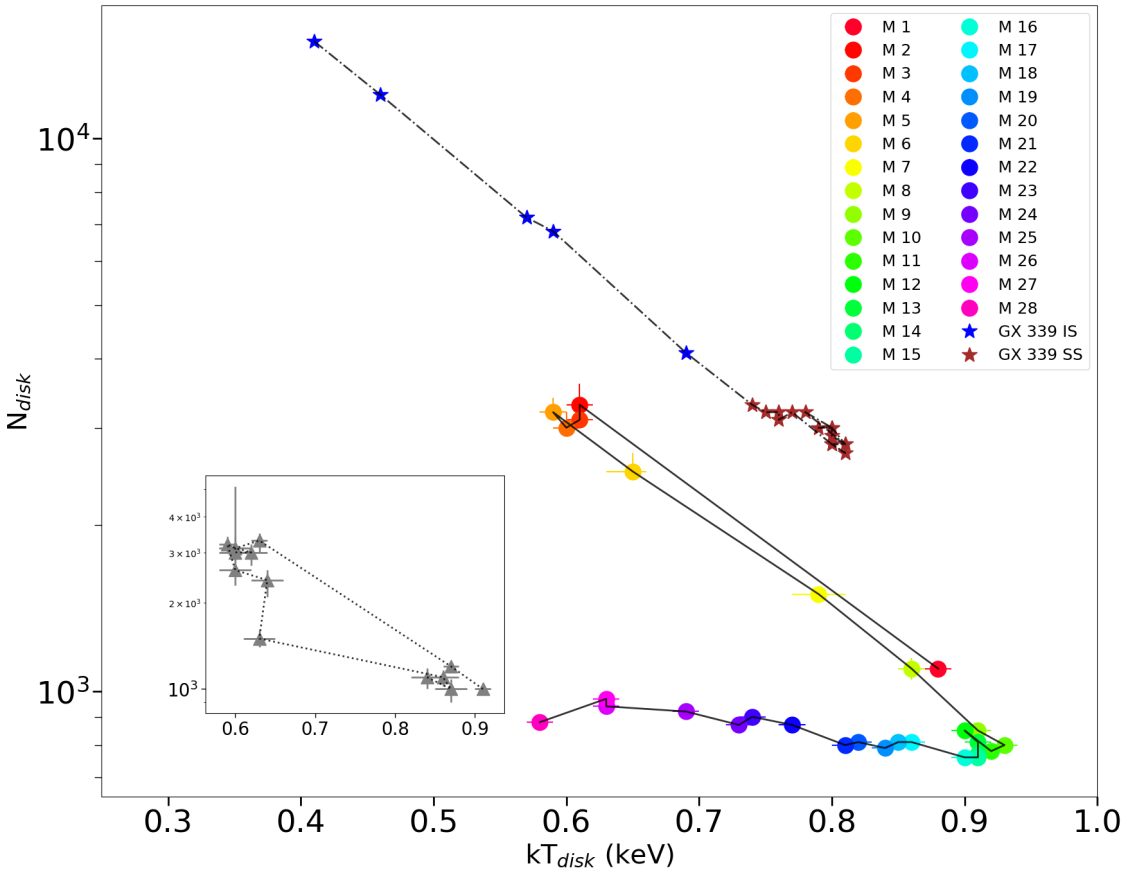

Figure 3.4.1: This plot presents the disk normalization as a function of disk temperature. The color-coded data points correspond to the SIMS and SS of MAXI J1803-298, with blue stars the intermediate states (HIMS and SIMS), and brown for the SS of GX 339-4. Data points from GX 339-4 are included for comparison. The inset shows M1 to M8 unmerged spectra. The plot shows the evolution of disk normalization during the outburst, with a notable short-lived jump in normalization during the SIMS.

of Fe XXVI and Fe XXV over the SS, we obtain is quite similar. We obtain similar velocities within uncertainties but consider them not significant. Complementary to the analysis of Zhang et al. (2024), in Table 3.3.1, we present the evolving equivalent widths of Fe XXV and Fe XXVI features, and our analysis extends to SS luminosities which are a factor of 1.3 below what they analyze in their work (36 days further in time).

3.4.3 Self-obscured Disk

We report the detection of a simultaneous drop in temperature and drop in count rate as the source transitions from the HS to the SS during the SIMS. We interpret these data as a self-obscured disk. In systems with sufficiently high inclination angles, a "puffed-up" disk can partially obscure the inner regions. Here, the inner accretion disk is inflated due to radiation pressure at high $\dot{M}$. This results in partial obscuration of the inner disk's thermal emission, causing an apparent drop in disk temperature and flux. Once the $\dot{M}$ decreases, the scale-height drops and obscuration diminishes, causing the temperature to rise and the observed flux to increase.

As shown in Fig. 3.4.1, a decrease in disk temperature is accompanied by an increase in disk normalization just before stabilizing at lower values as the system enters the SS. This evolution

rules out the possibility of significant mass ejection from the companion star obscuring the disk, and disfavors unexpected disk truncation. A disk wind obscuring the disk is also disfavored as there is no detection of absorption lines in the SIMS.

3.5 Conclusions

We conducted a spectroscopic analysis of *NICER* data from the black hole candidate MAXI J1803, investigating the evolution of disk temperature and iron absorption lines Fe XXV and Fe XXVI throughout the outburst. From our analysis of the SIMS and SS, we identify the following key findings:

1. The observed increase in disk normalization and drop in temperature during the SIMS can most readily be attributed to the presence of a self-obscured slim disk, characterized by a high inclination angle. The observed obscuration, which has not been reported in other sources, suggests that MAXI J1803 may be at extremely high inclination ($\gtrsim 75°$). In the event of a new outburst, a polarimetric measurement could be used to check the inclination, as a high polarization degree is expected for high inclination sources.

2. The obscuration is seen on a timescale of days compared to dip timescales which are the order of minutes.

3. The SIMS exhibits a photon index (Γ) and the fraction of Comptonized seed photons typical of a SIMS, alongside a disk temperature consistent with that of a SS.

4. The detected Fe XXV and Fe XXVI absorption lines are indicative of disk winds at a constant launch radius with evolving ionization state ξ.

5. The wind is estimated to be located $\sim 10^5\ R_g$.

Chapter 4

GRS 1716-249 Spin Measurement with New Dynamical Data

Content of this chapter

This chapter presents the results of the analysis of *Swift* and *NuSTAR* observations of GRS 1716-249 using the continuum-fitting method. Newly obtained dynamical data from optical telescopes have been incorporated to constrain the black hole spin. To achieve this, I performed a Monte Carlo sampling to explore the parameter space and derive a robust spin estimate. These results will be submitted to the *Astrophysical Journal Letters* after completion of this thesis. For this project, I am responsible for the full data reduction, analysis, and manuscript preparation.

GRS 1716-249 is a black hole X-ray binary that underwent an outburst in 2016-2017. I analyzed one soft epoch using joint observations from both telescopes, focusing on constraining the accretion disk properties and the black hole's fundamental parameters.

4.1 Introduction

A common approach to constraining spin involves fitting the thermal X-ray emission from the disk using models such as `kerrbb` (Li et al. 2005) and `kerrbb2` (Davis et al. 2005; McClintock et al. 2006). These models assume that the disk structure and emission properties are well described by the Novikov & Thorne (1973b) and Page & Thorne (1974), considering the full relativistic effects.

In theory, millions of stellar-mass BHs are within the Milky Way (Brown & Bethe 1994) but few of them have dynamical data available (Remillard & McClintock 2006; Özel et al. 2010; Corral-Santana et al. 2016). GRS 1716-249 (hereafter GRS 1716) was discovered in 1993 by the Granat/SIGMA telescopes using the SIGMA coded-mask X-ray and gamma-ray telescope (Ballet et al. 1993; Harmon & Paciesas 1993). GRS 1716 is a low mass X-ray binary (LMXB), with a main sequence companion star of spectral type K (della Valle et al. 1994; Masetti et al. 1996). Since its discovery, GRS 1716 remained in quiescence for 23 years until December 18, 2016, when the MAXI/GSC telescopes detected another outburst (Negoro et al. 2016). This outburst was largely "stalled" outburst unlike the first. Throughout the outburst, during the hard intermediate state (HIMS), it is believed that the disk was close to the ISCO (Bassi et al. 2019). The spectrum during this state showed a power-law component from the corona, andreflection features like the Fe-Kα emission line (~6.5 keV) and the Compton hump (~20 keV). The scenario to measure the spin via continuum fitting and relativistic reflection is during the SIMS. However, this HIMS scenario is also a good place to test the continuum fitting and reflection fitting methods to constrain the spin of the BH.

Until recently, the distance to GRS 1716 has not been well constrained. della Valle et al. (1994) estimated the distance to be in the range of (2.2–2.8) kpc. Later, Masetti et al. (1996) derived a BH mass of 4.9 $M_\odot$, an orbital period of ~14.7 hr, and a distance of 2.4 ± 0.4 kpc. The first attempt to constrain the BH spin via continuum fitting was carried out by Tao et al. (2019), who assumed a fixed distance of 2.4 kpc and obtained a lower limit of $a_\star > 0.92$, an inclination of $i \sim 40$–$50°$, and constrained the BH mass to be $M_{\rm BH} < 8M_\odot$. However, Saikia et al. (2022) suggested that the distance had been underestimated, proposing an estimate to be in the range of 4–17 kpc, with optical/X-ray correlations favoring a most likely value of 4–8 kpc.

The most recent dynamical measurements of GRS 1716 were reported by Casares et al. (2023), who determined an orbital period of 6.7 hr. By utilizing the relation between orbital period and r-band magnitude, they derived a distance of 6.9 ± 1.1 kpc through photometric and spectroscopic measurements. This result is consistent with the estimate of Saikia et al. (2022). Additionally, Casares et al. (2023) measured an orbital inclination, with constraints of $(68 \pm 6)°$ and $72^{+4}_{-5}°$ from the ellipsoidal light curve. Adopting a more conservative range of $(61 \pm 15)°$, they obtain a BH mass of $6.4^{+3.2}_{-2.0} M_\odot$.

GRS 1716 underwent a bright X-ray outburst in 2016–2017, displaying a characteristic evolution through spectral states typical of BH transients. Initially detected in a HS, the source followed a standard outburst track, transitioning through the HIMS and SIMS before reaching the SS. However, what set this outburst apart was the limited duration of the SS, with the system quickly returning to a harder spectrum. This behavior is reminiscent of other BH transients with failed or incomplete state transitions. The data used for spin fitting were obtained during a specific low-luminosity phase of the HIMS, just before the final transition back to the HS. This particular dataset is notable for its exceptional spectral softness, with a disk-dominated spectrum and minimal contribution from the Comptonized component. Such conditions make it an ideal case for applying the continuum-fitting method to constrain the BH spin, as the inner disk radius remains stable and can be reliably linked to the BHs event horizon properties. The reduced influence of the high-energy tail in the spectrum ensures that the thermal disk component can be well modeled without significant contamination from non-thermal emission, thus providing a robust measurement of the inner disk radius. Tao et al. (2019) measured the spin of GRS 1716 using both the continuum-fitting method (`kerrbb`) and relativistic reflection modeling (`relxill`), based on joint *NuSTAR* and *Swift* observations during the HIMS. They adopted a distance of 2.4 ± 0.4 kpc, as reported by della Valle et al. (1994), and considered three fixed BH masses (5, 10, and 15 $M_\odot$) for their analysis. The inclination and spin were constrained to be within 40°–50° and $a_\star > 0.92$, respectively. Additionally, they explored the possible black BH range, identifying a most probable value of (4.9–8) $M_\odot$. A more recent spin measurement using updated dynamical constraints from Casares et al. (2023) was conducted by Zhao et al. (2024). In this study, they adopted a distance of 6.9 kpc and a black BH of 6.4 $M_\odot$. Unlike Tao et al. (2019), they allowed the inclination to vary as a free parameter in both the continuum-fitting and relativistic reflection models, obtaining a similar inclination range. However, their spin measurement yielded a significantly lower upper limit of $a_\star < 0.78$.

In this project we compare both spin measurements via continuum fitting and relativistic reflection modeling from Tao et al. (2019) and Zhao et al. (2024) with our continuum fitting analysis with the new dynamical data, in which we fix the BH mass, inclination and distance with `kerrbb2` model.

Due to the nature of the continuum fitting method, different input values of distance and disk inclination may alter the result of the spin estimation. In our analysis we considered the three different inclinations given by Casares et al. (2023). A Monte Carlo (MC) sampling of the different new dynamical parameters was used to constrain the spin of GRS 1716. We employed *NuSTAR* and *Swift* observations to make a joint fit to constrain the spin, and compare our results with the

Table 4.2.1: Joint observations of *NuSTAR* and *Swift*

Mission	ObsID	Start time	End Time	Exposure (ks)	Count rate (counts s^{-1})
NuSTAR	90301007002	2017-07-28 12:06:09	2017-07-30 23:21:09	89.6	92.7
Swift/XRT	00088233001	2017-07-28 16:51:27	2017-07-28 20:34:56	3.7	93.9

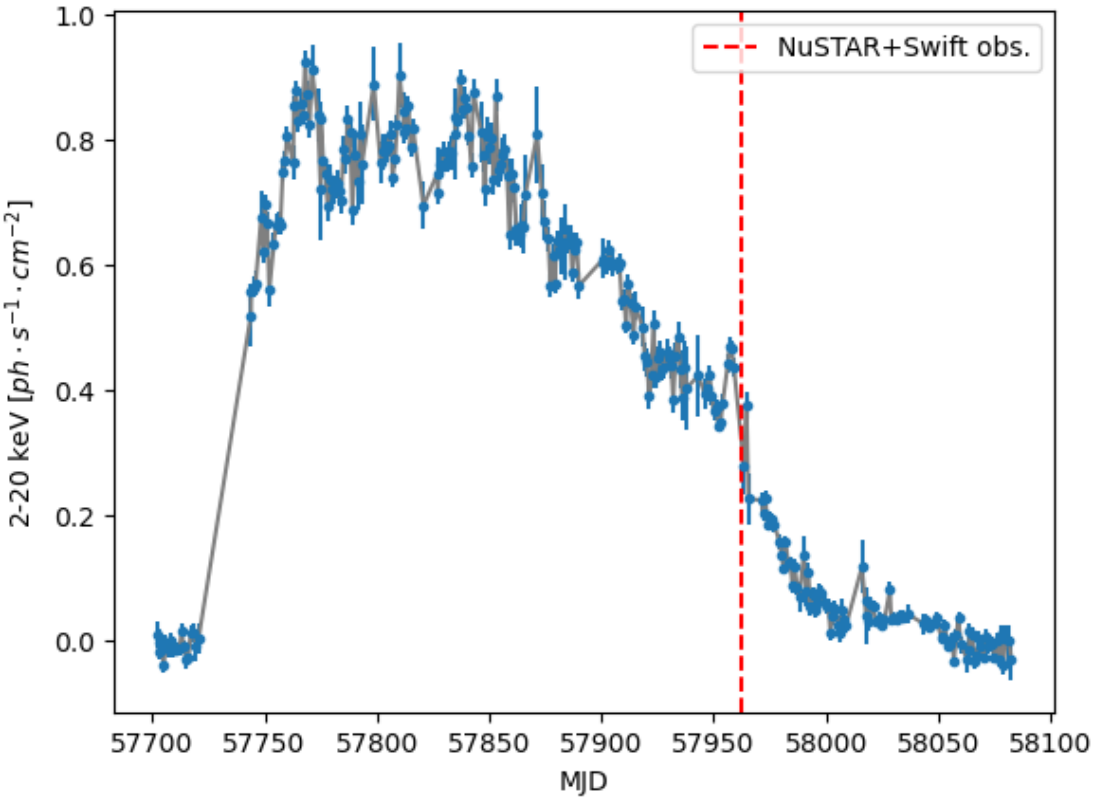

Figure 4.2.1: This plot presents the *MAXI* light curve of the full outburst of GRS 1716 in 2016-2017 from 2 to 20 keV range. The vertical dashed line (red) indicates the starting time when *NuSTAR* and *Swift* observed.

reflection fitting method (Zhao et al. 2024) on the 2016 outburst. In Section 4.2, we will describe the observations and data reduction. Section 4.3 will present the MC sampling, spectral fitting and results. The results will be discussed in Section 4.4 and summarized in Section 4.5.

4.2 Observations and Data Reduction

In this study, we analyzed *NuSTAR* and *Swift* data during the hard-intermediate state (HIMS) in the transition back to the HS of the outburst. Unlike typical HIMS observations, this dataset exhibits an unusually soft spectrum, making it uniquely suitable for studying disk properties and reflection components, or soft excess. Based on the spectral classification, we selected one *NuSTAR* observation (`nu90301007002`) and one *Swift* observation (`00088233001`) taken during the HIMS, with exposure times of 89.2 ks for `FPMA`, 89.9 ks for `FPMB`, and 3.7 ks for *Swift*, respectively (see Table 4.2.1). The *MAXI* light curve in Figure 4.2.1 marks the epochs of the *NuSTAR* and *Swift* observations as the source transitions back to the HS.

4.2.1 *NuSTAR*

NuSTAR (Harrison et al. 2013) is the first hard X-ray focusing observatory launched by NASA. It consists of two identical focusing modules: FPMA and FPMB. The cleaned *NuSTAR* event files were processed using the `NuSTARDAS` pipeline 1.9.2, with the *NuSTAR* CALDB version 20200429. The GRS 1716 spectrum was extracted for both FPMA and FPMB detectors from a 100″ radius circle centered on the source, while the background spectra were extracted from a source-free circle of 200" on the same detector chip. Data are analyzed from 3-75 keV for each FPM.

4.2.2 *Swift*

The *Swift* observatory is a multi-wavelength facility with the capacity to observe from ultraviolet/optical wavelengths (UVOT) to X-rays (XRT) and γ-rays (BAT). For our analysis we only used the XRT data (Burrows et al. 2005) in the range of 0.3-10 keV.

During the 2016–2017 outburst of GRS 1716, *Swift* observed the source at five epochs, three of which overlapped (either simultaneously or quasi-simultaneously) with *NuSTAR* during the HIMS. However, these three observations occurred while the source was transitioning from the SS to HIMS before re-entering the SS. For this study, we focus on the final overlapping epoch, which captures the low-luminosity HIMS just before the transition back to the HS and eventual quiescence. Zhao et al. (2024) used five *Swift*/XRT observations of GRS 1716, jointly with *NuSTAR* in two epochs where a HIMS was detected. The observation was carried out in windowed-timing (WT) mode. We extracted cleaned event files with the FTOOLS task `xrtpipeline` version 0.13.7 and calibration (CALDB) file version x20230725. We chose a box region of length and width of 95"×90" for source and 180″ × 90″ for the background. Light curve, source, and background spectra were extracted using XSELECT version 2.5b.

4.3 Analysis & Results

We performed spectral fitting using the XSPEC v12.13.0c software package (Arnaud 1996). To properly constrain the spin parameter via the continuum-fitting method, we conducted a Monte Carlo sampling of the dynamical data (M, i, and D). This sampling is essential for capturing the measurement uncertainties in mass, inclination, and distance, which directly impact the spin constraints. To efficiently perform multiple spectral fits, we utilized the XSPEC python module PyXSPEC to automate the process. As shown in Figure 4.3.1, a prominent Fe-Kα emission line and a strong Compton hump are evident in *NuSTAR*, necessitating a model that accurately accounts for these reflection features. We will discuss our results and compare with reflection-based and other recent spin measurements of GRS 1716 (Tao et al. 2019; Zhao et al. 2024) in Section 4.4.

4.3.1 Monte Carlo Sampling

To robustly constrain the black hole spin parameter via the continuum-fitting method, we first performed a Monte Carlo (MC) sampling of the dynamical parameters reported in Casares et al. (2023). This MC sampling, which consisted of 1000 realizations, was carried out by drawing random values for the three distributions of inclination angle , distance, and mass function according to their respective uncertainties, while the mass ratio was sampled from a normal distribution. These sampled parameters were then used to derive the probability distributions of the BH mass $M_{\rm BH}$ and the companion star mass $M_{\odot}$ using the mass function:

$$f(M) = \frac{M_1 \sin^3 i}{(1+q)^2} = \frac{K^3 P_{\rm orb}}{2\pi G}, \tag{4.1}$$

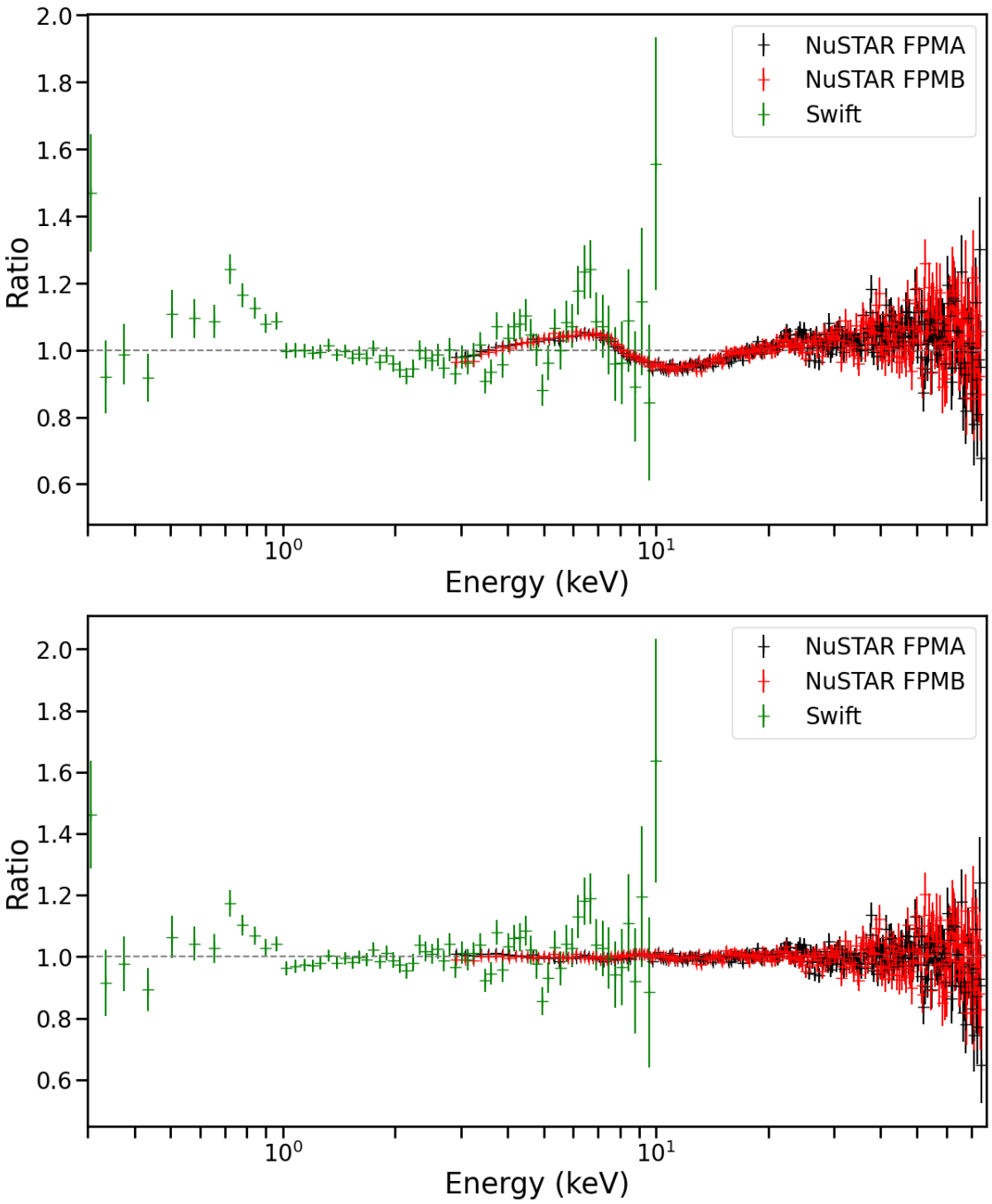

Figure 4.3.1: *Top*: Ratio plot for the *NuSTAR* and *Swift* observations, with spectra fitted in the 3–75keV and 0.3–10keV bands, respectively. Both FPMA and FPMB data are shown. The fit uses a simple model ($crabcor \cdot TBabs(simpl(diskbb \cdot kerrbb2)$) that does not account for key spectral features, including the strong iron line emission at 6.5keV and the Compton hump around 50keV. *Bottom*: Ratio plot for the *NuSTAR* and *Swift* observations, accounting for the iron line emission and the Compton hump, improving the fit ($smedge \cdot crabcor \cdot TBabs(simpl(diskbb \cdot kerrbb2))$).

where $q = M_2/M_1$, K is the radial velocity semi-amplitude, $P_{\rm orb}$ is the orbital period, and G is the gravitational constant.

The sampled parameters are then incorporated into the spectral fitting using the continuum-fitting method, where each realization of the three parameters is fixed during the fitting procedure to ascertain out the resulting impact on spin. This systematic approach ensures that the uncertainties in the dynamical parameters are properly accounted for, leading to a reliable constraint on the BH spin.

4.3.2 Continuum Fitting

We first performed a preliminary, exploratory fit using the new dynamical constraints from Casares et al. (2023) via continuum fitting. The full model used in this initial fit, prior to applying it in PyXSPEC for the 1000 fits, was: `smedge·crabcor·TBabs(simplcut·kerrbb2)`. The components of this model are as follows: `smedge` (Ebisawa et al. 1994) accounts for the reflected component, assuming that the disk elastically scatters all incident Compton photons, except for a broad iron absorption edge, which is modeled phenomenologically (Ebisawa et al. 1994). `Crabcor` (Steiner et al. 2010) standardizes the calibration to a common brightness and shape for the Crab between *NuSTAR* FPMs and *Swift*. `TBabs` models Galactic neutral hydrogen absorption (Wilms et al. 2000). For Comptonization, we use `simplcut`, a model that applies Comptonization to an arbitrary seed spectrum—here, the disk emission (Steiner et al. 2009; Steiner et al. 2017; Steiner et al. 2017). The thermal radiation originates from the accretion disk. `Kerrbb2` (McClintock et al. 2006) is a fully relativistic thin-disk model, incorporating the effects of returning radiation and limb darkening. This model utilizes look-up tables for the spectral hardening factor f, computed using `bhspec` (Davis et al. 2005; Davis & Hubeny 2006) and `kerrbb` (Li et al. 2005). It includes two viscosity parameter options, $\alpha = 0.1$ and $\alpha = 0.01$, both of which were explored in this study. The `kerrbb2` model fits only the dimensionless spin parameter ($a_\star$) and the mass accretion rate ($\dot{M}$).

The Monte Carlo (MC) samples were used in PyXSPEC to fit 1000 permutations generated from the MC process. Across all fits, the source exhibits a spectral index ($\Gamma \sim 1.9$) and a scattered fraction ($f_{sc} < 0.4$), consistent with expectations for a HIMS. The corona temperature was not reliably constrained, and it was fixed at 100 keV, as this resulted in an improved fit.

In the `kerrbb2` model, the BH mass, inclination, and distance serve as key parameters that anchor the spin value in each fit, directly linking it to the `diskbb/ezdiskbb` $R_{\rm in}/M$. This model accounts for relativistic effects, spectral hardening, and self-irradiation of the disk, providing a more physically accurate determination of the inner disk radius and, consequently, the BH spin (e.g., Li et al. 2005; McClintock et al. 2006; Steiner et al. 2010). The spin is not tightly constrained and for each of the three candidate inclination distributions, our findings are consistent with a spin of 0, but incompatible with high spin > 0.2.

Figure 4.3.2 illustrates the associated spin distribution of each dynamical distribution, and for both α possibilities (0.1 and 0.01). The inclination values reported in Casares et al. (2023), derived from the ellipsoidal light curve, did not provide strong constraints on the spin. Using a conservative inclination of $61 \pm 15^\circ$, the spin results remain weakly constrained, but they suggest that a prograde spin—where the BHs spin aligns with the orbital motion of the accreting material—is favored. However, the data also remain consistent with retrograde spin configurations, where the spin is opposite to the orbital motion. As shown in Figure 4.3.2, the results for both configurations are quite similar, with no strong preference for either. Additionally, the choice of $\alpha = 0.1$ does not drastically improve the constraints on spin, though it does marginally refine the results. Importantly, the weak constraints on the spin, consistent with values near zero, are reasonable and do not suggest extreme spin values ($a_* > 1$ or $a_* < -1$). While a high spin is strongly disfavored,

the current data do not decisively favor one spin configuration over the other.

4.4 Discussion

In this study, we performed a joint spectral fitting of the simultaneous and quasi-simultaneous *NuSTAR* and *Swift* observations of GRS 1716 during the HIMS of its 2016–2017 outburst. In this state, the accretion disk extends close to or reaches the ISCO, with a visible reflection component in the data. We analyzed the results from 1000 MC samples apiece using several dynamical distributions obtained from those reported by Casares et al. (2023). Using the mass, distance, and inclination constraints obtained, via the continuum-fitting method, we couldn't constrain the BH spin. In Figure 4.4.1, we present the spin distribution as a result of the MC sampling of the different optical parameters from Casares et al. (2023). The three inclinations used, show a non-preferential distribution of the spin for $\alpha = 0.1$ and $\alpha = 0.01$, although the conservative value of $61 \pm 15^{\circ}$ shows a hint prograde spin values. The distribution of mass, inclination and distance of the MC output are according the errors reported in Casares et al. (2023).

Comparing our results with the spin measurements of Tao et al. (2019) and Zhao et al. (2024), where they found a high BH spin of $a_\star > 0.92$ and $a_\star < 0.78$, respectively. In Tao et al. (2019) and Zhao et al. (2024) cases, they used `kerrbb` for the relativistic disk model and `relxill` for the reflection component. The `Kerrbb2` model is an improved version of `kerrbb`, offering more accurate representations of accretion disk emission, particularly in high-luminosity systems. One of the key advantages of `kerrbb2` is its inclusion of *self-irradiation*, which accounts for the radiation emitted by the inner disk that heats the outer regions, leading to a more accurate treatment of disk emission, especially at higher luminosities. Additionally, `Kerrbb2` allows for a variable *spectral hardening factor* ($f \sim 1.4 - 1.5$), providing a better fit for disks with varying temperatures. The model also incorporates a more realistic treatment of the *inner disk radius*, considering both the BH spin and mass, as well as the inclination of the disk, which results in improved constraints on parameters like spin and inner disk radius. In contrast, `kerrbb` assumes a constant hardening factor and a simpler model for the inner disk radius, which can limit its accuracy in systems with significant relativistic effects or self-irradiation. While `kerrbb2` is slightly more computationally complex due to its additional parameters, it provides more physically accurate results, making it ideal for systems with strong relativistic disk emission, such as high-spin BH or highly inclined systems. `kerrbb` remains a useful, faster option for systems where these effects are less pronounced or for more straightforward analyses. They found a most probable inclination between 40-50° with `relxill`, linking the `kerrbb` inclination to `relxill`. The discrepancy between the inclination measured from optical studies and the inclination inferred from the `relxill` model, as reported by Tao et al. (2019) and Zhao et al. (2024), results in significantly different spin estimates and may be subject to systematic uncertainties. Similar challenges have been observed in other BH binaries, such as Cygnus X-1 and GX 339-4, where inclination estimates derived from relativistic reflection modeling have varied across different studies. For instance, in Cygnus X-1, Walton et al. (2016) analyzed *NuSTAR* data in the HS and demonstrated that the inferred inclination was highly sensitive to model parameters and assumptions. Likewise, García et al. (2015) investigated multiple *RXTE* spectra of GX 339-4 and found that the inferred inclination varied depending on the spectral model and data selection, highlighting the potential for systematic uncertainties in reflection-based measurements. These findings suggest that inclination estimates obtained through reflection modeling should be interpreted cautiously, as they can be influenced by modeling choices, data quality, and the complex physical environment of the system. Given that our spin estimates are derived via continuum fitting, the differences between our results and those reported in previous studies may arise from several factors. Notably, our continuum fitting analysis of GRS 1716 reveals an inverse correlation between inclination and spin: assuming inclinations of 40°, 45°, and

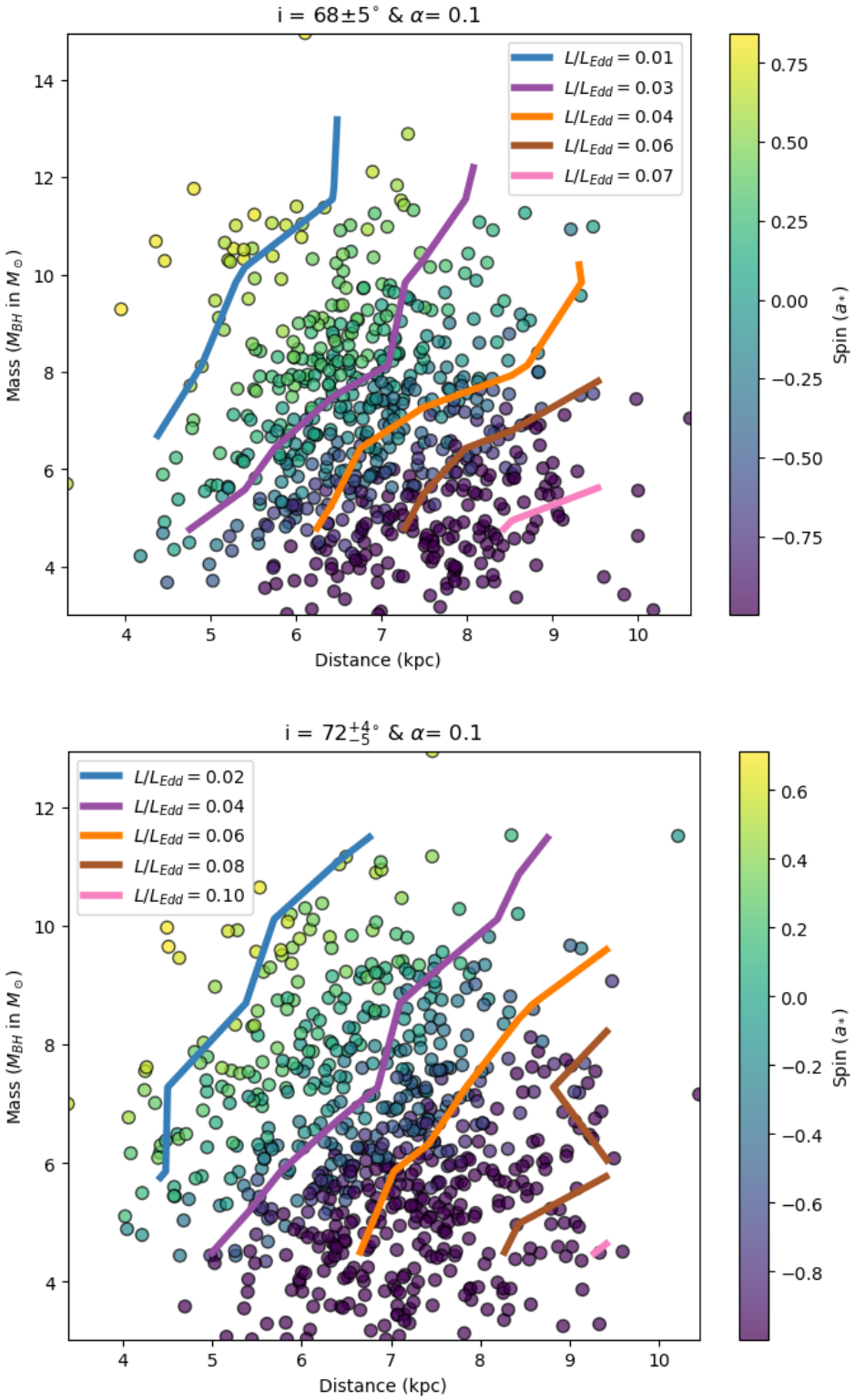

Figure 4.3.2: The distribution of BH mass ($M_{\odot}$) as a function of distance (kpc) is shown, with spin indicated by a color map for the $\alpha = 0.1$ case. The overlaid contours represent the Eddington luminosity ratio, interpolated from the spectral fits. Lower luminosities correspond to higher spin values, particularly for both inclinations, with higher black hole masses and smaller distances.

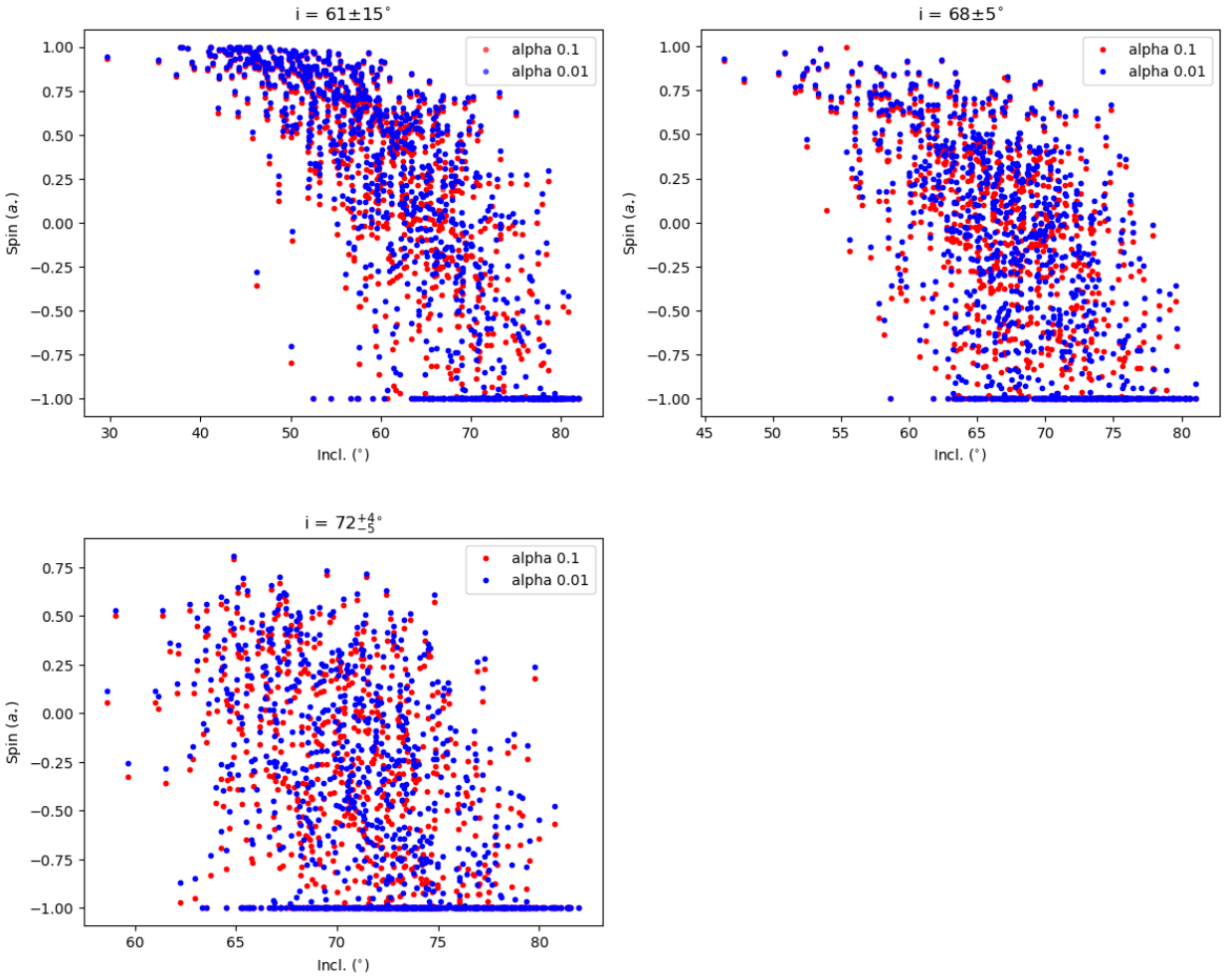

Figure 4.4.1: The plots show the spin distribution as a function of the inclination. Each plot shows the spin distribution for $\alpha = 0.1$ (red) and $\alpha = 0.01$ (blue) respectively. The inclination distributed is within the errors reported in Casares et al. (2023).

50° results in spin values of $a_\star = 0.61$, $a_\star = 0.50$, and $a_\star = 0.36$, respectively. Additionally, the corresponding Eddington luminosities increase slightly, from $L_{\rm Edd} \sim 0.02$ to $L_{\rm Edd} \sim 0.023$. This trend suggests that higher inferred spin values are associated with lower inclinations and lower luminosities, underscoring the importance of accurately constraining inclination when determining spin via continuum fitting.

The inclination of BHXRBs can be estimated through both X-ray and optical observations, but these method occasionally yield incompatible values, sometimes differing by more than 10° (Connors et al. 2019; Poutanen et al. 2022). This discrepancy it may arise due to different physical processes being probed, or it may arise due to modeling error. The reflection inclination is determined from spectral modeling of the X-ray reflection signatures from the inner accretion disk. Reflection spectroscopy, which analyzes the broad and skewed Fe Kα line produced by X-ray reflection, is highly sensitive to inclination, with higher values resulting in stronger Doppler shifts and boosting. The continuum-fitting method, which models the thermal emission from the accretion disk (e.g., using `kerrbb2`), is essentially very weak sensitive to inclination, but this can be affected by factors such as disk warping, precession, or spin-orbit misalignment, which also affects the reflection signal as much as it would be the continuum signal. In contrast, optical and IR observations obtained in quiescence constrain the inclination of the binary orbital plane via the ellipsoidal modulation of the secondary star. This is caused by its distorted shape due to the BH's gravitational influence (Gelino et al. 2006; Khargharia et al. 2012).

Several factors may contribute to the inclination discrepancy between these methods. The inner accretion disk may be tilted relative to the binary orbit due to spin-orbit misalignment, possibly caused by natal kicks during BH formation (Salvesen & Pokawanvit 2020) or a tilted disk causing Lense-Thirring precession (see Steiner & McClintock 2012; Steinle & Kesden 2022a). Optical estimates may also be biased if the accretion disk's contribution is not reliably estimated to the observed light (Salvesen & Pokawanvit 2020; Poutanen et al. 2022; Steinle & Kesden 2022b), or if X-ray irradiation of the companion star modifies its ellipsoidal variations. These discrepancies have important implications for determining BH mass and spin, as a lower inclination inferred from X-ray data compared to optical estimates suggests misalignment or warping of the inner disk but a modeling error might be also, a plausible explanation. X-ray polarimetry would be a potential cross-check of spin and inclination in a future outburst. Reconciling these differences is important for understanding these spectral models used to understand accretion disk structure, spin-orbit alignment, and the evolutionary history of BHXRBs.

Spin measurements via continuum fitting, they ideally have been done in the SS, where the thermal emission dominates. In this study, we used data from the HIMS which is outside of the typical place, being an important caveat related to the luminosity of the HIMS (Steiner et al. 2009)

4.5 Conclusions

In this study, we conducted a joint spectral analysis of simultaneous/quasi-simultaneous *NuSTAR* and *Swift* observations of GRS 1716 during the HIMS of its 2016–2017 outburst. By modeling the broadband X-ray spectrum (0.3–75 keV) with the relativistic disk model `kerrbb2` and the reflection model `smedge`, we constrained the BH spin using the continuum-fitting method. Our MC dynamical sampling, incorporating updated dynamical constraints on mass, distance, and inclination, yields a spin distribution consistent with zero. This suggests that, given the revised system parameters, the spin of GRS 1716 cannot be reliably constrained, strongly disfavoring high spin.

Our results disagree with previous spin estimate, such as the high spin ($a_\star > 0.92$) found by Tao et al. (2019) but agree with the more moderate constraint ($a_\star < 0.78$) reported by Zhao et al. (2024). These studies employed the models `kerrbb` and `kerrbb2`, respectively, for the relativistic

disk component and `relxill` for the reflection component, linking the inferred inclination and spin parameters of `kerrbb/kerrbb2` to that derived from `relxill`. Our study, in turn, relies on newly available dynamical constraints from Casares et al. (2023), where the mass, inclination, and distance were fixed, in our continuum fitting, based on MC outputs. Adopting the reasonable assumption that the BH spin is aligned with the binary orbit, this inclination constraint leads to a significantly lower inferred spin.

The discrepancy in spin measurements between this study and Tao et al. (2019) and Zhao et al. (2024) is likely influenced by differences in the assumed system inclination. Exploration on the inclinations reported in Tao et al. (2019) and Zhao et al. (2024) with `relxill` shows spin ($a_\star < 0.75$) for a fixed BH mass of 6.4 $M_\odot$ and a distance of 6.9 kpc adopted from Casares et al. (2023). Optical observations suggest an inclination between 68° and 72°, whereas spectral modeling with `relxill` in previous studies (Tao et al. 2019; Zhao et al. 2024) suggested a lower inclination, highlighting the discrepancy between X-ray and optical inclination measurements.

Chapter 5

Final Remarks

5.1 Summary of Results and Discussion

Using X-ray observations from *NICER*, *Swift*, *NuSTAR*, and *Chandra*, I performed a detailed, self-consistent analysis of MAXI J1813-095 during its failed-transition outburst in 2018. Employing the latest relativistic reflection model, I characterized the disk-corona connection in a self-consistent manner. Across seven observations, joint data from multiple X-ray telescopes revealed that in the HS, the inner accretion disk was in close proximity to the BH, in disagreement with the picture of a truncated disk during the HS. This may suggest that the system was undergoing a state transition, which ultimately failed, leading the source to return back to quiescence. Notably, a broad Fe Kα emission line at 6.5 keV was observed, and inclusion of relativistic reflection was crucial for fitting the spectrum. This analysis not only accounted for the reflection component but also incorporated the Comptonized reflection emission as a direct consequence of the self-consistent approach. This allowed for constraints on the inclination of the accretion disk and disk radius. One common picture of the HS typically presents a heavily truncated disk (around $\sim 100 R_g$), but the case of MAXI J1813-095 reveals a markedly different scenario. In Chapter 2, the discussion explores the possibility of a slightly or non-truncated disk for black hole luminosities $<10\%\ L_{Edd}$, and compares this with a low-luminosity outburst of GX 339-4, which presents similar behavior. This comparison suggests that a heavily truncated disk is unlikely during low-luminosity outbursts, making it necessary that future studies (on other outbursts) test these conclusions. The most stringent constraint on the inner disk is provided by Observation 5, where joint data from *NICER*, *Swift*, and *NuSTAR* were used to constrain its radius. Additionally, another key result of this work is the discovery of a reflection fraction—defined as the portion of Compton-scattered photons reflected by the disk—that is close to unity. This result arises from our self-consistent modeling, in contrast to previous studies on this source, which employed non-self-consistent approaches and reported a much lower reflection fraction of approximately 0.1.

A reflection fraction close to unity is in accordance with Dauser et al. (2016). A self-consistent analysis was necessary to fit the spectrum both with and without the reflection component. A model without reflection characterizes the continuum emission, while the model with reflection accounts for both the continuum and reflected emission independently. Because the reflection component must contribute significantly relative to the continuum, maintaining consistency between the two resulted in a higher reflection fraction. An MCMC of the output, used to study the probability distribution of the results, conferred robustness to the results, enabling a precise constraint of the inner radius and reflection fraction from Observation 5 (see Chapter 2, Table 2.3). Further investigation on future outbursts of MAXI J1813-095 is required, as well as the study of other sources presenting similar conditions to be analyzed self-consistently.

The BHXRB MAXI J1803-298 underwent a full outburst in 2021. Using *NICER* observations of the full outburst, our primary focus on the study of the evolution of disk winds (see Chapter 3), but the most significant finding of this study was the detection of a self-obscured disk in the SIMS, revealing important constraints on the disk structure and its interaction with the outflow. To track disk wind evolution requires a combination of similar observations in order to increase the S/N and correspondingly the sensitivity to line features. The absorption lines are related with disk ejection, absorbing the emission from the inner disk and the corona. These winds are optically thin and highly ionized, and thought to be equatorial. As the absorption lines are narrow (unresolved), stacking contiguous observations helps to enhance the signal. In this work, a proper assessment of disk wind velocity was not possible due to an energy-calibration uncertainty of *NICER*, which is comparable in size to the tentative line shifts of $\lesssim$30 eV found. In this sense, line shifts have been observed, though not significantly exceeding the *NICER* gain calibration uncertainty of $\sim$ 30 eV. An analysis using the `zxipcf` wind model helped to estimate the wind column density and ionization.

The big surprise of finding a self-obscured disk comes from the fact that it is one of the first self-obscured disk detections. The major outburst of MAXI J1803-298 revealed a decrease in disk temperature and an unexpected disk normalization increase that was not caused by disk winds as no absorption lines were detected during self-obscuration. Self-obscured disks are expected to occur near outburst peaks for highly inclined systems as MAXI J1803-298, because the accretion disk puffs-up due to the radiation pressure. The long duration of such a decrease of disk temperature is key to rule out other possibilities like an ejection from the companion star. A typical timescale for ejection is in the range of minutes, but in this case, the disk itself appears to have been obscured for several days, leading to self-obscuration as a natural explanation. Plotting the disk temperature against disk normalization (see Figures 3.3.1 and 3.4.1 in Chapter 3) is the primary evidence for this finding. A proper comparison was made with another BHXRB, namely GX 339-4, during its hard-to-soft state transition in its 2018 outburst. The disk temperature versus disk normalization showed a canonical decrease in disk normalization while the disk temperature increases, ruling out the hypothesis of an ejection or wind obscuration. The normalization changing with temperature has at least a significant role played by the temperature-dependent color-correction factor. So a constant radius should produce tracks that change in both temperature and normalization. A second comparison was made, for exploration purposes, with the BHXRB H1743-322 which underwent many outbursts over several decades. H1743-322 is a highly inclined system, in which we investigated a major outburst, a normal outburst and a failed outburst. In all three cases, we explored the evolution of the disk temperature against disk normalization and only in the major outburst, a similar behavior in temperature versus normalization was found. Also, the light curve showed a similar dip in the SIMS across several days compared to the two other outbursts. The normal outburst and failed outburst showed normal behavior as other low-inclined systems, reinforcing the idea that self-obscuration could be common but specific to major outbursts of high-inclination systems.

Further investigation of other highly inclined BHXRBs can definitively determine whether self-obscuration occurs in major outbursts. Other avenues of research may also shed light here, such as the reflection Fe-Kα emission line being self-obscured or the possibility to develop a new model for self-obscuration.

The third work of this thesis consisted of a new spin measurement of the BHXRB GRS 1716-249. New dynamical data obtained with the Gran Telescopio de Canarias for spectroscopy, the Danish 1.54 m telescope, the Southern Astrophysical Research (SOAR) 4.1 m Telescope and the 4.2 m William Herschel Telescope for photometry, revealed new measurements of the BH mass, inclination and distance. The new observations resulted in two ellipsoidal light curves that led to

two inclination measurements of $(72^{+4}_{-5})^\circ$ and $(68^{+6}_{-6})^\circ$, a distance of (6.9±1.1) kpc and a BH mass of $(6.4^{+3.2}_{-2.0})$ $M_\odot$. However, Casares et al. (2023) adopted the conservative value of (61±15)°. Using joint *NuSTAR* and *Swift* data, we fitted the SS via continuum fitting with `kerrbb2` to obtain a spin measurement. A MC sampling of distributions for inclination, distance, mass function and mass ratio (q) was performed, and in each instance a corresponding BH mass computed. The output of the MC sampling was incorporated into the *NuSTAR* and *Swift* joint data set and fitted again via continuum fitting. The result of this analysis revealed that the spin of GRS 1716-249 is only weakly constrained and is consistent with $a_\star = 0$. Its 95% CL upper limit, however, does not rule out high spin, indicating that a broad range of spin values remains possible. Comparing this result with a previous work on a revised spin of GRS 1716-249 with relativistic reflection modeling revealed a disagreement in spin and inclination of the system. Relativistic reflection modeling obtained a spin around $a_\star = 0.4$ using the same data and an inclination between (40-50)°. Reflection-based inclination measurements have shown tens-of-degrees inconsistency, so one possibility is that the inclination measurement is flawed here; another is that the optical inclination measurement is inaccurate; alternatively, the binary orbital inclination measured in the optical may differ from the inner-disk inclination if the spin axis is inclined, though that is statistically disfavored, especially for low spin (e.g., Steiner et al. 2012b).

To address these questions requires more optical data to ensure reliable inclination constraints and to be able to obtain a tighter constraint on the spin value. Other possibilities to be explored and related with this result would be to study a possible heavy misalignment between the inner disk and the outer disk.

5.2 Future Directions and Broader Impacts

The results obtained in this thesis observed and addressed several key questions in the BHXRB field such as the role of self-obscuration, the reflection fraction, HS inner radius, and the accretion physics governing BHXRBs. New self-consistent analyses with different BHs in their HS in high versus low luminosity outbursts might provide new constraints on whether the inner radius is truncated, slightly truncated or non-truncated. Also, the question of the size of the reflection fraction, can be properly addressed accounting for the Comptonized reflection photons, likely resulting in a reflection fraction close to unity as expected. The HS and intermediate states are the perfect place to find connections between the jet, the corona and the accretion disk, and multi-wavelengths campaigns are crucial for this purpose.

The SIMS and SS are ideal for assessing if self-obscuration may occur or not. Despite being among the first to report a detection of a self-obscured disk, this thesis also outlines methods for its identification, paving the way for future research in this field. A new model is being developed by a collaborator to address how a self-obscured disk behaves in the SIMS, and a study on self-obscured iron emission line has been initiated with collaborators.

Measurements via continuum fitting are one of the most reliable methods for determining the BH spin. The difference reported in Chapter 4 of this thesis raises the question of why spin estimates from continuum fitting and relativistic reflection modeling do not fully agree. Future comparisons of both methods in observations that exhibit iron emission lines will be important for understanding the origin of this difference.

5.3 Final Thoughts

This thesis provides a foundation for future investigation on BH accretion physics, with implications for the different spectral states. As upcoming observational facilities (*XRISM* and *IXPE*) improve

spectral resolution and sensitivity, our understanding of these extreme environments will continue to evolve, refining models of accretion, jet formation, and high-energy feedback processes in compact objects. New findings, such as self-obscuration, clear the path to develop new models, and self-consistent analysis will help us to improve the knowledge of BHXRB physics.

Multi-wavelength and multi-messenger studies will play a crucial role in the upcoming years in the BHXRB field. The latest publication of the LHAASO collaboration (LHAASO Collaboration 2024) reported the detection of ultra-high energy γ-ray emission from BHXRBs, such as GRS 1915+105 or Cygnus X-1, making them candidates for sources of Galactic cosmic rays. In the field of theoretical astrophysics, BHXRBs provide an ideal environment for quantum gravity studies by investigating potential deviations from classical general relativity in strong gravity regimes. These searches focus on spectral deviations, such as shifts in the Fe Kα line or the appearance of anomalous emission lines, as well as possible variations in the gravitational constant (G) across different accretion states, particularly in the SS. Additionally, quantum gravity effects may manifest themselves through energy-dependent photon arrival time delays or deviations from the Kerr solution in relativistic reflection spectra.

Bibliography

Abramowicz, M. A., Czerny, B., Lasota, J. P., & Szuszkiewicz, E. 1988, The Astrophysical Journal, 332, 646, doi: 10.1086/166683

Adegoke, O., Garcia, J., Connors, R., et al. 2024, arXiv e-prints, arXiv:2410.01134, doi: 10.48550/arXiv.2410.01134

Aharonian, F., Akhperjanian, A. G., Bazer-Bachi, A. R., et al. 2006, Astronomy and Astrophysics, 457, 899, doi: 10.1051/0004-6361:20065351

Alabarta, K., Altamirano, D., Méndez, M., et al. 2020, Monthly Notices of the Royal Astronomical Society, 497, 3896, doi: 10.1093/mnras/staa2168

Aleksić, J., Ansoldi, S., Antonelli, L., et al. 2016, Astroparticle Physics, 72, 76–94, doi: 10.1016/j.astropartphys.2015.02.005

Anastasopoulou, K., Zezas, A., Steiner, J. F., & Reig, P. 2022, Monthly Notices of the Royal Astronomical Society, 513, 1400–1413, doi: 10.1093/mnras/stac940

Araudo, A. T., Bosch-Ramon, V., & Romero, G. E. 2011, Transient gamma-ray emission from Cygnus X-3. https://arxiv.org/abs/1104.1730

Armas Padilla, M., Muñoz-Darias, T., Sánchez-Sierras, J., et al. 2019, Monthly Notices of the Royal Astronomical Society, 485, 5235, doi: 10.1093/mnras/stz737

Armas Padilla, M., Muñoz-Darias, T., Sánchez-Sierras, J., et al. 2019, Monthly Notices of the Royal Astronomical Society, 485, 5235, doi: 10.1093/mnras/stz737

Arnaud, K. A. 1996, in Astronomical Society of the Pacific Conference Series, Vol. 101, Astronomical Data Analysis Software and Systems V, ed. G. H. Jacoby & J. Barnes, 17

Ballet, J., Denis, M., Gilfanov, M., et al. 1993, IAU Cirulars, 5874, 1

Barcons, X., Barret, D., Decourchelle, A., et al. 2012, Athena (Advanced Telescope for High ENergy Astrophysics) Assessment Study Report for ESA Cosmic Vision 2015-2025. https://arxiv.org/abs/1207.2745

Barkov, M. V., Khangulyan, D. V., & Popov, S. B. 2012, Monthly Notices of the Royal Astronomical Society, 427, 589, doi: 10.1111/j.1365-2966.2012.22029.x

Bassi, T., Del Santo, M., D'Aı, A., et al. 2019, Monthly Notices of the RAS, 482, 1587, doi: 10.1093/mnras/sty2739

Bednarek, W., & Protheroe, R. J. 1999, Monthly Notices of the Royal Astronomical Society, 302, 373, doi: 10.1046/j.1365-8711.1999.02132.x

Belloni, T. M., Motta, S. E., & Muñoz-Darias, T. 2011, Black hole transients. https://arxiv.org/abs/1109.3388

Blandford, R. D., & Payne, D. G. 1982, Monthly Notices of the Royal Astronomical Society, 199, 883, doi: 10.1093/mnras/199.4.883

Blandford, R. D., & Znajek, R. L. 1977, Monthly Notices of the Royal Astronomical Society, 179, 433, doi: 10.1093/mnras/179.3.433

Bolis, F., Sobacchi, E., & Tavecchio, F. 2024, Polarization of synchrotron radiation from blazar jets. https://arxiv.org/abs/2411.16389

Bordas, P. 2009, PhD thesis, Universitat de Barcelona

Brown, G. E., & Bethe, H. A. 1994, Astrophysical Journal, 423, 659, doi: 10.1086/173844

Bu, Q., & Zhang, S. 2023, Black Holes: Accretion Processes in X-ray Binaries (Springer Nature Singapore), 1–28, doi: 10.1007/978-981-16-4544-0_99-1

Buckley, D. A. H., Brink, J., Charles, P. A., & Groenewald, D. 2021, The Astronomer's Telegram, 14597, 1

Buisson, D. J. K., Altamirano, D., Armas Padilla, M., et al. 2021, Monthly Notices of the Royal Astronomical Society, 503, 5600, doi: 10.1093/mnras/stab863

Burrows, D. N., Hill, J. E., Nousek, J. A., et al. 2005, Space Science Reviews, 120, 165, doi: 10.1007/s11214-005-5097-2

Cao, Z., Jonker, P. G., Wen, S., & Zabludoff, A. I. 2024, arXiv e-prints, arXiv:2409.17695, doi: 10.48550/arXiv.2409.17695

Casares, J., Yanes-Rizo, I. V., Torres, M. A. P., et al. 2023, Monthly Notices of the Royal Astronomical Society, 526, 5209, doi: 10.1093/mnras/stad3068

Casella, P., Belloni, T., & Stella, L. 2005, The Astrophysical Journal, 629, 403, doi: 10.1086/431174

Casella, P., Maccarone, T. J., O'Brien, K., et al. 2010, Monthly Notices of the Royal Astronomical Society: Letters, 404, L21–L25, doi: 10.1111/j.1745-3933.2010.00826.x

Cassatella, P., Uttley, P., Wilms, J., & Poutanen, J. 2012, Monthly Notices of the Royal Astronomical Society, 422, 2407, doi: 10.1111/j.1365-2966.2012.20792.x

Chakravorty, S., Petrucci, P.-O., Ferreira, J., et al. 2016, Astronomy and Astrophysics, 589, A119, doi: 10.1051/0004-6361/201527163

Chand, S., Dewangan, G. C., Thakur, P., Tripathi, P., & Agrawal, V. K. 2021, The Astronomer's Telegram, 14630, 1

Chand, S., Dewangan, G. C., Thakur, P., Tripathi, P., & Agrawal, V. K. 2022, The Astrophysical Journal, 933, 69, doi: 10.3847/1538-4357/ac7154

Chenevez, J., Maartensson, A. S., Andersen, C. L., & Jaisawal, G. K. 2021, The Astronomer's Telegram, 14601, 1

Connors, R. M. T., García, J. A., Steiner, J. F., et al. 2019, The Astrophysical Journal, 882, 179, doi: 10.3847/1538-4357/ab35df

Corbel, S., & Fender, R. P. 2002, The Astrophysical Journal, 573, L35–L39, doi: 10.1086/341870

Corbel, S., Kaaret, P., Fender, R. P., et al. 2005, The Astrophysical Journal, 632, 504–513, doi: 10.1086/432499

Coriat, M., Corbel, S., Buxton, M. M., et al. 2009, Monthly Notices of the Royal Astronomical Society, 400, 123–133, doi: 10.1111/j.1365-2966.2009.15461.x

Coriat, M., Corbel, S., Prat, L., et al. 2011, Monthly Notices of the Royal Astronomical Society, 414, 677–690, doi: 10.1111/j.1365-2966.2011.18433.x

Corral-Santana, J. M., Casares, J., Muñoz-Darias, T., et al. 2016, Astronomy and Astrophysics, 587, A61, doi: 10.1051/0004-6361/201527130

Coughenour, B. M., Tomsick, J. A., Mastroserio, G., et al. 2023, The Astrophysical Journal, 949, 70, doi: 10.3847/1538-4357/acc65c

Czerny, B., Różańska, A., Janiuk, A., & Życki, P. 2000, New Astronomy Reviews, 44, 439–441, doi: 10.1016/s1387-6473(00)00076-2

Dauser, T., García, J., Walton, D. J., et al. 2016, Astronomy and Astrophysics, 590, A76, doi: 10.1051/0004-6361/201628135

Dauser, T., Garcia, J., Wilms, J., et al. 2013, Monthly Notices of the Royal Astronomical Society, 430, 1694, doi: 10.1093/mnras/sts710

Davis, J. E. 2001, The Astrophysical Journal, 562, 575, doi: 10.1086/323488

Davis, S. W., Blaes, O. M., Hubeny, I., & Turner, N. J. 2005, The Astrophysical Journal, 621, 372, doi: 10.1086/427278

Davis, S. W., Blaes, O. M., Hubeny, I., & Turner, N. J. 2005, Astrophysical Journal, 621, 372, doi: 10.1086/427278

Davis, S. W., & Hubeny, I. 2006, The Astrophysical Journal Supplement Series, 164, 530, doi: 10.1086/503549

De Marco, B., Zdziarski, A. A., Ponti, G., et al. 2021, Astronomy and Astrophysics, 654, A14, doi: 10.1051/0004-6361/202140567

Degenaar, N., Altamirano, D., Parker, M., et al. 2016, Monthly Notices of the Royal Astronomical Society, 461, 4049, doi: 10.1093/mnras/stw1593

della Valle, M., Mirabel, I. F., & Rodriguez, L. F. 1994, Astronomy and Astrophysics, 290, 803

Deloye, C. J., Heinke, C. O., Taam, R. E., & Jonker, P. G. 2008, Monthly Notices of the Royal Astronomical Society, 391, 1619–1628, doi: 10.1111/j.1365-2966.2008.14021.x

Dihingia, I. K., Mizuno, Y., & Sharma, P. 2023, High-soft to low-hard state transition in black hole X-ray binaries with GRMHD simulations. https://arxiv.org/abs/2309.16092

Done, C., Gierliński, M., & Kubota, A. 2007, The Astronomy and Astrophysics Review, 15, 1–66, doi: 10.1007/s00159-007-0006-1

Draghis, P. A., Miller, J. M., Cackett, E. M., et al. 2020, The Astrophysical Journal, 900, 78, doi: 10.3847/1538-4357/aba2ec

Dunn, R. J. H., Fender, R. P., Körding, E. G., Belloni, T., & Cabanac, C. 2010, Monthly Notices of the Royal Astronomical Society, 403, 61, doi: 10.1111/j.1365-2966.2010.16114.x

Ebisawa, K., Ogawa, M., Aoki, T., et al. 1994, Publications of the ASJ, 46, 375

Echiburú-Trujillo, C., Tetarenko, A. J., Haggard, D., et al. 2024, The Astrophysical Journal, 962, 116, doi: 10.3847/1538-4357/ad1a10

Espinasse, M., Carotenuto, F., Tremou, E., et al. 2021, The Astronomer's Telegram, 14607, 1

Espinasse, M., Corbel, S., Kaaret, P., et al. 2020, The Astrophysical Journal Letters, 895, L31, doi: 10.3847/2041-8213/ab88b6

Fabian, A. C., Rees, M. J., Stella, L., & White, N. E. 1989, Monthly Notices of the Royal Astronomical Society, 238, 729, doi: 10.1093/mnras/238.3.729

Fan, N., Steiner, J. F., Bambi, C., et al. 2024, arXiv e-prints, arXiv:2412.07621, doi: 10.48550/arXiv.2412.07621

Fender, R. P. 2001, Monthly Notices of the Royal Astronomical Society, 322, 31, doi: 10.1046/j.1365-8711.2001.04080.x

Fender, R. P., Belloni, T. M., & Gallo, E. 2004, Monthly Notices of the Royal Astronomical Society, 355, 1105–1118, doi: 10.1111/j.1365-2966.2004.08384.x

Fender, R. P., Homan, J., & Belloni, T. M. 2009, Monthly Notices of the Royal Astronomical Society, 396, 1370, doi: 10.1111/j.1365-2966.2009.14841.x

Foreman-Mackey, D., Hogg, D. W., Lang, D., & Goodman, J. 2013, Publications of the Astronomical Society of the Pacific, 125, 306, doi: 10.1086/670067

Fragione, G. e. a. 2018, The Astrophysical Journal, 867, 119, doi: 10.3847/1538-4357/aae597

Freitag, M. e. a. 2006, Monthly Notices of the Royal Astronomical Society, 368, 141, doi: 10.1111/j.1365-2966.2006.10115.x

Fruscione, A., McDowell, J. C., Allen, G. E., et al. 2006, in Society of Photo-Optical Instrumentation Engineers (SPIE) Conference Series, Vol. 6270, Society of Photo-Optical Instrumentation Engineers (SPIE) Conference Series, ed. D. R. Silva & R. E. Doxsey, 62701V, doi: 10.1117/12.671760

Fuerst, F., Belanger, G., Parker, M., et al. 2018, The Astronomer's Telegram, 11357, 1

Gallo, E., Fender, R. P., & Pooley, G. G. 2003, Monthly Notices of the Royal Astronomical Society, 344, 60–72, doi: 10.1046/j.1365-8711.2003.06791.x

Gandhi, P., Blain, A. W., Russell, D. M., et al. 2011, The Astrophysical Journal Letters, 740, L13, doi: 10.1088/2041-8205/740/1/L13

García, J., & Kallman, T. R. 2010, The Astrophysical Journal, 718, 695, doi: 10.1088/0004-637X/718/2/695

García, J., Dauser, T., Lohfink, A., et al. 2014, The Astrophysical Journal, 782, 76, doi: 10.1088/0004-637X/782/2/76

García, J. A., Steiner, J. F., McClintock, J. E., et al. 2015, Astrophysical Journal, 813, 84, doi: 10.1088/0004-637X/813/2/84

García, J. A., Tomsick, J. A., Sridhar, N., et al. 2019, The Astrophysical Journal, 885, 48, doi: 10.3847/1538-4357/ab384f

García, J. A., Tomsick, J. A., Sridhar, N., et al. 2019, The Astrophysical Journal, 885, 48, doi: 10.3847/1538-4357/ab384f

García, J. A., Steiner, J. F., McClintock, J. E., et al. 2015, The Astrophysical Journal, 813, 84, doi: 10.1088/0004-637X/813/2/84

García, J. A., Tomsick, J. A., Sridhar, N., et al. 2019, The Astrophysical Journal, 885, 48, doi: 10.3847/1538-4357/ab384f

Gardner, E., & Done, C. 2013, Monthly Notices of the Royal Astronomical Society, 434, 3454, doi: 10.1093/mnras/stt1257

Gediman, B., Miller, J. M., Zoghbi, A., et al. 2024, Test for Echo: X-ray Reflection Variability in the Seyfert-2 AGN NGC 4388. https://arxiv.org/abs/2403.00926

Gelino, D. M., Balman, S., Kızıloglu, U., et al. 2006, The Astrophysical Journal, 642, 438–442, doi: 10.1086/500924

Gendreau, K., Arzoumanian, Z., Enoto, T., et al. 2021, The Astronomer's Telegram, 14588, 1

Gierliński, M., Done, C., & Page, K. 2009, Monthly Notices of the Royal Astronomical Society, 392, 1106, doi: 10.1111/j.1365-2966.2008.14166.x

Giersz, M. e. a. 2015, Monthly Notices of the Royal Astronomical Society, 454, 3150, doi: 10.1093/mnras/stv2162

Goodman, J., & Weare, J. 2010, Communications in Applied Mathematics and Computational Science, 5, 65, doi: 10.2140/camcos.2010.5.65

Greene, J. E. e. a. 2020, Annual Review of Astronomy and Astrophysics, 58, 257, doi: 10.1146/annurev-astro-032620-021835

Gropp, J. D., Kennea, J. A., Lien, A. Y., et al. 2021, The Astronomer's Telegram, 14591, 1

Grove, J. E., Grindlay, J. E., Harmon, B. A., et al. 1997, in AIP Conference Proceedings (AIP), 122–140, doi: 10.1063/1.54106

Harmon, B. A., & Paciesas, W. S. 1993, IAU Cirulars, 5913, 1

Harrison, F. A., Craig, W. W., Christensen, F. E., et al. 2013, The Astrophysical Journal, 770, 103, doi: 10.1088/0004-637x/770/2/103

Heida, M., Jonker, P. G., Torres, M. A. P., & Chiavassa, A. 2017, The Astrophysical Journal, 846, 132, doi: 10.3847/1538-4357/aa85df

Homan, J., & Belloni, T. 2005, Astrophysics and Space Science, 300, 107, doi: 10.1007/s10509-005-1197-4

Homan, J., Neilsen, J., Allen, J. L., et al. 2016, The Astrophysical Journal Letters, 830, L5, doi: 10.3847/2041-8205/830/1/L5

Homan, J., Bright, J., Motta, S. E., et al. 2020, The Astrophysical Journal Letters, 891, L29, doi: 10.3847/2041-8213/ab7932

Homan, J., Gendreau, K. C., Sanna, A., et al. 2021, The Astronomer's Telegram, 14606, 1

Hosokawa, R., Murata, K. L., Niwano, M., et al. 2021, The Astronomer's Telegram, 14594, 1

Huppenkothen, D., Younes, G., Ingram, A., et al. 2017, The Astrophysical Journal, 834, 90, doi: 10.3847/1538-4357/834/1/90

Huppenkothen, D., Younes, G., Ingram, A., et al. 2017, Astrophysical Journal, 834, 90, doi: 10.3847/1538-4357/834/1/90

Hynes, R. I. 2010, Multiwavelength Observations of Accretion in Low-Mass X-ray Binary Systems. https://arxiv.org/abs/1010.5770

Ingram, A., Done, C., & Fragile, P. C. 2009, Monthly Notices of the Royal Astronomical Society: Letters, 397, L101, doi: 10.1111/j.1745-3933.2009.00693.x

Ingram, A. R., & Motta, S. E. 2019, New Astronomy Reviews, 85, 101524, doi: 10.1016/j.newar.2020.101524

Inoue, H. 2022, Publications of the Astronomical Society of Japan, 74, 1263–1274, doi: 10.1093/pasj/psac081

Jana, A., Chatterjee, D., Chang, H.-K., Naik, S., & Mondal, S. 2023, Monthly Notices of the Royal Astronomical Society, 527, 2128, doi: 10.1093/mnras/stad3192

Jana, A., Jaisawal, G. K., Chhotaray, B., et al. 2021a, The Astronomer's Telegram, 14629, 1

Jana, A., Jaisawal, G. K., Naik, S., et al. 2021b, Research in Astronomy and Astrophysics, 21, 125, doi: 10.1088/1674-4527/21/5/125

Jiang, J., Fabian, A. C., Wang, J., et al. 2019, Monthly Notices of the Royal Astronomical Society, 484, 1972, doi: 10.1093/mnras/stz095

Jiang, J., Buisson, D. J. K., Dauser, T., et al. 2022, Monthly Notices of the Royal Astronomical Society, 514, 1952, doi: 10.1093/mnras/stac1401

John, C., De, K., Lucchini, M., et al. 2024, Correlated mid-infrared and X-ray outbursts in black hole X-ray binaries: A new route to discovery in infrared surveys. https://arxiv.org/abs/2406.17866

Kalemci, E., Begelman, M. C., Maccarone, T. J., et al. 2016, Monthly Notices of the Royal Astronomical Society, 463, 615, doi: 10.1093/mnras/stw2002

Kalemci, E., Tomsick, J. A., Buxton, M., et al. 2005, The Astrophysical Journal, 622, 508

Kallman, T., & Bautista, M. 2001, The Astrophysical Journal Supplement Series, 133, 221, doi: 10.1086/319184

Kallman, T. R., Palmeri, P., Bautista, M. A., Mendoza, C., & Krolik, J. H. 2004, The Astrophysical Journal Supplement Series, 155, 675, doi: 10.1086/424039

Kara, E., Fabian, A. C., Lohfink, A. M., et al. 2015, Monthly Notices of the Royal Astronomical Society, 449, 234–242, doi: 10.1093/mnras/stv304

Kataoka, J., Mattox, J. R., Quinn, J., et al. 1999, Astrophysical Journal, 514, 138, doi: 10.1086/306918

Kawase, T., Negoro, H., Yoneyama, T., et al. 2018, The Astronomer's Telegram, 11323, 1

Kennea, J. A., Palmer, D. M., Lien, A. Y., et al. 2018, The Astronomer's Telegram, 11326, 1

Khargharia, J., Froning, C. S., Robinson, E. L., & Gelino, D. M. 2012, The Astronomical Journal, 145, 21, doi: 10.1088/0004-6256/145/1/21

Koljonen, K. I. I., Maccarone, T., McCollough, M. L., et al. 2018a, Astronomy and Astrophysics, 612, A27, doi: 10.1051/0004-6361/201732284

—. 2018b, Astronomy and Astrophysics, 612, A27, doi: 10.1051/0004-6361/201732284

Kostić, U., Čadež, A., Calvani, M., & Gomboc, A. 2009, Astronomy and Astrophysics, 496, 307, doi: 10.1051/0004-6361/200811059

Kravtsov, V., Berdyugin, A., Kosenkov, I., et al. 2022, Monthly Notices of the Royal Astronomical Society, 514, doi: 10.1093/mnras/stac1470

Kumar, R. 2024, Monthly Notices of the Royal Astronomical Society, 532, 2635–2643, doi: 10.1093/mnras/stae1683

Kumar, R., Bhattacharyya, S., Bhatt, N., & Misra, R. 2022, Monthly Notices of the Royal Astronomical Society, 513, 4869, doi: 10.1093/mnras/stac1170

Kylafis, Nikolaos D., Reig, Pablo, & Papadakis, Iossif. 2020, Astronomy and Astrophysics, 640, L16, doi: 10.1051/0004-6361/202038468

Laycock, S. G. T., Cappallo, R. C., & Moro, M. J. 2014, Monthly Notices of the Royal Astronomical Society, 446, 1399, doi: 10.1093/mnras/stu2151

Lewin, C., Kara, E., Cackett, E. M., et al. 2023, X-ray/UVOIR Frequency-resolved Time Lag Analysis of Mrk 335 Reveals Accretion Disk Reprocessing. https://arxiv.org/abs/2307.11145

LHAASO Collaboration. 2024, arXiv e-prints, arXiv:2410.08988, doi: 10.48550/arXiv.2410.08988

Li, G.-X., Yuan, Y.-F., & Cao, X. 2010, The Astrophysical Journal, 715, 623, doi: 10.1088/0004-637X/715/1/623

Li, L.-X., Zimmerman, E. R., Narayan, R., & McClintock, J. E. 2005, The Astrophysical Journal Supplement Series, 157, 335, doi: 10.1086/428089

Li, L.-X., Zimmerman, E. R., Narayan, R., & McClintock, J. E. 2005, The Astrophysical Journal Supplement Series, 157, 335, doi: 10.1086/428089

Liu, H. X., Huang, Y., Bu, Q. C., et al. 2022, The Astrophysical Journal, 938, 108, doi: 10.3847/1538-4357/ac88c6

Liu, J., McClintock, J. E., Narayan, R., Davis, S. W., & Orosz, J. A. 2008, The Astrophysical Journal, 679, L37–L40, doi: 10.1086/588840

Liu, Z., Malyali, A., Krumpe, M., et al. 2023a, Astronomy and Astrophysics, 669, A75, doi: 10.1051/0004-6361/202244805

—. 2023b, Astronomy and Astrophysics, 669, A75, doi: 10.1051/0004-6361/202244805

Lucchini, M., Russell, T., Markoff, S., et al. 2020, Monthly Notices of the Royal Astronomical Society, 501, doi: 10.1093/mnras/staa3957

Maccarone, T. J., Coppi, P. S., & Taam, R. E. 1999, in American Astronomical Society Meeting Abstracts, Vol. 195, American Astronomical Society Meeting Abstracts, 37.03

Makishima, K., Maejima, Y., Mitsuda, K., et al. 1986, The Astrophysical Journalj, 308, 635, doi: 10.1086/164534

Malyshev, D., Chernyakova, M., Neronov, A., & Walter, R. 2015, Astronomy and Astrophysics, 582, A11, doi: 10.1051/0004-6361/201526120

Malzac, J., Merloni, A., & Fabian, A. C. 2005, Astrophysics and Space Science, 300, 31–38, doi: 10.1007/s10509-005-1187-6

Malzac, J., Kalamkar, M., Vincentelli, F., et al. 2018, Monthly Notices of the Royal Astronomical Society, 480, 2054–2071, doi: 10.1093/mnras/sty2006

Mao, D.-M., & Yu, W.-F. 2021, Research in Astronomy and Astrophysics, 21, 170, doi: 10.1088/1674-4527/21/7/170

Mapelli, M. e. a. 2021, Frontiers in Astronomy and Space Sciences, 8, 107, doi: 10.3389/fspas.2021.627845

Marcel, G., Ferreira, J., Petrucci, P.-O., et al. 2018, Astronomy and Astrophysics, 615, A57, doi: 10.1051/0004-6361/201732069

Marino, A., Barnier, S., Petrucci, P. O., et al. 2021, Astronomy and Astrophysics, 656, A63, doi: 10.1051/0004-6361/202141146

Markoff, S., Nowak, M. A., & Wilms, J. 2005, The Astrophysical Journal, 635, 1203

Masetti, N., Bianchini, A., Bonibaker, J., della Valle, M., & Vio, R. 1996, Astronomy and Astrophysics, 314, 123

Matt, G., Fabian, A. C., & Ross, R. R. 1993, Monthly Notices of the RAS, 262, 179, doi: 10.1093/mnras/262.1.179

McClintock, J. E., Narayan, R., & Steiner, J. F. 2014, Space Science Reviews, 183, 295, doi: 10.1007/s11214-013-0003-9

McClintock, J. E., & Remillard, R. A. 2004, Black Hole Binaries. https://arxiv.org/abs/astro-ph/0306213

McClintock, J. E., Shafee, R., Narayan, R., et al. 2006, The Astrophysical Journal, 652, 518, doi: 10.1086/508457

McClintock, J. E., Shafee, R., Narayan, R., et al. 2006, The Astrophysical Journal, 652, 518, doi: 10.1086/508457

Merloni, A., Heinz, S., & di Matteo, T. 2003, Monthly Notices of the Royal Astronomical Society, 345, 1057, doi: 10.1046/j.1365-2966.2003.07017.x

Mezcua, M. 2017, International Journal of Modern Physics D, 26, 1730021, doi: 10.1142/S021827181730021X

Migliari, S., Tomsick, J. A., Maccarone, T. J., et al. 2006, The Astrophysical Journal, 643, L41–L44, doi: 10.1086/505028

Miller, J. M., Fabian, A. C., Kaastra, J., et al. 2015, Powerful, Rotating Disk Winds from Stellar-mass Black Holes. https://arxiv.org/abs/1510.01177

Miller, J. M., & Reynolds, M. T. 2021, The Astronomer's Telegram, 14650, 1

Miller, J. M., Raymond, J., Fabian, A. C., et al. 2004, The Astrophysical Journal, 601, 450–465, doi: 10.1086/380196

—. 2016, The Astrophysical Journal Letters, 821, L9, doi: 10.3847/2041-8205/821/1/l9

Miller, J. M., Gendreau, K., Ludlam, R. M., et al. 2018, Astrophysical Journal Letters, 860, L28, doi: 10.3847/2041-8213/aacc61

Miller, L., Turner, T. J., Reeves, J. N., et al. 2006, Astronomy and Astrophysics, 453, L13, doi: 10.1051/0004-6361:20065276

Miller, M. C., & Colbert, E. J. M. 2004, International Journal of Modern Physics D, 13, 1, doi: 10.1142/S0218271804004426

Miller-Jones, J. C. A., Gallo, E., Rupen, M. P., et al. 2008, Monthly Notices of the Royal Astronomical Society, 388, 1751, doi: 10.1111/j.1365-2966.2008.13495.x

Miller-Jones, J. C. A., Jonker, P. G., Maccarone, T. J., Nelemans, G., & Calvelo, D. E. 2011, The Astrophysical Journal Letters, 739, L18, doi: 10.1088/2041-8205/739/1/L18

Mitsuda, K., Inoue, H., Koyama, K., et al. 1984, Publications of the Astronomical Society of Japan, 36, 741

Motta, S., Muñoz-Darias, T., Casella, P., Belloni, T., & Homan, J. 2011, Monthly Notices of the Royal Astronomical Society, 418, 2292–2307, doi: 10.1111/j.1365-2966.2011.19566.x

Motta, S., Rodriguez, J., Jourdain, E., et al. 2021, New Astronomy Reviews, 93, 101618, doi: https://doi.org/10.1016/j.newar.2021.101618

Motta, S. E., Casella, P., Henze, M., et al. 2015, Monthly Notices of the Royal Astronomical Society, 447, 2059, doi: 10.1093/mnras/stu2579

Motta, S. E., Franchini, A., Lodato, G., & Mastroserio, G. 2017, Monthly Notices of the Royal Astronomical Society, 473, 431–439, doi: 10.1093/mnras/stx2358

Muñoz-Darias, T., Motta, S., & Belloni, T. M. 2010, Monthly Notices of the Royal Astronomical Society, 410, 679–684, doi: 10.1111/j.1365-2966.2010.17476.x

Narayan, R., Mahadevan, R., & Quataert, E. 1998, Advection-Dominated Accretion around Black Holes. https://arxiv.org/abs/astro-ph/9803141

Narayan, R., & McClintock, J. E. 2008, New Astronomy Reviews, 51, 733–751, doi: 10.1016/j.newar.2008.03.002

Narayan, R., & Yi, I. 1994, The Astrophysical Journal Letters, 428, L13, doi: 10.1086/187381

Nathan, E., Ingram, A., Steiner, J. F., et al. 2024, Monthly Notices of the Royal Astronomical Society, doi: 10.1093/mnras/stae1896

Negoro, H., Masumitsu, T., Kawase, T., et al. 2016, The Astronomer's Telegram, 9876, 1

Neilsen, J., & Lee, J. C. 2009a, Nature, 458, 481, doi: 10.1038/nature07680

—. 2009b, Nature, 458, 481, doi: 10.1038/nature07680

Novikov, I. D., & Thorne, K. S. 1973a, in Black Holes (Les Astres Occlus), ed. C. Dewitt & B. S. Dewitt, 343–450

Novikov, I. D., & Thorne, K. S. 1973b, in Black Holes (Les Astres Occlus), ed. C. Dewitt & B. S. Dewitt, 343–450

Oda, S., Shidatsu, M., Nakahira, S., et al. 2019, Publications of the Astronomical Society of Japan, 71, doi: 10.1093/pasj/psz091

Orosz, J. A., Groot, P. J., van der Klis, M., et al. 2002, The Astrophysical Journal, 568, 845, doi: 10.1086/338984

Page, D. N., & Thorne, K. S. 1974, Astrophysical Journal, 191, 499, doi: 10.1086/152990

Paice, J. A., Gandhi, P., Charles, P. A., et al. 2019, Monthly Notices of the Royal Astronomical Society, 488, 512, doi: 10.1093/mnras/stz1613

Pal, M., Dewangan, G. C., Connolly, S. D., & Misra, R. 2016a, Monthly Notices of the Royal Astronomical Society, 466, 1777, doi: 10.1093/mnras/stw3173

—. 2016b, Monthly Notices of the Royal Astronomical Society, 466, 1777, doi: 10.1093/mnras/stw3173

Park, N. 2015, Performance of the VERITAS experiment. https://arxiv.org/abs/1508.07070

Parra, M., Petrucci, P.-O., Bianchi, S., et al. 2024, Astronomy and Astrophysics, 681, A49, doi: 10.1051/0004-6361/202346920

Petrucci, P.-O., Bianchi, S., Ponti, G., et al. 2021, Astronomy and Astrophysics, 649, A128, doi: 10.1051/0004-6361/202039524

Petrucci, P.-O., Bianchi, S., Ponti, G., et al. 2021, Astronomy & Astrophysics, 649, A128, doi: 10.1051/0004-6361/202039524

Plant, D. S., Fender, R. P., Ponti, G., Muñoz-Darias, T., & Coriat, M. 2015, Astronomy and Astrophysics, 573, A120, doi: 10.1051/0004-6361/201423925

Ponti, G., Fender, R. P., Begelman, M. C., et al. 2012, Monthly Notices of the Royal Astronomical Society, 422, L11, doi: 10.1111/j.1745-3933.2012.01224.x

Ponti, G., Fender, R. P., Begelman, M. C., et al. 2012, Monthly Notices of the Royal Astronomical Society: Letters, 422, L11, doi: 10.1111/j.1745-3933.2012.01224.x

Porquet, D., Reeves, J. N., Hagen, S., et al. 2024, Astronomy and Astrophysics, 689, A336, doi: 10.1051/0004-6361/202449708

Portegies Zwart, S. F. e. a. 2004, Nature, 428, 724, doi: 10.1038/nature02448

Poutanen, J., Veledina, A., Berdyugin, A. V., et al. 2022, Science, 375, 874–876, doi: 10.1126/science.abl4679

Radhika, D., & Nandi, A. 2014, Advances in Space Research, 54, 1678–1697, doi: 10.1016/j.asr.2014.06.039

Rau, A. 2018, The Astronomer's Telegram, 11332, 1

Reeves, J., Done, C., Pounds, K., et al. 2008, Monthly Notices of the Royal Astronomical Society: Letters, 385, L108–L112, doi: 10.1111/j.1745-3933.2008.00443.x

Reeves, J., Done, C., Pounds, K., et al. 2008, Monthly Notices of the Royal Astronomical Society, 385, L108, doi: 10.1111/j.1745-3933.2008.00443.x

Reig, P., & Kylafis, N. D. 2015, Astronomy and Astrophysics, 584, A109, doi: 10.1051/0004-6361/201527151

Reis, R. C., Fabian, A. C., & Miller, J. M. 2010, Monthly Notices of the Royal Astronomical Society, 402, 836, doi: 10.1111/j.1365-2966.2009.15976.x

Remillard, R. A., & McClintock, J. E. 2006, Annual Review of Astron and Astrophys, 44, 49, doi: 10.1146/annurev.astro.44.051905.092532

Remillard, R. A., & McClintock, J. E. 2006, Annual Review of Astronomy and Astrophysics, 44, 49–92, doi: 10.1146/annurev.astro.44.051905.092532

Remillard, R. A., Loewenstein, M., Steiner, J. F., et al. 2022, The Astronomical Journal, 163, 130, doi: 10.3847/1538-3881/ac4ae6

Reynolds, C., Kara, E., Mushotzky, R. F., et al. 2023, in UV, X-Ray, and Gamma-Ray Space Instrumentation for Astronomy XXIII, ed. O. H. Siegmund & K. Hoadley (SPIE), 49, doi: 10.1117/12.2677468

Romero, G. E., Vieyro, F. L., & Vila, G. S. 2010, Aastronomy and Astrophysics, 519, A109, doi: 10.1051/0004-6361/200913663

Ross, R. R., & Fabian, A. C. 2005, Monthly Notices of the Royal Astronomical Society, 358, 211, doi: 10.1111/j.1365-2966.2005.08797.x

Russell, D. 2018, Galaxies, 6, 3, doi: 10.3390/galaxies6010003

Russell, D. M., & Fender, R. P. 2008, Monthly Notices of the Royal Astronomical Society, 387, 713, doi: 10.1111/j.1365-2966.2008.13254.x

Russell, D. M., Maitra, D., Dunn, R. J. H., & Markoff, S. 2010, Monthly Notices of the Royal Astronomical Society, no, doi: 10.1111/j.1365-2966.2010.16547.x

Russell, D. M., Miller-Jones, J. C. A., Maccarone, T. J., et al. 2011, The Astrophysical Journal, 739, L19, doi: 10.1088/2041-8205/739/1/l19

Russell, D. M., Markoff, S., Casella, P., et al. 2012, Monthly Notices of the Royal Astronomical Society, 429, 815–832, doi: 10.1093/mnras/sts377

Russell, D. M., Russell, T. D., Miller-Jones, J. C. A., et al. 2013, The Astrophysical Journal, 768, L35, doi: 10.1088/2041-8205/768/2/l35

Russell, T. D., Miller-Jones, J. C. A., Sivakoff, G. R., Tetarenko, A. J., & JACPOT XRB Collaboration. 2018, The Astronomer's Telegram, 11356, 1

Sadowski, A. 2011, arXiv e-prints, arXiv:1108.0396, doi: 10.48550/arXiv.1108.0396

Sahakyan, N. 2018, The Astrophysical Journal, 866, 109, doi: 10.3847/1538-4357/aadade

Saikia, P., Russell, D. M., Baglio, M. C., et al. 2022, The Astrophysical Journal, 932, 38, doi: 10.3847/1538-4357/ac6ce1

Sako, M., Kahn, S. M., Paerels, F., et al. 2003, Structure and Dynamics of Stellar Winds in High-mass X-ray Binaries. https://arxiv.org/abs/astro-ph/0309503

Salvesen, G., & Pokawanvit, S. 2020, Monthly Notices of the Royal Astronomical Society, 495, 2179, doi: 10.1093/mnras/staa1094

Serino, M., Negoro, H., Nakajima, M., et al. 2021, The Astronomer's Telegram, 14587, 1

Shahbaz, T., Fender, R. P., Watson, C. A., & O'Brien, K. 2008, The Astrophysical Journal, 672, 510–515, doi: 10.1086/523793

Shakura, N. I., & Sunyaev, R. A. 1973, Astronomy and Astrophysics, 24, 337

Shidatsu, M., Kobayashi, K., Negoro, H., et al. 2022, The Astrophysical Journal, 927, 151, doi: 10.3847/1538-4357/ac517b

Shimura, T., & Takahara, F. 1995, The Astrophysical Journal, 445, 780, doi: 10.1086/175740

Sikora, M., & Zdziarski, A. 2023, Formation and evolution of transient jets and their cavities in black-hole X-ray binaries. https://arxiv.org/abs/2307.02853

Skipper, C. J., & McHardy, I. M. 2016, Monthly Notices of the Royal Astronomical Society, 458, 1696, doi: 10.1093/mnras/stw436

Steiner, J. F., García, J. A., Eikmann, W., et al. 2017, The Astrophysical Journal, 836, 119, doi: 10.3847/1538-4357/836/1/119

Steiner, J. F., García, J. A., Eikmann, W., et al. 2017, The Astrophysical Journal, 836, 119, doi: 10.3847/1538-4357/836/1/119

Steiner, J. F., & McClintock, J. E. 2012, The Astrophysical Journal, 745, 136, doi: 10.1088/0004-637x/745/2/136

Steiner, J. F., McClintock, J. E., & Reid, M. J. 2012a, The Astrophysical Journal Letters, 745, L7, doi: 10.1088/2041-8205/745/1/L7

—. 2012b, Astrophysical Journal Letters, 745, L7, doi: 10.1088/2041-8205/745/1/L7

Steiner, J. F., McClintock, J. E., Remillard, R. A., et al. 2010, The Astrophysical Journal Letters, 718, L117, doi: 10.1088/2041-8205/718/2/L117

Steiner, J. F., McClintock, J. E., Remillard, R. A., Narayan, R., & Gou, L. 2009, The Astrophysical Journal, 701, L83–L86, doi: 10.1088/0004-637x/701/2/l83

Steiner, J. F., Narayan, R., McClintock, J. E., & Ebisawa, K. 2009, Publications of the Astron. Soc. of the Pacific, 121, 1279, doi: 10.1086/648535

Steiner, J. F., Remillard, R. A., García, J. A., & McClintock, J. E. 2016, The Astrophysical Journal Letters, 829, L22, doi: 10.3847/2041-8205/829/2/L22

Steiner, J. F., Ubach, S., Tomsick, J. A., Coughenour, B., & Homan, J. 2021, The Astronomer's Telegram, 14994, 1

Steiner, J. F., Nathan, E., Hu, K., et al. 2024, arXiv e-prints, arXiv:2406.12014, doi: 10.48550/arXiv.2406.12014

Steinle, N., & Kesden, M. 2022a, Physical Review D, 106, doi: 10.1103/physrevd.106.063028

—. 2022b, Phys. Rev. D, 106, 063028, doi: 10.1103/PhysRevD.106.063028

Stiele, H., & Kong, A. K. H. 2021, The Astrophysical Journal, 914, 93, doi: 10.3847/1538-4357/abfaa5

Svoboda, J., Dovčiak, M., Steiner, J. F., et al. 2024, The Astrophysical Journal Letters, 966, L35, doi: 10.3847/2041-8213/ad402e

Tao, L., Tomsick, J. A., Qu, J., et al. 2019, The Astrophysical Journal, 887, 184, doi: 10.3847/1538-4357/ab5282

Team, X. S. 2020, Science with the X-ray Imaging and Spectroscopy Mission (XRISM). https://arxiv.org/abs/2003.04962

Timmes, F. X., Woosley, S. E., & Weaver, T. A. 1996, The Astrophysical Journal, 457, 834, doi: 10.1086/176778

Tzanavaris, P., & Yaqoob, T. 2018, The Astrophysical Journal, 855, 25, doi: 10.3847/1538-4357/aaaab6

Ubach, S., Steiner, J., Homan, J., et al. 2021, The Astronomer's Telegram, 14660, 1

Ubach, S., Steiner, J. F., Jiang, J., et al. 2024a, arXiv e-prints, arXiv:2409.13481, doi: 10.48550/arXiv.2409.13481

—. 2024b, The Astrophysical Journal, 976, 38, doi: 10.3847/1538-4357/ad7b2c

Ueda, Y., Yamaoka, K., & Remillard, R. 2009, The Astrophysical Journal, 695, 888, doi: 10.1088/0004-637X/695/2/888

Uttley, P., & Malzac, J. 2023, Large and complex X-ray time lags from black hole accretion disks with compact inner coronae. https://arxiv.org/abs/2312.08302

Veledina, A., Poutanen, J., & Vurm, I. 2011, The Astrophysical Journal, 737, L17, doi: 10.1088/2041-8205/737/1/l17

Veledina, A., Poutanen, J., & Vurm, I. 2011, Astrophysical Journal Letters, 737, L17, doi: 10.1088/2041-8205/737/1/L17

Walton, D. J., Tomsick, J. A., Madsen, K. K., et al. 2016, The Astrophysical Journal, 826, 87, doi: 10.3847/0004-637x/826/1/87

Wang, J., Mastroserio, G., Kara, E., et al. 2021, The Astrophysical Journal Letters, 910, L3, doi: 10.3847/2041-8213/abec79

Wang, J., Kara, E., Lucchini, M., et al. 2022, The Astrophysical Journal, 930, 18, doi: 10.3847/1538-4357/ac6262

Wang, J.-M., Qiu, J., Du, P., & Ho, L. C. 2014, The Astrophysical Journal, 797, 65, doi: 10.1088/0004-637X/797/1/65

Wang, Y., Xu, Y., Ji, L., et al. 2021, The Astronomer's Telegram, 14613, 1

Wang-Ji, J., García, J. A., Steiner, J. F., et al. 2018, The Astrophysical Journal, 855, 61, doi: 10.3847/1538-4357/aaa974

Wijnands, R., & van der Klis, M. 1999, The Astrophysical Journal, 514, 939, doi: 10.1086/306993

Wilms, J., Allen, A., & McCray, R. 2000, The Astrophysical Journal, 542, 914, doi: 10.1086/317016

Woosley, S. E., Heger, A., & Weaver, T. A. 2002, Reviews of Modern Physics, 74, 1015, doi: 10.1103/RevModPhys.74.1015

Xing, Z., Fragos, T., Zapartas, E., et al. 2024, Astronomy and Astrophysics, 693, A27, doi: 10.1051/0004-6361/202451275

Xu, Y., & Harrison, F. 2021, The Astronomer's Telegram, 14609, 1

Yang, P., Zhang, G., Russell, D. M., et al. 2022a, Monthly Notices of the Royal Astronomical Society, 514, 234, doi: 10.1093/mnras/stac1120

—. 2022b, Monthly Notices of the Royal Astronomical Society, 514, 234–248, doi: 10.1093/mnras/stac1120

Yao, Y., & Feng, H. 2019, The Astrophysical Journal Letters, 884, L3, doi: 10.3847/2041-8213/ab44c7

Yorgancioglu, E. S., Bu, Q. C., Santangelo, A., et al. 2023, Astronomy and Astrophysics, 677, A79, doi: 10.1051/0004-6361/202346511

Zdziarski, A. A., & Gierliński, M. 2004, Progress of Theoretical Physics Supplement, 155, 99, doi: 10.1143/PTPS.155.99

Zhang, S. N., Cui, W., & Chen, W. 1997, The Astrophysical Journal, 482, L155, doi: 10.1086/310705

Zhang, Z., Bambi, C., Liu, H., et al. 2024, The Astrophysical Journal, 975, 22, doi: 10.3847/1538-4357/ad7b29

Zhao, S. J., Tao, L., Yin, Q. Q., et al. 2024, Astronomy and Astrophysics, 691, A192, doi: 10.1051/0004-6361/202449646

Zimmerman, E. R., Narayan, R., McClintock, J. E., & Miller, J. M. 2005a, Astrophysical Journal, 618, 832, doi: 10.1086/426071

—. 2005b, The Astrophysical Journal, 618, 832, doi: 10.1086/426071

Życki, P. T., Done, C., & Smith, D. A. 1999, Monthly Notices of the Royal Astronomical Society, 309, 561, doi: 10.1046/j.1365-8711.1999.02885.x

Özel, F., Psaltis, D., Narayan, R., & McClintock, J. E. 2010, The Astrophysical Journal, 725, 1918–1927, doi: 10.1088/0004-637x/725/2/1918